PFC/RR-87-2

DOE-ET 51013210
UC–20 f, g

Visible Continuum Measurements on the Alcator C Tokamak: Changes in Particle Transport During Pellet Fuelled Discharges

Mark Edward Foord

Plasma Fusion Center
Massachusetts Institute of Technology
Cambridge, MA 02139

December 1986

This work was supported by the U. S. Department of Energy Contract No. DE-AC02-78ET51013. Reproduction, translation, publication, use and disposal, in whole or in part by or for the United States government is permitted.

VISIBLE CONTINUUM MEASUREMENTS ON THE ALCATOR C TOKAMAK: CHANGES IN PARTICLE TRANSPORT DURING PELLET FUELLED DISCHARGES

Mark Edward Foord

B.S. Physics, University of California,Irvine
(1979)

Submitted to the
Department of Nuclear Engineering
in Partial Fulfillment of the Requirements
for the Degree of
DOCTOR OF PHILOSOPHY
at the
MASSACHUSETTS INSTITUTE OF TECHNOLOGY
December, 1986

Signature of Author Mark E Foord
Department of Nuclear Engineering
December, 1986

Certified by E. S. Marmar
Dr. Earl Marmar, Principal Research Scientist
Thesis Supervisor

Certified by I. H. Hutchinson
Professor Ian Hutchinson
Thesis Reader

Accepted by _____
Professor Allen Henry
Chairman, Department Committee of Graduate Students

VISIBLE CONTINUUM MEASUREMENTS ON THE ALCATOR C TOKAMAK: CHANGES IN PARTICLE TRANSPORT DURING PELLET FUELLED DISCHARGES

Mark Edward Foord

Submitted to the Department of Nuclear Engineering
in Partial Fulfillment of the Requirements for the Degree
of Doctor of Philosophy in Nuclear Engineering

ABSTRACT

A spatially resolving visible light detector system is used to measure continuum radiation near 5360Å on the Alcator C Tokamak. For the typically hot (T_e >>50 eV) plasmas studied, the continuum emission is found to be dominated by bremsstrahlung radiation near this wavelength region. Accurate determinations of Z_{eff} are obtained from continuum measurements using independently determined temperature and density measurements. For discharges with line-average electron densities $\overline{n_e} > 2\times 10^{14}\text{cm}^{-3}$, the weighted line-average $\overline{Z}_{eff} \simeq 1.2$, and $Z_{eff}(r)$ is found to have a relatively flat profile shape, inconsistent with neoclassical predictions. Small changes in the continuum brightness ($\Delta B/B \simeq 0.5\%$) due to sawteeth are detected and found to be consistent with a simple sawtooth model.

Density profiles during high density, clean ($\overline{Z}_{eff} \simeq 1.2$), pellet fueled discharges, are also determined and are used to study the changes in particle transport after injection. For discharges with sufficiently large pellet density increases ($\Delta\overline{n}_e/\overline{n}_e \geq .7 - .9$), density profiles are found to become more peaked following the injection. In these cases, the profiles are found to remain peaked for the remainder of the discharge, or until a 'giant' sawtooth or minor disruption abruptly returns the profiles to a flatter pre-pellet condition. Both the threshold for the particle transport changes and the effect of giant sawteeth are found to be well correlated with changes in trace impurity transport.

Analysis of density profiles after pellet injection yields information about the radial diffusion and convection velocity of the plasma particles. The peakedness in the density profiles, observed after pellet injection, is attributable mostly to increases in inward convection. It is concluded that neoclassical fluxes are too small to account for these changes. Predictions from collisionless η_i transport theory are found to be qualitatively consistent with the observed changes in the convection velocity.

Thesis Supervisor:

Dr. Earl Marmar, Principal Research Scientist, Plasma Fusion Center, M.I.T

Thesis Reader:

Ian Hutchinson, Professor of Nuclear Engineer, M.I.T

ACKNOWLEDGEMENTS

There are many people who deserve my thanks as I complete my graduate studies at MIT. I would like to thank the entire Alcator C group, in particular, Frank Silva, Martin Greenwald, Jim Terry, Steve Wolfe, Ron Parker, and Laurie Pfeifer for their help and support. I thank my advisor, Earl Marmar, for his invaluable guidance, and my thesis reader, professor Ian Hutchinson for helpful criticisms. I also thank my close friends, Marina, Brian, Herb, and Tom. Finally, I would like to thank my parents for their constant concern and encouragement throughout my years at MIT.

Table of Contents

This page is intentionally left blank.

CHAPTER 1

Introduction and Motivation for Continuum Studies

1.1 Introduction to Tokamak Research

This thesis presents measurements of visible continuum emissions from Alcator C Tokamak plasmas. A thorough introduction to the principles of tokamak confinement can be found in Ref. 4. A brief introduction is now presented. The tokamak, (a Russian acronym for TO(*toroidalnaya* - toroidal) KA(*kamera* - chamber) MA(*magnitnoi* - of magnetic) K(*katushki* - coils)) is a toroidally shaped, plasma confinement device (see Fig. 1.1). The plasma discharge is initiated by leaking a small amount of gas (eg. H_2, D_2, or He) into the toroidal vacuum chamber, while applying a toroidal electric field. This electric field is induced in the plasma by continuously changing the current through the ohmic coils ($E_{tor} = -d\Phi/dt$) positioned inside the hole of the torus (see Fig. 1.1). The electric field can drive a large toroidal current (for Alcator C $\sim$ .6 MA) which resistively heat the plasma ("ohmic heating" ηj^2), and can result in plasma temperatures of few keV ($\sim$ 10 -20 million degrees C). Unfortunately, the plasma's resistivity decreases as the plasma temperature increases, so that auxiliary heating schemes (like RF or neutral beam injection) will probably be needed in order to reach the relatively high temperatures required for plasma ignition[1].

The toroidal current is also useful in generating a poloidal magnetic field within the plasma which provides the plasma with an radially inward ($-\hat{r}$) equilibrium force necessary to balance the radially

outward expansion forces. The a[illegible]e of the poloidal field is typically much smaller than the toro[illegible] field (due to stability constraints[2,3]), and results in a slightly helical magnetic field. This effectively shorts-out the vertical electric fields which are inherent in toroidally confined plasmas, and which if present, would result in a loss of plasma confinement.

A vertical magnetic field B_{vert} is also used to help confine the plasma and is generated in the plasma by externally wound toroidal coils. B_{vert} provides the plasma current channel an inward equilibrium force (directed towards the [illegible]enter axis of the torus $\bar{j}_{tor} \times \bar{B}_{vert}$). This force balances the outwar[illegible]ansion forces which are inherent in toroidal confinement.

A toroidal magnetic field is used to help confine the hot ionized plasma particles, and if large enough can stabilize the kink mode instability[2,3]. Therefore, higher currents and thus, higher temperatures are achievable with larger toroidal fields. Alcator C's toroidal field (see Fig 1.1) is generated by helically connected copper plates (Bitter plates), which can generate relatively high toroidal fields ($\sim$ 15 T) in comparison to other present-day tokamaks in operation.

In 1968, at the Third International Conference on Plasma Physics and Controlled Nuclear Fusion Research in Novosibirsk, USSR[5], results from the T-3 Tokamak indicated that tokamak plasmas could be confined for much longer times (30 Bohm times) and at much higher temperatures (1 KeV) than other plasma confinement devices which were operating at that time. Since then, tokamak research has advanced significantly. Well confined, stable plasmas with densities and temperatures approaching fusion reactor relevant values are now routinely obtained by present-day operating tokamaks. However, the final order of

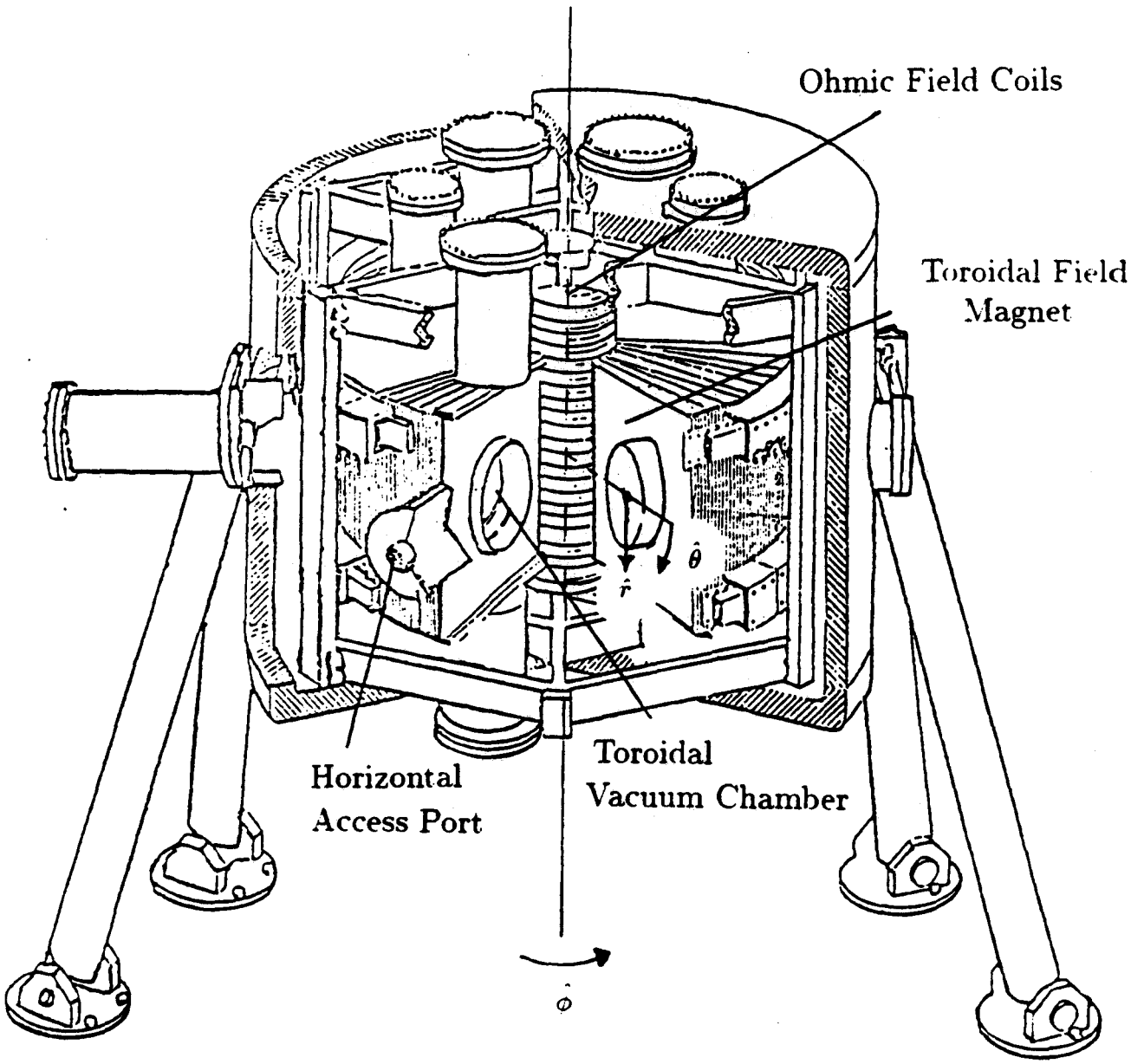

Figure 1.1 — Cutaway view of the Alcator C Tokamak. The orthogonal toroidal coordinate system ($\hat{r}$, $\hat{\theta}$, $\hat{\phi}$) is illustrated. These coordinate directions are also commonly referred to as 'radial', 'poloidal', and 'toroidal', respectfully.

magnitude increases in plasma temperatures and densities, necessary for plasma ignition, have not yet been achieved. Many technological problems associated with constructing safe, reliable, and economically attractive tokamak fusion reactors also remain to be solved.

1.2 Alcator C Tokamak

Experimental results presented in this thesis were obtained from measurements taken on the MIT Alcator C Tokamak[6]. Alcator C (a latin acronym for AL(*altus* - high) CA(*campus* - field) TOR(*toroid*)) is a research-oriented tokamak experiment which first began operation in 1979. Among present-day tokamaks, Alcator C is distinguished in having achieved, to date, the highest plasma densities $\overline{n_e} = 1.0 \times 10^{15}\text{cm}^{-3}$ with pellet fueled discharges[7]. In 1983, Alcator C was the first tokamak to reach the Lawson number $n_o\tau_E$ for thermalized breakeven[7].

The typical range of some of Alcator C plasma parameters are: line-average electron densities (non-pellet) $\overline{n_e} = .5 - 5 \times 10^{14}\text{cm}^{-3}$; central electron temperatures $T_{eo} = .5 - 2.5$ keV; toroidal currents $I_p = 100 - 600$ kA; and toroidal fields $B_t = 6 - 15$ T. The major radius (center of toroidal axis to plasma center distance) is 64 cm, and the minor radius (plasma column radius) is typically 16.5 cm.

1.3 Review of Spectroscopic Theory of Continuum Emission

Continuum radiation in hot plasmas results when either: 1) a free electron is accelerated by a positively charged nucleus, resulting in a free electron of less energy and a photon (bremsstrahlung radiation); or 2) a free electron is captured by an ion, resulting in a lower charge-state ion and a photon (recombination radiation). Both processes generally contribute to the total continuum emission, although, as will be shown, at certain temperatures and in certain wavelength regions bremsstrahlung emission dominates recombination radiation.

Spectroscopic theory provides accurate formulae for hydrogenic continuum cross-sections[8,9]. The total bremsstrahlung emissivity from a plasma with electron temperature T_e (eV), at wavelength λ (Å) , with electron density $n_e(\mathrm{cm}^{-3})$, ion density $n_i(\mathrm{cm}^{-3})$, and ion charge Z_i is:

$$E_{brem} = \frac{C_b}{\lambda} \frac{n_e n_i Z_i^2 \bar{g}_{ff} e^{-hc/\lambda T_e}}{T_e^{1/2}} \qquad \text{photons/sec/cm}^3\text{/Å/sr}, \qquad (1.1)$$

where C_b is $9.5 \times 10^{-14}/(4\pi)$, and $\bar{g}_{ff}$ is the free-free Gaunt factor, averaged over a maxwellian electron distribution at temperature T_e. The free-free Gaunt factor is defined as the ratio of the bremsstrahlung cross section to Kramers' classical emission cross section[10], and generally includes the effects of all non-classical processes. An analytical expression for g_{ff}, involving complex hypergeometric functions, has been calculated from quantum-mechanical dipole transition probabilities[8]. Numerical calculations of the temperature-averaged $\bar{g}_{ff}$ are shown in Fig. 1.2, and is generally a function of photon wavelength, ion charge, and electron temperature. In certain temperature and wavelength regimes simple analytic approximations have also been obtained[11]. The analytical expressions for $\bar{g}_{ff}$, which are used in this thesis, (valid at these low

photon energies (2.3 eV)) are given as: $\bar{g}_{ff} = (\sqrt{3}/\pi)\ln\{(4/\gamma^{5/2})(T/h\nu)(T/13.6Z_i^2)^{1/2})\}$ for $T < 77$ eV, and $\bar{g}_{ff} = (\sqrt{3}/\pi)\ln\{(4T/\gamma h\nu\}$ for $T > 77$ eV, where $\gamma = 1.781$.

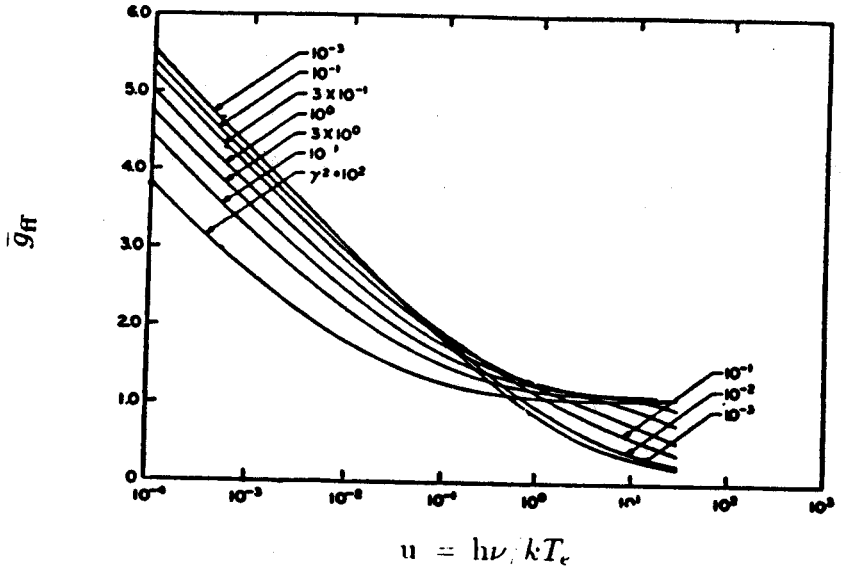

Figure 1.2 — Temperature-averaged free-free Gaunt factor versus $u = h\nu/kT_e$ for various values of $\gamma^2 = Z^2Ry/kT_e$. From Ref. 8.

The recombination emissivity from a plasma with electron temperature T_e (eV), at wavelength λ (Å) ,with electron density $n_e(\mathrm{cm}^{-3})$, ion density $n_i(\mathrm{cm}^{-3})$, and ion charge Z_i is

$$E_{recomb} = \frac{2C_b\chi_H}{\lambda}\frac{n_e n_i Z_i^4}{T_e^{3/2}}\sum_n\{\frac{\bar{g}_{fbn}}{n^3}e^{-hc/\lambda_n T_e}\} \qquad (1.2)$$

photons/sec/cm^3/Å/sr

where,

$$\lambda_n \equiv hc/(E_{continuum} - E_n),$$

χ_H is the Rydberg energy (13.6 eV), and $\bar{g}_{\rm fbn}$ is the free-bound Gaunt factor averaged over the shell of principal number n. The free-bound Gaunt factor is defined as the ratio of the recombination cross-section to Kramers' free-bound cross-sections[10]. $\bar{g}_{\rm fbn}$ has been calculated[8] for n $= 1 \rightarrow 20$ over a large range of $h\nu/\chi_H Z_i^2$. For photon wavelength $\lambda =$ 5360Å, $\bar{g}_{\rm fbn}$ is between .8 and 1.1 for all n and Z_i. The summation in Eq. 1.2 only includes the electron recombination into states of energy E_n ($E_n \equiv \chi_H Z_i^2/n^2$) such that $E_{continuum} - E_n \leq h\nu = 2.3eV(\lambda =$ 5360Å). Recombination into partially filled levels is not included in Eq. 1.2 since the contribution is small at these low photon energies.

Combining Eqs. 1.1 and 1.2, the ratio of recombination to bremsstrahlung emissivity is given by

$$\frac{E_{recomb}}{E_{brem}} = \frac{2\chi_H Z_i^2}{\bar{g}_{ff} T_e} \sum_n \{ \frac{\bar{g}_{\rm fbn}}{n^3} e^{-hc/\lambda_n T_e} \}. \qquad (1.3)$$

This continuum ratio is plotted in Fig 1.3 for electron temperatures between 2.3 - 2300 eV at $\lambda =$ 5360Å for ions of charge $Z_i =$ $1, Z_i = 6$ and $Z_i = 26$. In this wavelength region, bremsstrahlung radiation dominates the continuum ($> 99\%$) for sufficiently large electron temperatures ($T_e \geq 50$ eV). Since most continuum radiation near $\lambda =$ 5360Å is from the high density, hot (1-2 keV) central core of the

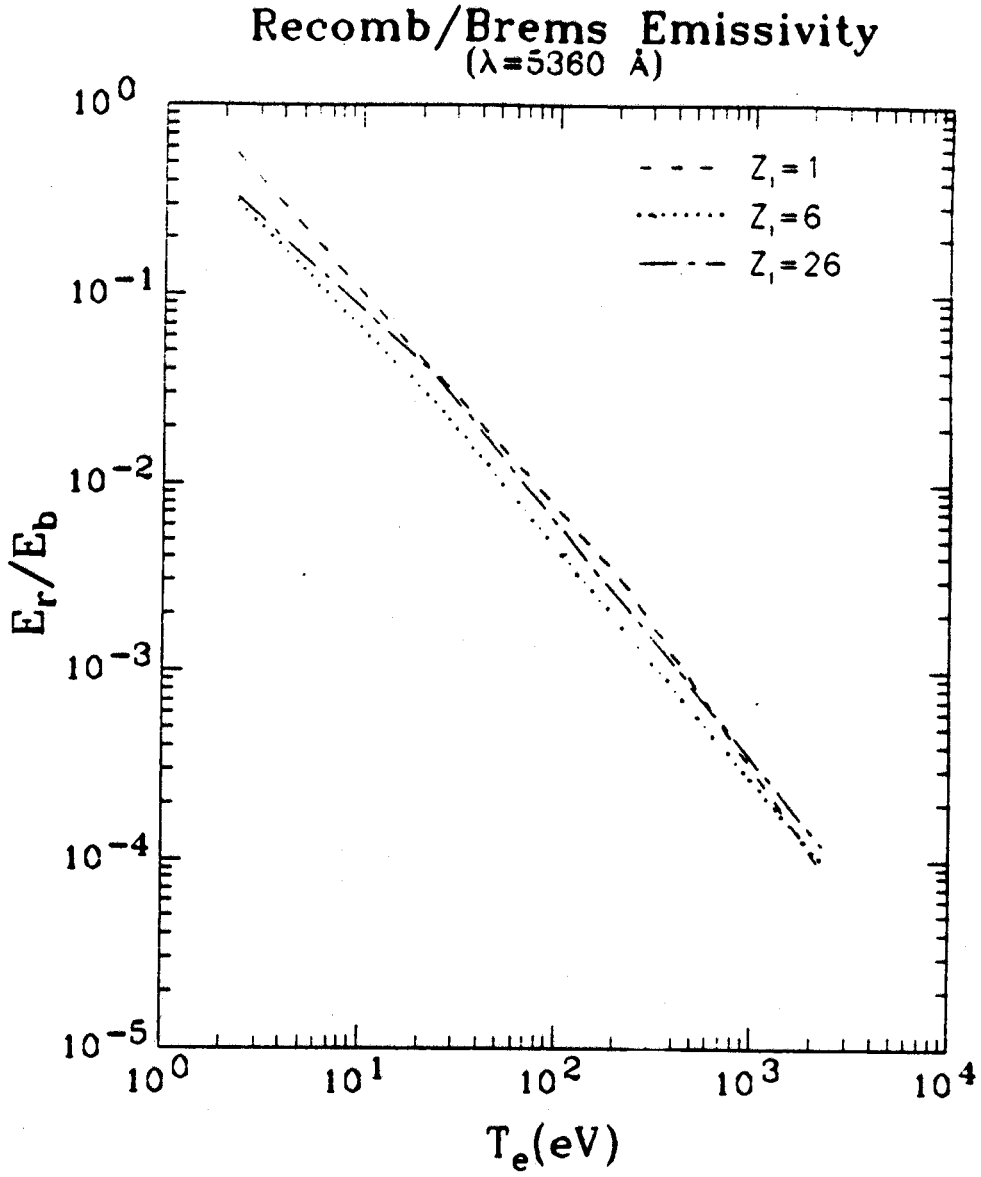

Figure 1.3 -- Ratio of thermal bremsstrahlung to recombination emissivities for $Z_i = 1$, 6, and 26, calculated from Eq. 1.3.

discharge, the total continuum emission is assumed to be largely dominated by bremsstrahlung radiation.

Measurements of the Alcator C spectrum in the visible region were obtained from analysis of film spectra using a 1/2 meter Jarrel-Ash monochromator. A typical spectrum between 5000Å $< \lambda <$ 5600Å, integrated over many discharges, is shown in Fig 1.4. The observed line at 5289 Å is identified as either OVI or CVI (n=8 — 7 transition), which may be populated from charge-exchange with neutral hydrogen. An OVI line was also identified at this wavelength on the T-6 Tokamak[12], although mislabeled as OIV[13]. The background level shown in Fig. 1.4, is attributed to the continuum radiation from the plasma.

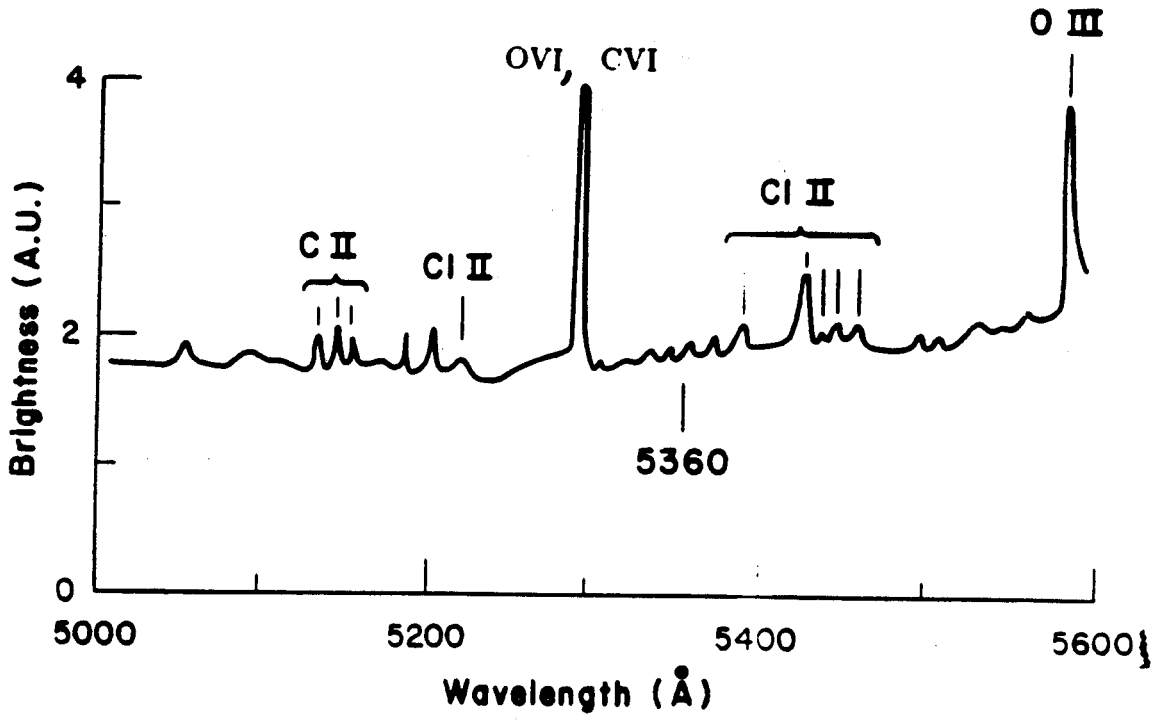

Figure 1.4 — Film spectrum of wavelength region 5000Å $\leq \lambda \leq$ 5600Å. Background level is attributed to continuum radiation.

As shown in Eq. 1.1, the bremsstrahlung emissivity is proportional to $n_e n_i Z_i^2$, where the weak charge dependence of $\bar{g}_{ff}$ will be ignored. In a plasma with multiple ion species, the emissivity is proportional to total emission from each species, or $\sum n_e n_i Z_i^2$. For a quasi-neutral plasma ($n_e = \sum n_i Z_i$), the total emission from a multiple species plasma is proportional to:

$$E_{brem} \propto n_e^2 \frac{\sum n_i Z_i^2}{\sum n_i Z_i}$$

The second term is defined as Z_{eff} :

$$Z_{eff} \equiv \frac{\sum n_i Z_i^2}{\sum n_i Z_i} \tag{1.4}$$

where each summation is over all ion species of charge Z_i. Z_{eff} is the average ionic charge, weighted by a Z_i factor. Thus, the presence of a very small percent of a highly ionized impurity ion can have a large effect on the plasma's Z_{eff} . For example, a hydrogenic plasma with 1.6% (n_{imp}/n_e) O^{+6} or 0.077% Fe^{+26} has a Z_{eff} of 1.5.

Equation 1.1 can now be rewritten for multiple ion species plasmas, in terms of Z_{eff} :

$$E_{brem} = \frac{C_b}{\lambda} \frac{n_e^2 Z_{eff}\ \bar{g}_{ff} e^{-hc/\lambda T_e}}{T_e^{1/2}} \qquad \text{photons/sec cm}^3/\text{Å/sr.} \tag{1.5}$$

where C_b is $9.5 \times 10^{-11}(4\pi)$ and $\bar{g}_{ff}$ is the free-free Gaunt factor of the background gas.

1.4 Visible Continuum Diagnostic and Applications

Three optical detector systems were built for use in measuring the visible continuum emissions from Alcator C plasmas. A brief introduction to these diagnostic systems is presented below with a more detailed description being presented in Chapter 2.

Visible light from the plasma is first filtered with an interference filter having a peak transmission in a wavelength region which has been determined to be dominated by the continuum (near 5360 Å). The light is then imaged and detected via each optical detector system. A 20-channel system[14], which uses photomultiplier tube (PMT) detectors, was originally designed for use at a side port (midplane of the torus) since stray magnetic fields are minimal there. Later, a single channel system which transmitted light through a 10-meter light pipe to a PMT, and a 16-channel photodiode detector system were built for use on Alcator's vertical ports. All of these detector systems are relatively easy to absolutely calibrate with a tungsten lamp and to optically align.

In order to determine the Z_{eff} profiles from visible continuum measurements, independent measurements of n_e and T_e are needed (see Eq. 1.5). The diagnostics which are usually available on Alcator C for determining n_e and T_e are: 1) 5-chord FIR interferometer ($n_e(r,t)$); 2) single chord Thomson scattering ($n_e(r=0,t)$ and $T_e(r=0,t)$ at $\sim$ 20 ms intervals); 3) ECE emission measurement ($T_e(r,t)$ or a radial scan of $T_e(r,t)$ every 15 ms); and 4) soft X-ray spectrum measurement (T_{eo}).

In cases where T_e and Z_{eff} profiles are known or can be estimated, electron density profiles can be inferred. This generally limits the analysis to high density, clean discharges where $Z_{eff}(r)$ is usually found to be quite flat and near 1 (Section 3.2). In Section 3.4, $Z_{eff}(r)$ is shown

to also remain relatively flat during N_2 gas injection, where Z_{eff} increases from 1.2 to 1.4.

One motivation for using continuum measurements to infer electron density profiles is the relatively high spatial resolution achievable– approximately the spatial resolution of the optical detection system ($\simeq$ 1 cm/channel). High resolution profile measurements are necessary to accurately determine the spatial variations of the particle transport. In Chapter 6, the particle transport during high density, pellet fueled discharges are presented. In these discharges, changes in particle transport are observed following pellet injection. Concurrent interferometer and Thomson scattering measurements are then used to check independently the continuum inferred line-integral and central densities.

1.5 Organization of Thesis

This thesis basically consists of four parts: a description of the continuum diagnostic, impurity studies, sawtooth detection, and particle transport studies during pellet injection discharges. Chapter 2 describes in detail the optical detector systems which are used to measure visible continuum brightness profiles. Chapter 3 presents measurements of Z_{eff} obtained from absolute continuum brightness measurements. Comparisons are made with values of Z_{eff} estimated from loop voltage and T_e measurements, and are found to be in good agreement over a wide range of values. Effects of N_2 gas-puff injection on Z_{eff} are studied. An important result of this chapter is that $\overline{Z}_{eff}$ (the approximate spatial average of $Z_{eff}(r)$) is found to be very close to 1 in high density discharges. This result was a major motivation for using the continuum as a density diagnostic. In Chapter 4, small sawtooth oscillations are detected on the central-chord visible continuum brightness, by averaging over many sawtooth periods. The sawtooth amplitude is $\Delta B/B \simeq 0.5\%$, which is found to be consistent with a simple sawtooth model. This result indicates that the continuum brightness is indeed due mostly to bremsstrahlung emissions from the high density core of the discharge. In Chapter 5, electron density profiles during high density, clean ($Z_{eff} \simeq 1.2$) pellet-fueled discharges are inferred from continuum brightness profile measurements. One interesting result is that in cases where the injected pellet increases the background density sufficiently, profiles are observed to remain peaked after the density has decayed to a new constant level. Chapter 6 presents analysis of these density profiles utilizing a technique which allows the diffusion coefficient D(r,t) and the inward convection velocity V(r,t) to be determined in the high density, source-free central region of the plasma.

CHAPTER 2

Experimental Apparatus and Calibration

2.1 Introduction

The major objective of this chapter is to describe in detail the detector systems which have been built to measure visible continuum radiation from Alcator C plasmas. The first diagnostic system used to measure visible continuum radiation from a tokamak plasma was built in 1979 by Kadota *et al*[15]. The single-channel optical system consisted of an imaging lens and monochromator which was set to only transmit continuum light ($\lambda = 5230\,\text{Å}$, $\Delta\lambda = 5\,\text{Å}$) to a detector. Z_{eff} radial profiles were obtained by shot-to-shot radial scans. Marmar *et al.*[16] used this technique in 1980 to obtain Z_{eff} profiles on Alcator.

The first multichannel visible continuum detector system for diagnosing tokamak plasmas was built in 1981 for use on Alcator C[14]. This detector system basically consists of an interference filter positioned in front of a 20-channel spatially resolving optical system. The filter's maximum passband wavelength is selected in a wavelength region which is found (from film spectrum measurements) to be relatively free of line emission ($\lambda \simeq 5360\,\text{Å}$). Recently, the use of the visible continuum has become widespread with similar diagnostic systems being built for use on other tokamaks[17-19].

Section 2.2 describes the 20-channel detector system, and contains a brief description of interference filters and photomultiplier tubes which are components of this system. Section 2.3 describes the single channel camera detector system. Section 2.4 describes a 16-channel camera

detector system, and contains a brief description of the PIN photodiode detectors which are used in this system. Section 2.5 presents the time responses of each system. Section 2.6 describes the method used to absolutely calibrate the detector systems.

2.2 20-Channel Detector System

A 20-channel, spatially resolving, visible light detector system has been used to measure continuum radiation on the Alcator C tokamak[14]. As shown in Fig. 2.1. the light is first filtered with a 30 Å FWHM interference filter having a peak transmission of 67% at $\lambda = 5360$ Å. The light is then imaged with a lens, 3.0 cm in diameter and 40 cm focal length, onto an array of light pipes and transmitted to 20 Hamamatsu 1P28 photomultiplier tubes (PMTs). The array is 0.79 cm wide and 7.6 cm high and consists of a 4 × 40 matrix of 1.0 mm-dia. plastic light pipes. This allows chordal measurements of 1.7 cm resolution at the center of the plasma with a limiter radius of 16 cm. The light pipes are epoxied into a drilled 1.6 mm-thick plate with a bundle of eight pipes transmitting light to each PMT. The current from each PMT is actively filtered at $\tau_{RC} = 100$ μsec and then digitized with a 12-bit, 5 kHz A/D converter. The cathode voltage is usually varied between −300 V and

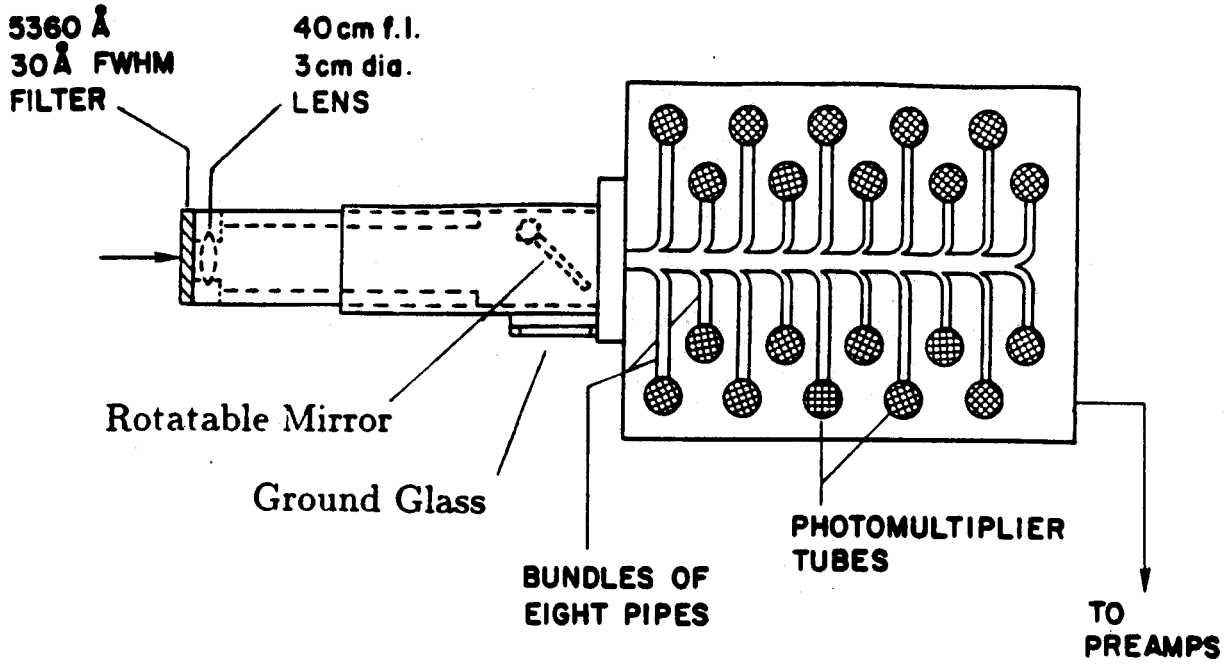

Figure 2.1 — Schematic of 20-channel visible detector system.

-600 V, depending on the plasma density, so as to maximize the dynamic range of the instrument.

The housing box is constructed of 4.7 mm-thick metal alloy (50% iron, 50% nickel, $\mu = 5 \times 10^4$.) This provides partial magnetic shielding from Alcator's external fields, which are primarily due to the ohmic heating transformer coil. In addition, each PMT is individually shielded, providing an overall magnetic attenuation $B_{\rm int}/B_{\rm ext} = 0.002$ with a saturation limit of 300 Gauss. The interference filter and lens are mounted directly on the mobile portion of the light shield, allowing adjustable focusing while eliminating stray light. A mirror is mounted near the

front of the light pipe array, which when rotated 45°, reflects light onto a frosted glass slide positioned at the image plane. This provides a viewfinder used for aligning the detector system.

For typical Alcator C parameters of $\overline{n_e} = 2 \times 10^{14}\,\mathrm{cm}^{-3}, T_{e0} = 1500\,\mathrm{eV}$, and $Z_{\mathrm{eff}} = 1$, the central chord bremsstrahlung power collected by this system ($\lambda = 5360\text{Å}, \Delta\lambda = 30\text{Å}$) is $4.2 \times 10^{-10}\,\mathrm{W}$ (1.1×10^9 photons/sec). A typical brightness profile from this detector system is shown in Fig. 2.2.

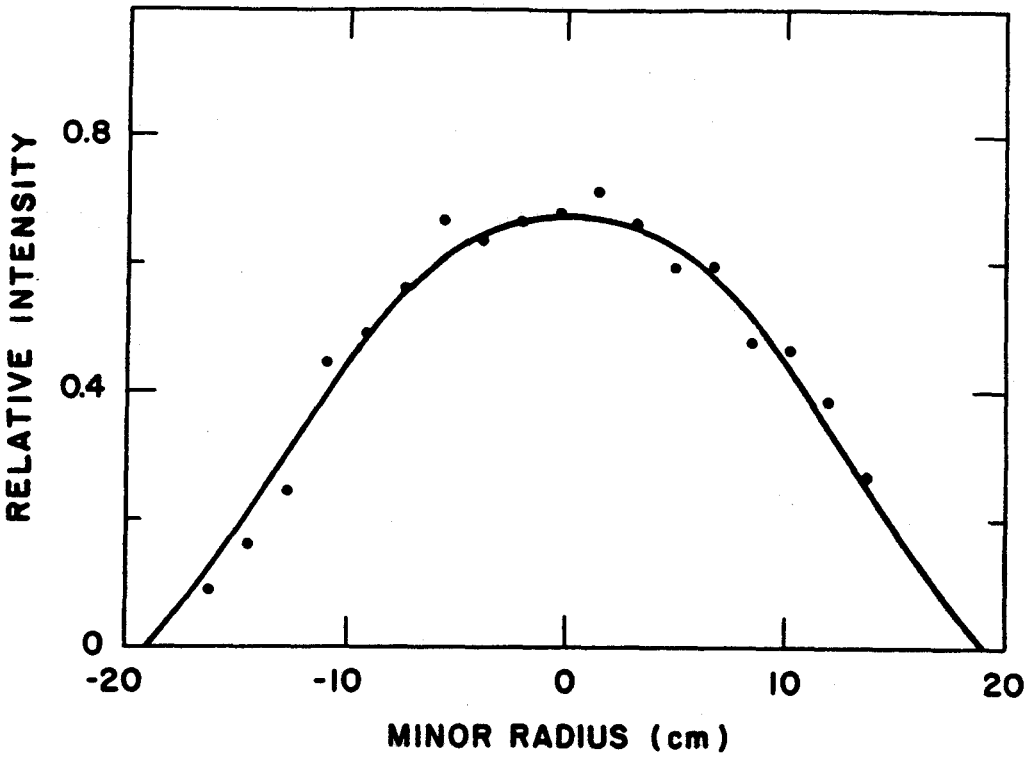

Figure 2.2 — Typical visible continuum brightness profile for a non-pellet, ohmically heated discharge. Brightness profile was obtained from the 20-channel instrument viewing the plasma from the horizontal midplane.

Interference Filters:

The three detector systems described in sections 2.2 – 2.4 use interference filters with peak transmissions near $\lambda = 5500\,\text{Å}$, which is a wavelength region dominated by continuum emission. Interference filters are composed of closely spaced, partially reflecting, plane parallel dielectric surfaces[20]. These Fabry-Perot-like interferometers spectrally filter incident light through multiple reflection interference. Maximum transmission of the incident light filter occurs when the phase difference between two parallel waves reflecting from the surface is πm ($m = 0, 1, 2, 3, \ldots$) radians. For a single layer dielectric of refraction index n, maximum transmission occurs at wavelengths:

$$\lambda_m \simeq \frac{2dncos(\theta)}{m - \phi/\pi}, \qquad m = 0, 1, 2, 3, \ldots \tag{2.1}$$

where d is the dielectric thickness, θ is the internal refraction angle, ϕ is the change in phase on internal reflection, and m is the transmission order. Single band transmission is achieved by using blocking filters above and below the desired wavelength λ. Narrow passband filters are obtained by using partially reflecting metallic coatings and multiple dielectric layers.

Use of interference filters can provide a relatively easy method of measuring brightnesses from integrated portions of the wavelength spectrum. This is particularly useful in measuring continuum light in wavelength regions relatively free from line emission. Interference filters which are commercially available have passband widths from about 10 Å FWHM to 1000 Å FWHM throughout the visible wavelength region.

As shown in Eq. 2.1, the peak transmission wavelength is down-shifted for light with incident angles not normal to the filter's surface ($\theta > 0°$). Thus, it is important to consider the angles of incidence for all rays of light which pass through the filter and strike the detector so as not to down-shift into a wavelength region containing many lines. For the geometry of this detector system the maximum incident angle is approximately 10° This corresponds to a down-shift of approximately 25 Å [21] which, as shown in Fig. 1.4, is in a wavelength region still dominated by continuum. The stop band rejection for these filters is $\sim .001\%$ (average), and $\sim .01\%$ (maximum)[21].

Photomultiplier Tubes:

The 20-channel detector system uses photomultiplier tubes (PMTs) to detect visible continuum radiation. Photomultiplier tubes consist of two components, a photoemissive cathode which emits a current proportional to the incident flux of light, and a current amplifying dynode chain. PMTs typically have $5-15$ dynode stages which provide a maximum photoemission current amplification of $10^5 - 10^7$. The sensitivity of a PMT is proportional to the product of the quantum efficiency of the photocathode (electrons/photon) with the current gain of the dynode stage, and is usually strongly dependent on the photocathode material and incident wavelength.

The 1P28 PMTs use Sb-Cs photocathodes which have quantum efficiencies of approximately 3% (at $\lambda = 5360\,\text{Å}$) resulting in a photocathode sensitivities of 15 mA/W. With a typical cathode voltage of $-400\,\text{V}$, the anode radiant sensitivity is 30 A/W.

2.3 Single Channel Detector System

The single channel detector system consists of a modified 35 mm SLR Pentax camera body with a light pipe mounted at the center of the image plane (see Fig. 2.3). Light is then transmitted through the light pipe to a Hamamatsu R955 PMT. A 5360 Å, 30 Å FWHM interference filter is positioned in front of 135 mm-focal-length, f3.5 lens, which focuses the light onto the .20 mm-dia. light pipe. This provides a spatial resolution of approximately 2 mm in the center of the plasma.The compact size of the camera body and the built-in viewfinder allow a relatively easy alignment of the light pipe-lens axis with the plasma center. The R955 PMT uses a multi-alkali photocathode having a quantum efficiency of 12% (at $\lambda = 5360\,\text{Å}$) resulting in a cathode sensitivity of 55 mA/W. For a typical cathode potential of $-700\,\text{V}$, the anode radiant sensitivity is approximately 2.1×10^4 A/W. The PMT current

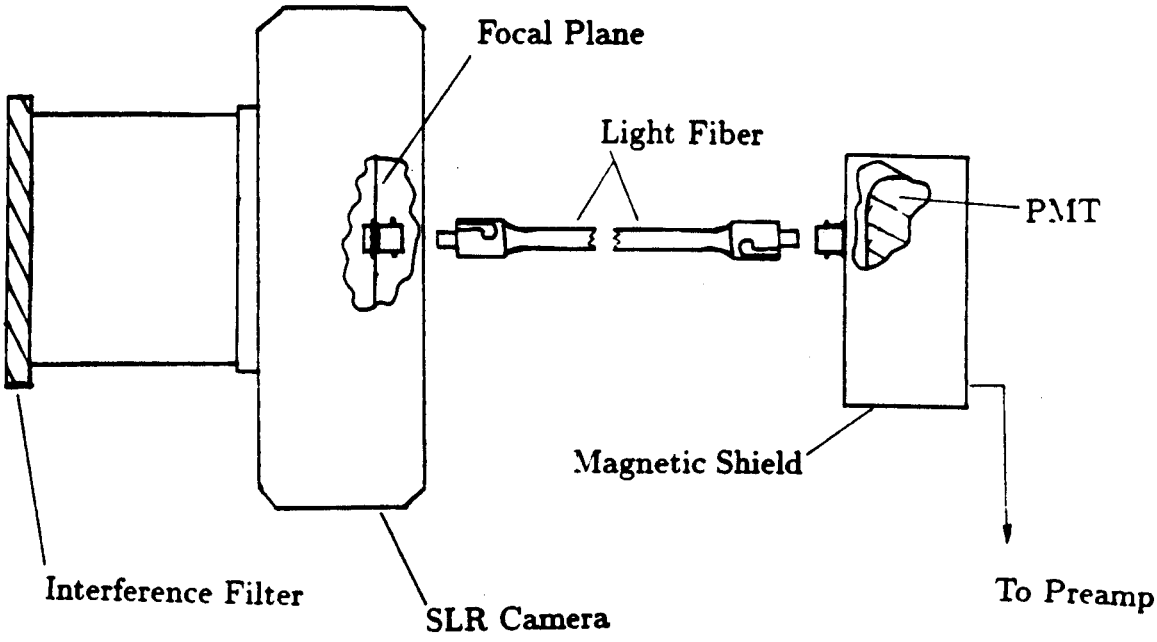

Figure 2.3 — Schematic of single channel detector system.

is converted to voltage (10^6 V/A, $\tau_{RC} = 100\,\mu$s) and then digitized at 5 kHz.

For typical Alcator C parameters of $\overline{n_e} = 2 \times 10^{14}\,\mathrm{cm}^{-3}$, $T_{e0} = 1500$ eV, and $Z_{\mathrm{eff}} = 1$, the central chord bremsstrahlung power collected by this system ($\lambda = 5360$Å, $\Delta\lambda = 30$Å is 2.9×10^{-11} W (8.1×10^7 photons/sec).

Because of the compact size of the camera body and the built-in viewfinder, this detector system is relatively easy to calibrate and align, and is routinely used to measure Z_{eff} .

2.4 16-Channel Detector System

The 16-channel detector system consists of a modified 35 mm SLR Pentax camera body with an array of 16 PIN photodiodes (.25 cm × 3.0 cm) mounted at the image plane (see Fig. 2.4). A 5500 Å, 600 Å FWHM interference filter is positioned in front of the 200 mm-focal-length lens which focuses the light onto the photodiodes. This provides a spatial resolution of .83 cm at the center of the plasma. Current from the photodiodes is converted to voltage (4×10^7 V/A, $\tau_{RC} = 1$ ms), and then digitized at 5 kHz.

PIN Photodiodes:

The 16-channel detector system uses PIN photodiodes to detect visible continuum radiation. PIN photodiodes consist of thin Si chips with a *p*-type region, an intrinsic (Si) region, and a *n*-type region. An electron-hole pair is created when a photon of sufficient energy knocks an electron into the conduction band of the semiconductor. The electron-hole pair is then separated by the internal electric field in the intrinsic region and collected as current.

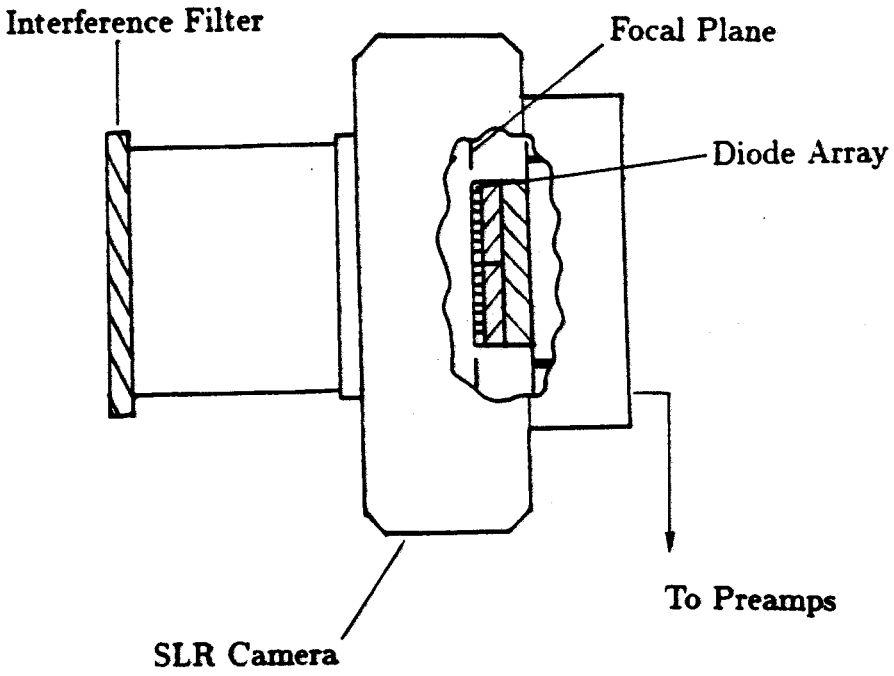

Figure 2.4 — Schematic of 16-channel detector system.

Photodiodes typically have peak quantum efficiencies in the range of 40% to 70% – significantly higher than PMTs. However, since photodiodes have no internal gain, they require high gain, low noise amplification for detecting weak light intensities.

This detector system uses UDT A4C-8PL photodiodes which have quantum efficiencies of 55% at 5500 Å. The active areas of each photodiode is $4.3\,\mathrm{mm}^2$. For typical Alcator C parameters of $\overline{n_e} = 2 \times$

$10^{14}\,\mathrm{cm}^{-3}$, $T_{e0} = 1500\,\mathrm{eV}$, and $Z_{\mathrm{eff}} = 1$, the central chord bremsstrahlung power detected by this system ($\lambda = 5500\text{Å}, \Delta\lambda = 600\text{Å}$) is $3.8 \times 10^{-8}\,\mathrm{W}$ (1.0×10^{11} photons/sec).

2.5 Temporal Responses

The maximum time response of each detector system, Δf_{max}, is defined here as the maximum filtering bandwidth which results in a signal-to-noise ratio (SNR) greater than 1. Δf_{max} is dependent on both the the efficiency and type of photodetector used, and is generally limited by the total collected flux (photons/sec) of the optical system.

The two detector systems which are described in sections 2.2 and 2.3 use PMTs to detect the incident light flux and amplify the photoelectron current. Since the PMT dark noise and pre-amplifier noise are relatively small, the photon statistical noise determines the SNR. This type of noise is due to the statistical fluctuations in the number of photons/sec emitted from the plasma (proportion to the square-root of the photon flux) and, in the number of photoelectrons emitted per incident photon from the photocathode. Since quantum efficiencies for PMT's are generally much less than unity, the photoelectron emission statistics of the PMT determines the SNR of the signal. Therefore, Δf_{max} is approximately the photocathode emission frequency and, for constant bandwidth, the SNR is proportional to the square-root of the incident light flux.

For typical Alcator C parameters of $\overline{n_e} = 2 \times 10^{14}\,\mathrm{cm}^{-3}$, $T_{e0} = 1500\,\mathrm{eV}$, and $Z_{\mathrm{eff}} = 1$, the central chord bremsstrahlung power collected by the 20-channel system (etendue $= 1.5 \times 10^{-4}\mathrm{cm}^2\mathrm{sr}$) is $4.2 \times 10^{-10}\,\mathrm{W}$ (1.1×10^{9} photons/sec). This corresponds to a cathode emission frequency of 3.4×10^{7} electrons/sec. Thus, $\Delta f_{\mathrm{max}} = 3.4 \times 10^{7}\,\mathrm{Hz}$ for bremsstrahlung emissions at these plasma densities and temperatures. The central chord bremsstrahlung power collected by the single channel system (etendue $= 1.1 \times 10^{-5}\mathrm{cm}^2\mathrm{sr}$) is $2.9 \times 10^{-11}\,\mathrm{W}$ (8.1×10^{7} photons/sec). This corresponds to a cathode emission frequency of 9.7×10^{6} (electrons/sec). Thus, $\Delta f_{\mathrm{max}} = 9.7 \times 10^{6}\,\mathrm{Hz}$ for bremsstrahlung emissions at these plasma densities and temperatures.

In section 2.4, a 16-channel detector system is described which uses PIN photodiodes as detectors. In these high quantum efficient ($\simeq$ .6), unity gain photodetectors, the noise in the diode and/or electronics dominates the SNR of this system. For the SNR to be greater than unity, the incident light power must be greater than the noise equivalent power (NEP) of the detector system. The NEP of these photodiodes is proportional to $\sqrt{\Delta f}$. Thus, Δf_{max} (which is Δf when SNR =1 or equivalently when the incident light power equals the NEP) is proportional to the square of the incident light flux. For constant bandwidth, the noise is constant so that the SNR is proportional to the incident flux.

The NEP of the system is measured to be approximately $6 \times 10^{-10}\,\mathrm{W}$ for $\Delta f = .16\,\mathrm{kHz}$ (NEP $\simeq 4.7 \times 10^{-11}\sqrt{\Delta f}\,\mathrm{W}$).

For typical Alcator C parameters of $\overline{n_e} = 2 \times 10^{14}\,\mathrm{cm}^{-3}, T_{e0} = 1500\,\mathrm{eV}$, and $Z_{\mathrm{eff}} = 1$, the central chord bremsstrahlung power detected by this system (etendue $= 7.0 \times 10^{-4}\mathrm{cm}^2\mathrm{sr}$) is $3.8 \times 10^{-8}\,\mathrm{W}$

$(1.0 \times 10^{11}$ photons/sec). Δf_{max} at these plasma densities and temperatures is $(3.8 \times 10^{-8}/4.7 \times 10^{-11})^2 = 6.5 \times 10^5\,\mathrm{sec}^{-1}$.

Although the photon flux and the bandwidth of the detector system determine the SNR, very small amplitude variations can still be detected by using synchronous averaging techniques. This method is used in Chapter 4 to detect small (0.5%) sawteeth oscillations on the central chord continuum brightness.

2.6 Absolute Calibration

In order to obtain accurate, absolute brightness measurements, the detector systems were calibrated with a tungsten lamp of known spectral brightness. As is shown below, accurate line-integral plasma emissivities are obtained by comparisons with the results of this absolute calibration.

The output signal S_{cal} (in volts) from a detector system whose detector is focused on the calibration lamp's filament (filled etendue) is given by:

$$S_{cal} = \int_{A_{lens}} \overline{\Omega}(\theta) \cdot d\overline{S} \int_0^\infty B_{cal}(\lambda) F(\lambda) R(\lambda) d\lambda \qquad (2.2)$$

where the first integral is the solid angle from lens area dS, subtended by the detector at angle θ, integrated over the projected lens area. $B_{cal}(\lambda)$ is the brightness of the calibration lamp at wavelength λ, and $F(\lambda)$ is the filter's spectral transmission. $R(\lambda)$ is the product of the spectral responses of the lens, light pipes (used in the 20-channel and single channel system), and detectors (PMTs or photodiodes), and the gain of the amplifier (V/A).

The single channel and 20-channel detector systems were calibrated in this manner, while the 16-channel detector system (whose etendue could not be filled by the thin calibration filament) was cross-calibrated against the single channel detector system's response to a diffuse source.

The brightness B (photons /unit time/solid angle/wavelength/unit projected area) from a plasma is given by the line-integral of the emissivity

E(photons /unit time/solid angle/wavelength/ unit volume) along the line of sight through the plasma,

$$B(\lambda) = \int_{\mathrm{L}} E(\lambda, \bar{\varepsilon}) dl \tag{2.3}$$

where $\bar{\varepsilon}$ is the position (r, θ) along the emission chord L through the plasma with respect to the plasma center r=0. Actual brightness measurements have finite spatial resolution, so that Eq. 2.3 is only accurate when the spatial resolution is smaller than the spatial scale length. This is easily satisfied for the typical $\simeq$ 1 cm spatial resolution of these detector systems.

The output signal S_{brem} (in volts) from the same detector system measuring the bremsstrahlung brightnesses from a plasma is

$$S_{\mathrm{brem}} = \int_{A_{\mathrm{lens}}} \bar{\Omega}(\theta) \cdot d\bar{S} \int_{\mathrm{L}} E_{\mathrm{brem}}(\lambda_0, \bar{\varepsilon}) dl \int_0^{\infty} e(\lambda) F(\lambda) R(\lambda) d\lambda \tag{2.4}$$

where $e(\lambda)$ is the bremsstrahlung wavelength dependence ($e(\lambda) = \lambda_0/\lambda$), λ_0 is the wavelength at which $F(\lambda)R(\lambda)$ is maximum, and $E_{\mathrm{brem}}(\lambda_0, \bar{\varepsilon})$ is the bremsstrahlung emissivity at wavelength $\lambda = \lambda_0$ from position $\bar{\varepsilon}$ in the plasma.

Combining Eqs. 2.2–2.4, the bremsstrahlung brightness is written as:

$$B_{\text{brem}}(\lambda_0) = \int_L E_{\text{brem}}(\lambda_0, \bar{z}) dl = B_{\text{cal}}(\lambda_0) g_\lambda \frac{S_{\text{brem}}}{S_{\text{cal}}} \tag{2.5}$$

where g_λ is the wavelength form-factor defined as:

$$g_\lambda = \frac{\int_0^\infty \frac{B_{\text{cal}}(\lambda)}{B_{\text{cal}}(\lambda_0)} F(\lambda) R(\lambda) d\lambda}{\int_0^\infty e(\lambda) F(\lambda) R(\lambda) d\lambda} \tag{2.6}$$

For the 16 channel detector system, which uses a 5500 Å, 600 Å FWHM filter and PIN photodiode detectors, g_λ was calculated to be approximately 0.98.

The other two detector systems use 30 Å FWHM filters. Since the spectral variation of $R(\lambda)$) is small over this small wavelength region, a good approximation is to let $F(\lambda) = \Delta\lambda F_0 \delta(\lambda_0 - \lambda)$. From Eq. (2.6), $g_\lambda = 1$, where λ_0 is now the peak transmission of the interference filter. Eq. 2.5 is simplified to:

$$B_{\text{brem}}(\lambda_0) = \int_L E_{\text{brem}}(\lambda_0, \bar{z}) dl = B_{\text{cal}}(\lambda_0) \frac{S_{\text{brem}}}{S_{\text{cal}}} \tag{2.7}$$

Uncertainties in the absolute calibration are small due to the easy availability of well calibrated sources in the visible wavelength region. The uncertainty in the brightness of the calibration lamp used in calibrating these detector systems is given as $\leq 3\%$.

Thus, accurate line-integral emissivities are obtained by comparisons of measured brightness with the results of absolute calibration.

CHAPTER 3

Impurity Measurements

3.1 Motivation for Impurity Studies

This chapter describes how $Z_{\rm eff}$, the average plasma ionic charge, is obtained from visible continuum measurements, and presents the effects of changes in various plasma conditions on $Z_{\rm eff}$. The definition of $Z_{\rm eff}$ was shown in Chapter 1 to arise naturally from the bremsstrahlung emissivity of a multiple ion-species plasma,

$$Z_{\rm eff} \equiv \frac{\sum n_i Z_i^2}{\sum n_i Z_i}. \tag{3.1}$$

$Z_{\rm eff}$ provides a good estimate of the overall plasma purity, since it depends on a sum over all the ions in the plasma. In cases where the dominant impurity is known, approximate impurity concentrations can be inferred. $Z_{\rm eff}$ measurements are also sometimes needed to interpret correctly the results from other diagnostics, such as T_i from neutron flux measurements.

The role of controlling impurities in future fusion reactors will be an important one. Sudden introductions of impurities from the plasma edge can radiatively cool the current channel sufficiently to cause major plasma disruptions. Disruptions can result in structural damage to the limiter and vacuum wall due to thermal deposition and due to forces caused by large induced currents. Possible damage to the vacuum vessel and blanket structure due to disruptions is therefore a major concern to the designers of future large experimental tokamaks[22].

The presence of small concentrations of background impurities in reactor-grade plasmas is equally detrimental. For example, a .01% Mo contamination increases the minimum temperature required for ignition from 4.4 keV to 10 keV for a D–T fusion reactor, while a .2% Mo plasma will not ignite at any temperature[1]. Given the present-day, low efficiency heating results from both RF and NBI (neutral beam injection) experiments, the effectiveness in maintaining low levels of impurities may be decisive for achieving the high temperatures needed for ignition.

The introduction of impurities into the plasma is generally due to the 10–20 eV edge plasma interacting with nearby materials such as limiters, the vacuum chamber wall, rf antennae, and edge diagnostics. One major plasma-wall interaction, believed to be important in explaining the high impurity levels during low density Alcator C discharges, is sputtering on the limiter surfaces due to background and impurity ions[25]. Enhanced run-away electron populations, most prevalent at low densities, or during strong lower-hybrid RF current drive, can also lead to large increases in the influx of limiter material, probably due to increases in evaporation and melting. Other processes, such as blistering may also be important mechanisms for introducing unwanted impurities into the plasma[26].

In section 3.2, the method used for obtaining $Z_{\rm eff}(r)$ profiles and the line-average $Z_{\rm eff}$ is described. Section 3.3 presents a comparison between enhancements of the resistivity over Spitzer[46], as inferred from $Z_{\rm eff}$ measurements and as inferred from loop voltage and T_e measurements. This provides an independent check of $Z_{\rm eff}$ measurements. In

Section 3.4, the effects of N_2 injection on $Z_{\rm eff}(r)$ are presented. In Section 3.5, uncertainties in the $Z_{\rm eff}$ measurements are discussed.

3.2 $Z_{\rm eff}$ Inferred from Continuum Measurements

$Z_{\rm eff}$ can be inferred from visible continuum measurements when independent electron temperature and electron density measurements are available. From Eq. 1.5, $Z_{\rm eff}(r)$ can be written as,

$$Z_{\rm eff}(r) = \frac{\lambda_0}{C_b} \frac{T_e^{1/2}(r)\ E_{\rm brem}(\lambda_0, r)}{n_e^2(r)\ \bar{g}_{\rm ff}(T_e(r))\ e^{-hc/\lambda_0 T_e(r)}} \tag{3.2}$$

The brightness profiles are least-squares fitted with Fourier-Bessel series of the form: $B(r) = \sum a_n J_0(\nu_n r/a)$, where J_0 is the zero-order Bessel function with $B(a) = 0$. The Abel inversion is then given as $E_{\rm brem}(r) = \sum a_n A_n(\nu_n r/a)$, where A_n is the Abel inversion of $J_0(\nu_n r/a)$. Electron density profiles $n_e(r)$ are obtained by Abel inverting 5–chord interferometer data. Electron temperature diagnostics which are frequently available on Alcator C are Thomson scattering, electron cyclotron emission, and soft-xray spectrum measurements. These measurements of $T_e(r)$, $n_e(r)$, and $E_{\rm brem}(r)$ are then used to determine $Z_{\rm eff}(r)$.

A typical $Z_{\rm eff}(r)$ profile for a moderate density discharge is shown in Fig. 3.1. $Z_{\rm eff}(r)$ is seen to be approximately flat out to the relative radius r/a = 0.75. At these densities the dominant impurities are probably due to low to medium Z ions – like carbon or oxygen[27]. For typical $T_{eo} = 1 - 2$ keV discharges, these impurities are fully ionized over the much of the central plasma core. Since the electron density

profiles during non-pellet fueled discharges are usually found to quite flat, these measurements of $Z_{\rm eff}(r)$ imply that the fully-stripped, low Z impurities also have centrally flat profiles.

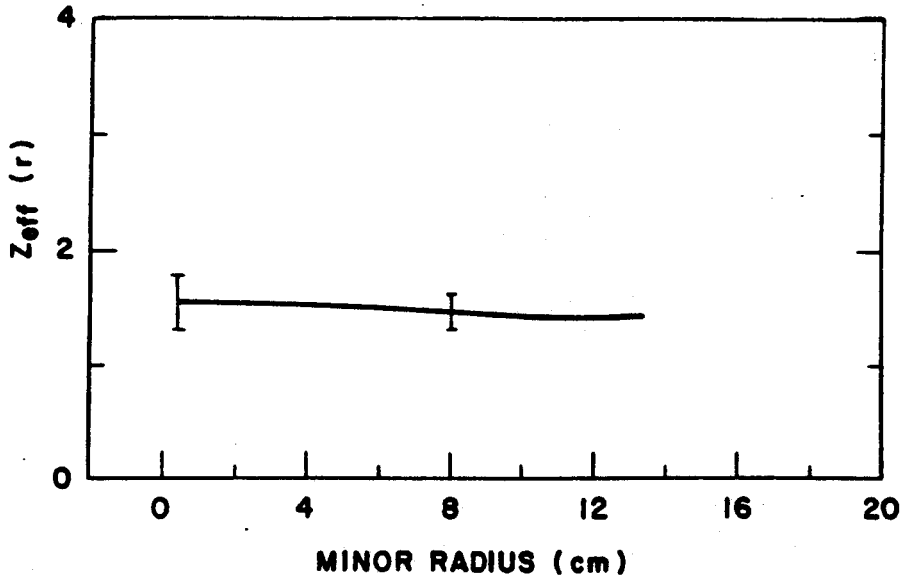

Figure 3.1 — Typical $Z_{\rm eff}(r)$ profile during the steady-state portion of an ohmically heated discharge. Relative profile uncertainties are estimated to be $\simeq \pm 16\%$ near r=0 and $\simeq \pm 12\%$ near r/a = 0.5.

A 'line-average' $Z_{\rm eff}$ is defined as,

$$\overline{Z}_{\rm eff} = \frac{\lambda_0}{C_b} \frac{T_{e0}^{1/2}\ B_{\rm brem}(\lambda_0, z=0)}{\overline{n}_e^2\ \overline{g}_{\rm ff}(T_{e0})\ e^{-hc/\lambda_0 T_{e0}}} \frac{2a}{f_z} \tag{3.3}$$

where z=r/a, $B_{\rm brem}(\lambda_0, z=0)$ is the central chord (z=0) bremsstrahlung brightness (see Eq. 2.7), and $\overline{n}_e$ is the central line average electron

density. f_z is a profile form-factor function, which is weakly dependent on the density and temperature profiles, and is defined as:

$$f_z = \frac{\int_0^1 \frac{n_e^2(z)}{n_{e0}^2} \frac{T_{e0}^{1/2}}{T_e(z)^{1/2}} \frac{\bar{g}_{ff}(T_e(z))}{\bar{g}_{ff}(T_{e0})} \frac{e^{-hc/\lambda_0 T_e(z)}}{e^{-hc/\lambda_0 T_{e0}}} dz}{(\int_0^1 \frac{n_e(z)}{n_{e0}} dz)^2} \tag{3.4}$$

For typical density and temperature profiles, $n_e = n_{eo}(1-(r/a)^2)^{1/2}, T_e = T_{eo}\exp(-r^2/(.55a)^2)$, $f_z = 1.4$ and varies $\pm$ 10% over a wide range of density and temperature profile shapes, as shown in Fig 3.2.

$\overline{Z}_{\rm eff}$ is defined such that it depends only on directly measured parameters: $\bar{n}_e$ (from the central-chord FIR interferometer); $B_{\rm brem}(\lambda_0)$; and T_{e0} (obtainable from soft xray spectra). Each of these is available without inversions of multi-chord data. $\overline{Z}_{\rm eff}$ is therefore free from the inherent uncertainties of Abel inversions and is generally easier to obtain.

To elucidate the physical relationship between $\overline{Z}_{\rm eff}$ and $Z_{\rm eff}(r)$, Eq. 3.3 is rewritten as

$$\overline{Z}_{\rm eff} = \frac{\int_0^1 Z_{\rm eff}\ (z)\ W(z)\ dz}{\int_0^1 W(z)dz} \tag{3.5}$$

where W(z) is a weighting function defined as,

$$W(z) \quad \frac{n_e^2(z)\ \bar{g}_{ff}(T_e(z))\ e^{-hc/\lambda_0 T_e(z)}}{T_e^{1/2}(z)} \tag{3.6}$$

Thus, $\overline{Z}_{\rm eff}$ is the chordal average of $Z_{\rm eff}(r)$, weighted approximately by $n_e^2/T_e^{1/2}$. For typical Alcator C temperature and density

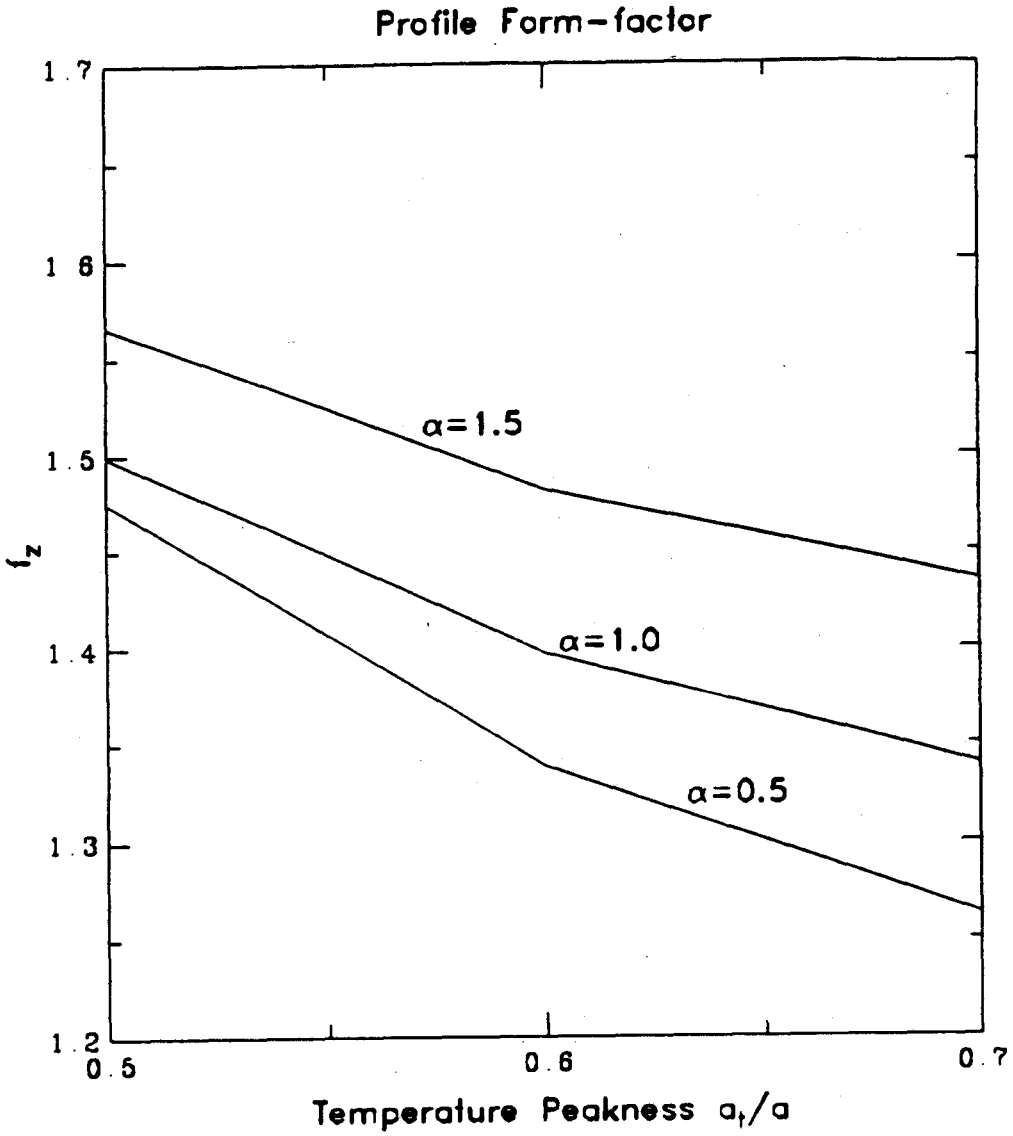

Figure 3.2 — Profile form-factor for typically measured profile range $n_e = n_{eo}(1-(r/a)^2)^\alpha, \alpha = 0.5,\ 1.0,\ 1.5$, and $T_e = T_{eo}exp(-r^2/a_T^2)$. $.5a \leq a_T \leq .7a$. $T_{eo} = 1500$.

profiles, $n_e^2/T_e^{1/2}$ usually has only a weak spatial dependence. In these cases, $\overline{Z}_{eff}$ is approximately equal to the non-weighted chordal average of $Z_{eff}(r)$.

During the steady-state portion of ohmic discharges, central temperatures $T_{e0(SS)}$ can be determined from analysis of the soft x-ray spectrum. In cases where this diagnostic is not available, a fairly accurate ($\pm$ 10%) empirical formula for $T_{e0(SS)}$ has been calculated from regression analysis of previous data[28]:

$$T_{e0(SS)} = 17.9\ B_t^{.6}\ I_p^{.4}\ M^{.3}\ a^{.3}\ \overline{n}_e^{-.3} \tag{3.7}$$

with $T_{e0(SS)}$ in eV, B_t in T, I_p in kA, a in cm, $\overline{n}_e$ in 10^{14}cm^{-3}, and M is the mass of the majority ion species in AMU.

Central ECE measurements, normalized to $T_{e0(SS)}$ during the steady-state portion of the discharge, are used to determine $T_{e0}(t)$. During ohmically heated, non-pellet fueled plasmas, central ECE measurements have also been found to be approximately proportional to the plasma current, $I_p(t)$, during most of the discharge. Thus, in cases where ECE measurements are not available, $T_{e0}(t)$ is assumed proportional to $I_p(t)$ and then normalized to $T_{e0(SS)}$ during the steady-state portion of the discharge. $\overline{Z}_{eff}(t)$ is routinely monitored on Alcator C by this technique and provides a relatively easy and reliable method for diagnosing variations in the impurity level of the plasma. Fig 3.3 shows $\overline{Z}_{eff}(t)$ for

a high density ($\overline{n}_e$ =3.4 $\times 10^{14}$ cm^{-3}) discharge, where $T_{e0(SS)}$ is determined from soft-Xray measurements.

The strongest variation of $\overline{Z}_{\text{eff}}$ on background plasma parameters is found to be with electron density, especially for lower densities $\overline{n_e} \leq$ 2 $\times 10^{14}$ cm^{-3}. Fig 3.4 shows a plot of $\overline{Z}_{\text{eff}}$ vs. $\overline{n_e}$, measured during the steady-state portion of each discharge in which the limiter material was molybdenum. In high density discharges where $\overline{n_e} \geq 3 \times 10^{14}$ cm^{-3}, $\overline{Z}_{\text{eff}}$ is typically ≤ 1.2 in hydrogen and deuterium discharges, and ≤ 2.2 in helium discharges.

In lower densities discharges, $\overline{Z}_{\text{eff}}$ is typically much higher, in some cases as large as 10–15. This enhanced $\overline{Z}_{\text{eff}}$ at low densities may be due to enhanced Mo influxes which have been found at low densities[25]. Since the edge temperature is typically higher for low density plasmas, these enhanced Mo influxes were attributed to physical ion sputtering and self-sputtering of Mo from the Mo limiters[25].

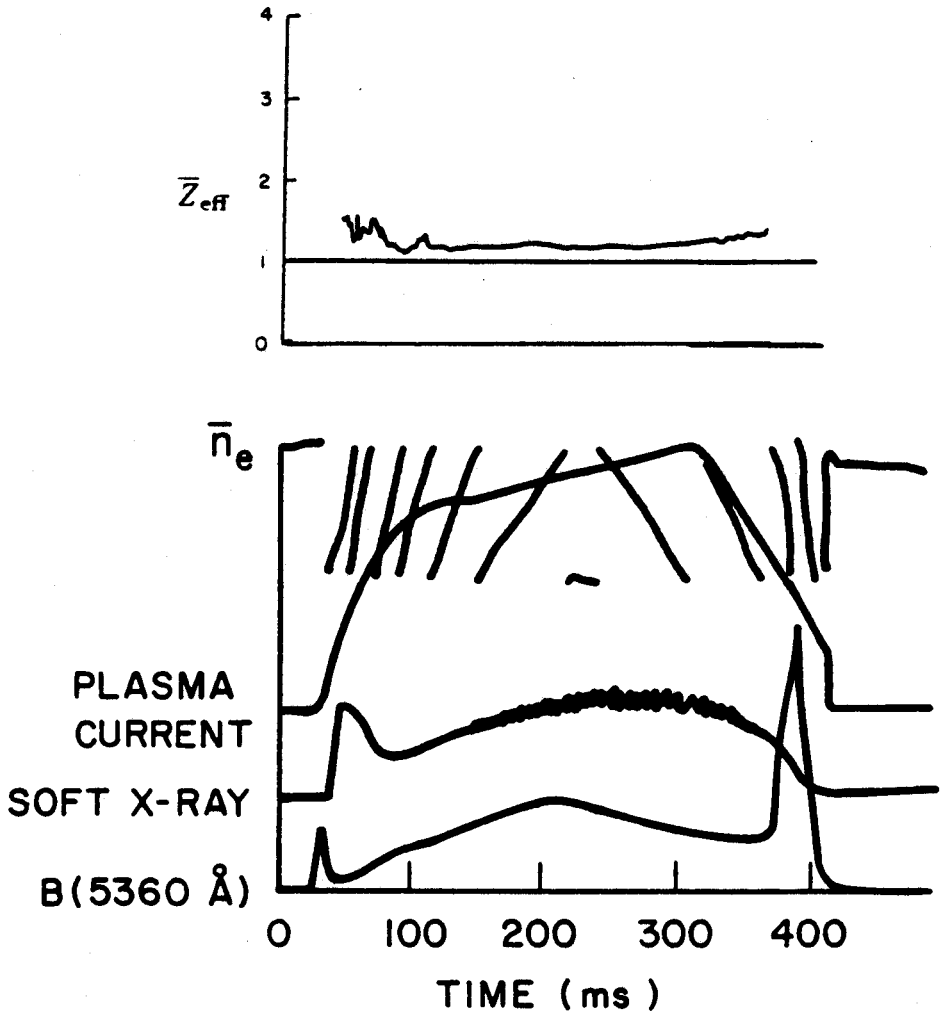

Figure 3.3 — $\overline{Z}_{eff}(t)$ for a typical high density, non-pellet discharge. Traces shown: line-average electron density (1 fringe = 6.5 $\times 10^{13}$ cm^{-3}), plasma current ($I_p(t = 300\text{ms})$=250 kA) soft X-ray brightness and visible continuum brightness ($B_{brem}(t = 220\text{ms})$ = 4.7 $\times 10^{11}$ photons/sec/cm^2/Å/sr). Enhancement of the continuum brightness due to marfe radiation is observed after $\sim$ 370 ms.

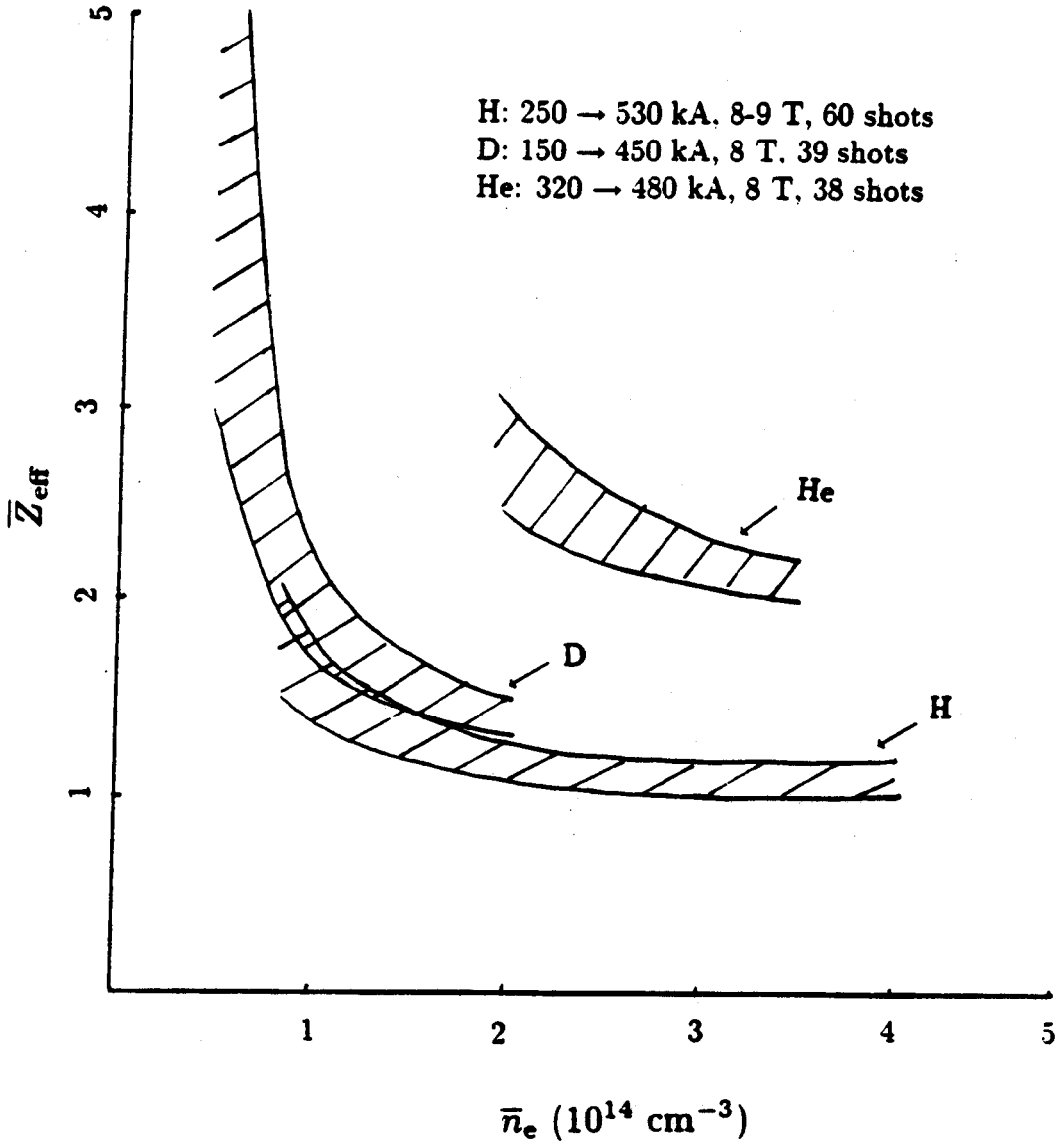

Figure 3.4 — $\overline{Z}_{eff}$, measured during the steady-state portion of the discharge with Mo limiters. Shaded areas represent the approximate scatter of data over the range of parameters listed. For $\overline{n_e} \geq 2 \times 10^{14}$ cm^{-3}, the scatter is approximately the same as the uncertainty in the measurement of $\overline{Z}_{eff}$ ($\pm 10\%$), as discussed in Section 3.5. $\overline{Z}_{eff}$ is seen to approach the background ionic charge, Z_i, as $\overline{n_e}$ increases, for all three background gases.

3.3 Comparisons with Resistivity Inferred $\overline{Z}_{eff}$

The plasma resistivity, η, can be calculated from measurements of Z_{eff} through

$$\eta = \eta_s A_z \tag{3.8}$$

where η_s is the Spitzer resistivity[46] for a hydrogenic plasma:

$$\eta_s = \frac{C_s ln\Lambda}{T_e^{3/2}} \quad (\text{ohm} - \text{cm}) \tag{3.9}$$

where $ln\Lambda$ is the Coulomb logarithm[29], $C_s = 9.0 \times 10^{-3}$,and T_e is in eV.

An analytical expression for A_z is given as[30]:

$$A_z = \frac{.914 Z_{eff}}{1.077 + Z_{eff}} + .58 Z_{eff} \quad . \tag{3.10}$$

The plasma resistivity, η, also can be estimated from measurements of the plasma loop voltage V_l.

$$\eta = E_{\|}/j \tag{3.11}$$

$$= \frac{\mu_o}{4\pi} \frac{V_l q_o}{B_t} \quad (\text{MKS}) \tag{3.12}$$

where q_o is the safety factor $q(r = 0)$. which for low β plasmas in cylindrical coordinates is defined as:

$$q(r) \equiv \frac{r B_t}{R_0 B_p(r)} \tag{3.13}$$

$$q(r = 0) \equiv q_o = \frac{2 B_t}{\mu_o R_0 j_o} \quad (\text{MKS}). \tag{3.14}$$

q_o cannot be directly ascertained without independent measurements of j(r), but for sawtoothing discharges, q_o should be close to or slightly less than one[3].

Using Eqs. 3.9 and 3.12, the ratio η/η_s can be calculated from measurements of T_{e0} and V_l, assuming $q_o \simeq 1.0$. This ratio can also be calculated using the continuum inferred Z_{eff} through Eqs. 3.8–3.10. Since η in Eqs. 3.9 and 3.12 are calculated at r= 0, corrections due to neoclassical effects are small. A comparison of these ratios is shown in Fig 3.5 where good agreement is found over the range $1 < \eta/\eta_s < 6.5$.

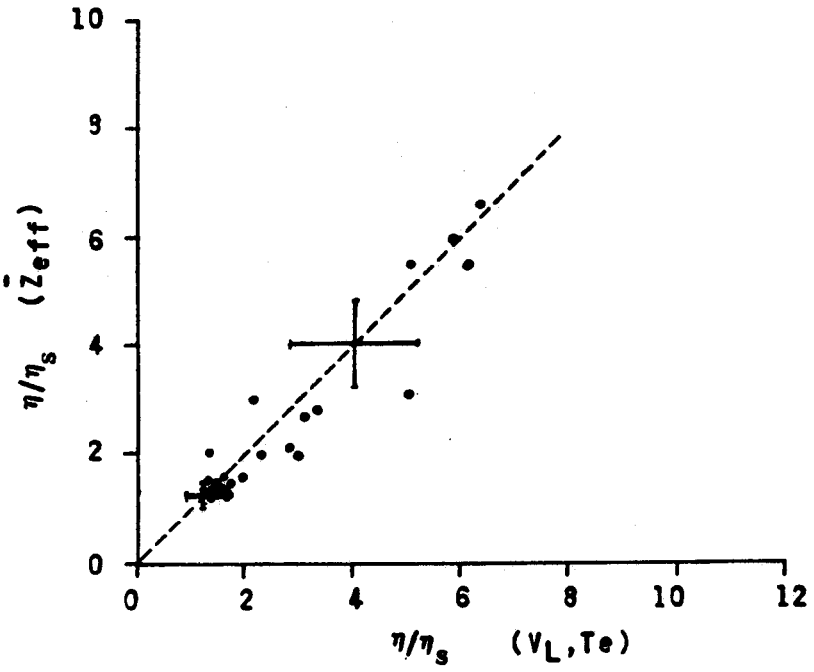

Figure 3.5 — Comparisons between η/η_s inferred from $\overline{Z}_{eff}$ measurements and inferred from V_l and T_e measurements during sawtoothing discharges. Error bars shown are estimated in Section 3.5

3.4 Nitrogen Injection Experiments

Nitrogen gas was injected into clean ($\overline{Z}_{\rm eff} \simeq 1.2$) background plasmas in order to study the time-evolution of the $Z_{\rm eff}(r)$ profiles. Shown in Fig 3.6 are $Z_{\rm eff}(r)$ profiles measured during one such discharge. $Z_{\rm eff}(r)$ is seen to remain flat or slightly peak as N_2 diffuses into the plasma, while $\overline{Z}_{\rm eff}$ increases from 1.2 to 1.4. These flat $Z_{\rm eff}(r)$ profiles imply an impurity profile distribution similar to that of the background gas, or $n_{\rm imp} \sim (1-(r/a)^2)^{.5}$. Neoclassical impurity transport predicts steady-state impurity profiles which are approximately the background ion profile to the power of the impurity charge $Z_{\rm imp}$. However, these results indicate that nitrogen transport is clearly non-classical, as must also be true of the intrinsic background impurities, although it is not clear what transport mechanisms are involved in producing these flat impurity profiles.

Impurity transport analysis of injected Si into Alcator also indicates non-classical impurity transport[31]. These experiments involved ablating a impurity coated glass slide with a laser pulse, and then observing the time responses of the brightnesses of the injected impurity lines. By comparing these measurements with results from an impurity transport code, transport coefficients consistent with the measurements were obtained. It was found from these comparisons that using a neoclassical form for the impurity flux, the measurements could not be qualitatively predicted. However, assuming a simple self-diffusion flux model $\Gamma_{\rm imp} = -D_{\rm imp}\frac{\partial n_{\rm imp}}{\partial r}$, the experimental data could be well fitted.

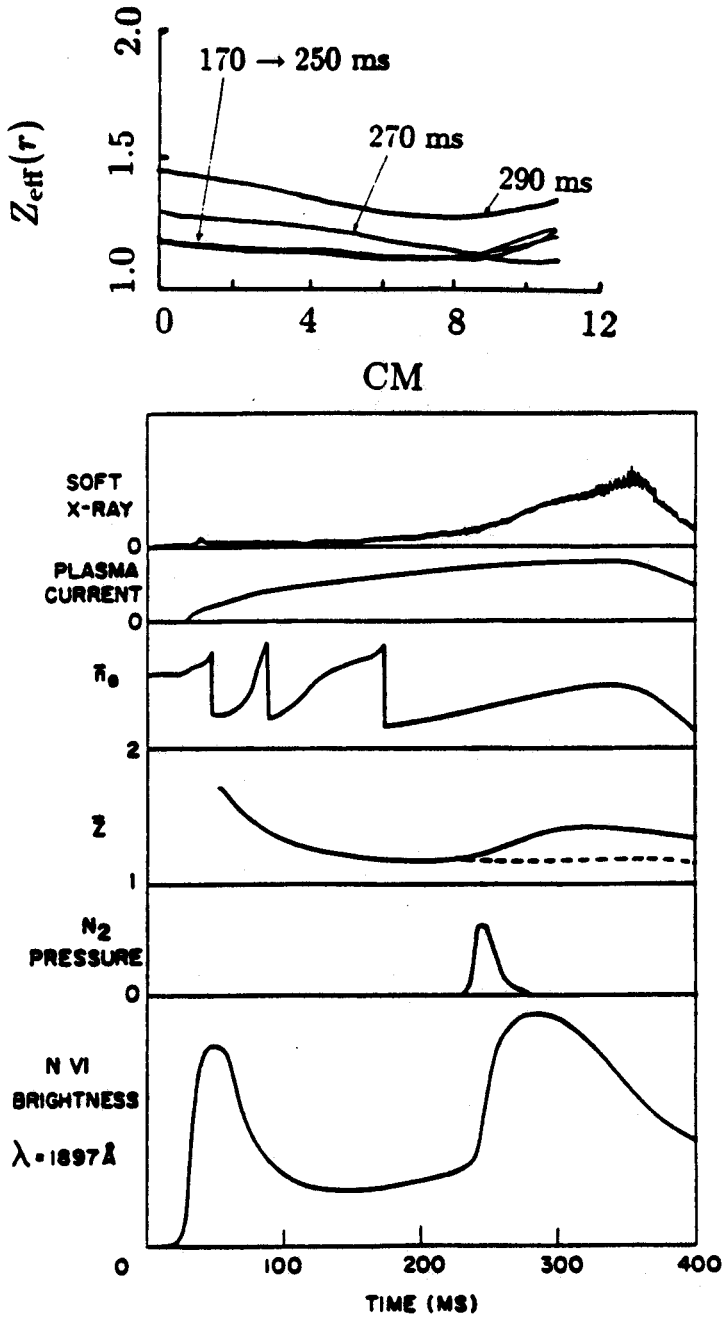

Figure 3.6 — $Z_{eff}(r)$ during N_2 injection experiments. N_2 is puffed at approximately 230 ms. The dashed curve of $\overline{Z}_{eff}$ was measured during shot with similar background parameter but with no N_2 puffing.

The $Z_{eff}(r)$ measurements during N_2 injections, are also consistent with this self-diffusion model, which predicts flat steady-state $Z_{eff}(r)$ profiles and no impurity accumulation.

3.5 Uncertainties in Z_{eff} Measurements

The uncertainties in obtaining $\overline{Z}_{eff}$ from continuum measurements are generally due to the experimental uncertainties in $\overline{n_e}$ and T_{e0} measurements, uncertainties in the absolute calibration ($< \pm$ 3%), and uncertainties due to non-bremsstrahlung enhancements such as recombination, line, and MARFE[34] radiation.

The uncertainty in the measurement of $\overline{n_e}$ is approximately 1/10 of an interferometer fringe or 6.5 $\times 10^{12}$ cm^{-3}. Thus, for very low densities ($\overline{n}_e \simeq$ 6.0 $\times 10^{13}$ cm^{-3}), the uncertainty in $\overline{n_e}$ is $\simeq \pm$ 15%. For higher density discharges ($\overline{n_e} \geq 3 \times 10^{14}$ cm^{-3}), the uncertainty in $\overline{n}_e$ is $\leq$ 2%.

For hot ($T_e \gg$ 10 eV) plasmas, visible bremsstrahlung radiation dominates recombination radiation. The relative contribution from recombination emission to the central-chord continuum brightness for typical Alcator C plasmas is estimated to be $\simeq$ 1%, while from a chord at impact radii r/a = .95 the contribution is $\simeq$ 3% (assuming $n_e \sim (1-(r/a)^2)^{1/2}, T_e = T_{eo} exp(-r^2/a_T^2), a_T = .5a, T_{eo} = 1500eV$).

The relative contributions from line radiation in the wavelength region of the interference filter can be roughly estimated from film spectrum analysis. Fig 1.4 shows the relative contribution from line emission to be $\leq$ 5% for 5000Å $\leq \lambda \leq$ 5600Å. This spectrogram was taken

over many discharges and indicates the impurity lines which are normally present in that wavelength region.

Another possible source of uncertainty is enhancement from MARFE[34,35] radiation (lower case 'marfe' will from now on be used). A marfe is an edge phenomena found on Alcator C and other tokamaks[36] which strongly emits both continuum and line radiation. Marfes are found to exist prevalently as a small toroidal band on the upper inside midplane of the torus, just inside the the poloidal limiter radius, and only occur during high density and/or low current discharges on Alcator C.

Thus, visible continuum brightnesses measurements from chords intersecting the marfe region can be greatly enhanced. Since the density, temperature and exact spatial extent of marfes are unknown, it is not possible to determine the fractional contribution to the continuum brightness from chords viewing the marfe region. However, since marfes are radially and poloidally localized, it is not difficult to determine whether a particular chord is viewing a marfe region. Therefore, bremsstrahlung emissivity profiles are obtained from Abel-inverting the brightnesses only from chords which do not intersect marfe regions. Since marfes are typically localized near the upper inside of the torus, the central-chord continuum brightness is seldom enhanced from marfe radiation. Thus, there is usually no influence on the $\overline{Z}_{\rm eff}$ measurement due to marfes during most of the discharge (see Fig. 3.3).

The uncertainties in $\overline{Z}_{\rm eff}$ due to multiple reflections are estimated to be small ($\simeq 10\%$). It was found that there were no significant differences in measurements of $\overline{Z}_{\rm eff}$ with a light dump installed, for similar background plasmas. Furthermore, the fact that $\overline{Z}_{\rm eff} \simeq 1.2$ during high density discharges (consistent with independent spectroscopic

measurements), also provides evidence that the effects of reflections are indeed small.

The overall uncertainties in $Z_{\rm eff}(r)$ measurements can be separated into a profile uncertainty and an absolute uncertainty. The absolute uncertainty is approximately the uncertainty of $\overline{Z}_{\rm eff}$. The total uncertainty of $\overline{Z}_{\rm eff}$ due to uncertainties in $\overline{n_e}$, T_{eo}, and $B_{\rm brem}$ is estimated to be $\pm$ 15% at high densities and $\pm$ 20% for lower densities ($\overline{n_e} \leq 6.0\times10^{13}$ cm^{-3}). For comparison, the uncertainty of $\overline{Z}_{\rm eff}$ determined from V_l and T_e measurements is estimated to be approximately $\pm$ 30%, assuming the uncertainty of q_o is $\pm$ 20% , T_{e0} is $\pm$ 10%, and V_l is $\pm$ 10%. These estimates of uncertainties are roughly consistent with the scatter of points shown in Fig 3.4.

The profile uncertainties in $Z_{\rm eff}(r)$ are due to uncertainties in the measured profiles of T_e, n_e, and $E_{\rm brem}$. T_e profiles can either be measured with a scanning Fabry-Perot or estimated from j(r), assuming $q_o \simeq 1$. The largest profile uncertainties in $Z_{\rm eff}(r)$ are a result of the Abel-inversions used to obtain $n_e(r)$ and $E_{\rm brem}(r)$. Small uncertainties in line-integral quantities result in large uncertainties in the Abel inverted profile, especially near r=0. In order to estimate these uncertainties, simulated brightness profiles with varying amounts of added 'noise' were Abel-inverted. A 15-point equi-spaced background profile of the form $B = B_o(1-(r/a)^2)^\beta$ was constructed. After a Gaussian-distributed random fluctuation was added to each channel, the resulting brightness profile was least-squares-fit with a Fourier-Bessel series. Using a typical RMS brightness fluctuation of $\simeq$ 3% ($\tau_{\rm smooth} = 100\mu s$),

a non-pellet peakedness (β =0.9), and a 3-term Fourier-Bessel LSF, average fluctuation of $E_{\rm brem}(r)$ was found to be $\simeq$ 7% at r=0 and $\simeq$ 5% at r/a=0.5. Larger values of β result in smaller fluctuation levels.

Increasing the smoothing time of the brightness signal will decrease the uncertainty in $E_{\rm brem}$. However, there is also an inherent uncertainty due to the finite number of chordal measurements. It is therefore important to choose correctly the number of Fourier-Bessel terms which are appropriate for the number and chordal locations of the brightness measurements. For most of the data presented in this thesis, 3 or 4 Fourier-Bessel terms are used. It is found that using more terms generally introduces harmonic artifacts, while using fewer terms result in inadequate fits to the brightness profiles.

In summary, the total uncertainty of $\overline{Z}_{\rm eff}$, due to uncertainties in $\overline{n_e}$, T_{eo}, and $B_{\rm brem}$ is estimated to be $\pm$ 15% at high densities and $\pm$ 20% for lower densities ($\overline{n_e} \leq 6.0\times10^{13}$ cm^{-3}). Assuming approximately the same uncertainty in $n_e(r)$ as $B_{\rm brem}(r)$, and an uncertainty in the profile shape of T_e of 5%, the relative uncertainty in $Z_{\rm eff}(r)$ is estimated to be $\simeq$ 16% at r=0 and $\simeq$ 12% at r/a=0.5.

3.6 Summary and Discussion

$Z_{\rm eff}(r)$ profiles have been obtained from Abel inversions of continuum brightness profiles, using independently measured $n_e(r)$ and $T_e(r)$. $\overline{Z}_{\rm eff}$, defined as a weighted line-average of $Z_{\rm eff}(r)$, is typically found to increase as $\overline{n_e}$ is lowered, probably because of enhanced sputtering of the limiter material. For high density discharges, $\overline{Z}_{\rm eff}$ is typically found to be $\simeq$ 1.2. The fact that $Z_{\rm eff}$ is so close to 1 in high density discharges

is the major motivation for using continuum measurements as a density diagnostic. Density profiles, obtained during high density, pellet fueled discharges are presented in Chapter 5.

Comparisons between η/η_s as inferred from T_e and V_l measurements, and η/η_s as inferred from continuum measurements, show good agreement for $1 \leq \eta/\eta_s \leq 6.5$. These comparisons provide confidence that the continuum brightness is dominated by bremsstrahlung emissions and that enhancements from impurity lines in the filter's passband are small.

Nitrogen gas injection experiments were performed in order to study the effects on the $Z_{\rm eff}$ profile. The results indicate that $Z_{\rm eff}(r)$ remains flat or slightly peaked during N_2 injection, while $\overline{Z}_{\rm eff}$ increases from 1.2 to 1.4. These $Z_{\rm eff}(r)$ profiles imply impurity profiles which are similar to the background plasma and must, therefore, have similar transport. This also indicates no strong ionic charge dependence on the steady-state impurity profile which is inconsistent with neo-classical impurity transport. A self-diffusion impurity transport model, which was found to be consistent with the transport of impurities on Alcator, is also consistent with the centrally flat steady-state $Z_{\rm eff}(r)$ profiles measured during N_2 injection.

The total uncertainty of $\overline{Z}_{\rm eff}$, due to uncertainties in $\overline{n_e}$, T_{eo}, and $B_{\rm brem}$ is estimated to be $\pm$ 15% at high densities and $\pm$ 20% for low densities ($\overline{n_e} \leq 6.0\times10^{13}$ cm^{-3}). The relative uncertainty in the $Z_{\rm eff}(r)$ profile shape is estimated to be $\simeq$ 16% at r=0 and $\simeq$ 12% at r/a=0.5.

CHAPTER 4

Detection and Analysis of Visible Continuum Sawteeth

4.1 Introduction and Motivation

In this chapter, the effects of internal disruptions on the visible continuum emission are presented[39]. Internal disruptions (sawteeth) in tokamak plasmas were first observed in 1974 by Von Goeler *et al.*[40] utilizing soft X-ray measurements. Soft X-ray sawtooth oscillations are also observed on Alcator C (see Fig. 4.1) during low $q_\ell (q_\ell \equiv 5a^2 B_T / R I_p \leq 5)$ discharges and are typically characterized by: 1) a sawtooth rise time in the range of 2 to 5 ms with a disruption time of about $100\mu s$; 2) a superimposed $m = 1$ oscillation preceding the disruption; 3) inverted sawteeth from chords outside the $q = 1$ radius. One major effect of the internal disruption is to flatten the density and temperature profiles approximately out to a mixing radius $r_m = \sqrt{2} r_s$[41], where $r_s < r_m < a$, and r_s is the $q = 1$ radius.

Sawteeth oscillations are often observed on many diagnostics, including the soft X-ray brightness, neutron flux (D_2 plasmas), and central electron cyclotron emission (ECE), and are usually indicative of a clean, non-disruptive discharge. The main purpose of this chapter is to explain why the effects of sawteeth are small on the visible continuum, but are nevertheless finite and observable. (However, as will be presented in Chapter 5, large sawteeth are sometimes observed for more highly peaked density profiles following a pellet injection.) This provides further proof that the visible continuum light is indeed coming

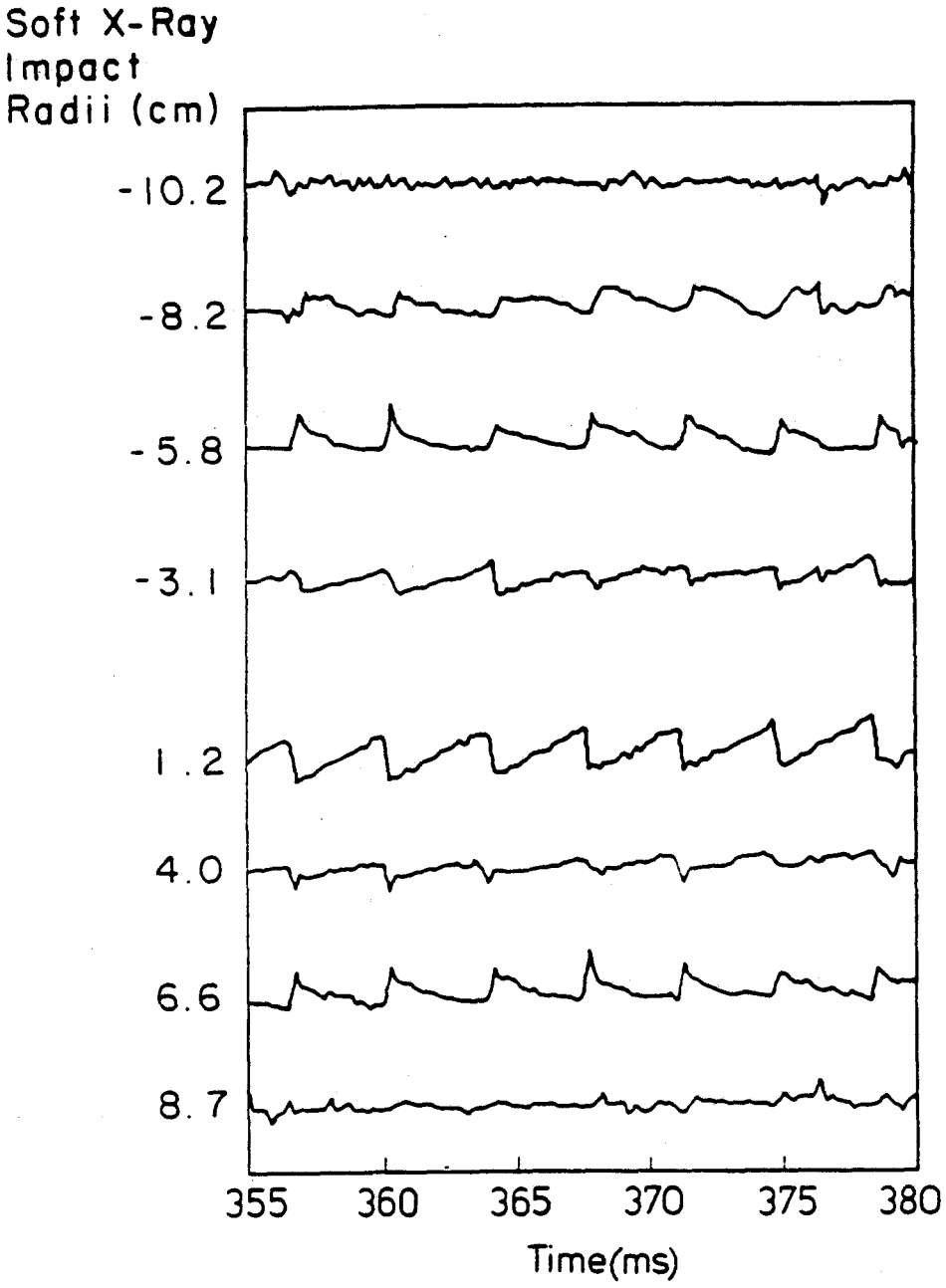

Figure 4.1 — Typical soft X-ray brightnesses from 8 different impact radii during a sawtoothing discharge in which a=16.5 cm and $r_m \simeq 8.5$ cm.

from the hot core of the discharge, and is not dominated by emission from the cold edge regions of the plasma. Traces of the visible continuum brightness, density, current, and central soft X-ray brightness during a sawtoothing discharge is shown in Fig 4.2.

As discussed in Section 2.6, the central-chord continuum brightness is equal to the line-integral bremsstrahlung emissivity,

$$B_{brem}(\lambda_o) = \frac{C_b}{\lambda_o} \int_{-a}^{a} \frac{n_e^2(r) Z_{eff}(r) \bar{g}_{ff}(T_e(r)) e^{-hc/\lambda T_e(r)}}{T_e^{1/2}(r)} dr \qquad (4.1)$$

During the high density ($\bar{n}_e \cong 2\times10^{14}\mathrm{cm}^{-3}$) steady state portion of the discharge, $Z_{eff}(r)$ is approximately constant ($\simeq 1.2$)[4] and will be assumed constant for this analysis. Since the Gaunt factor[8] and $e^{-hc/\lambda T_e(r)}$ vary only slowly with T_e in this wavelength and temperature region, the dominant terms which vary with radius in Eq. 4.1 are n_e^2 and $T_e^{1/2}$.

Since typical Alcator C density and temperature profiles, during non-pellet fueled discharges are $n_e(r) \simeq n_0(1-r^2/a^2)^{1/2}, T_e(r) \simeq T_{e0}(1-r^2/a^2)^2$, the continuum emission profile (approximately proportional to $n_e^2(r)/T_e^{1/2}(r)$) is expected to be centrally flat. A typical emission profile obtained from an Abel inverted brightness profile is shown in Fig. 4.3. Internal disruptions perturb n_e and T_e in the central region of the plasma, but since the emission profile is centrally flat, the effects on the central brightness B are small. However, by averaging over many sawteeth periods by the method described below, variations in the central continuum brightness yield $\Delta B/B \cong 0.5\%$.

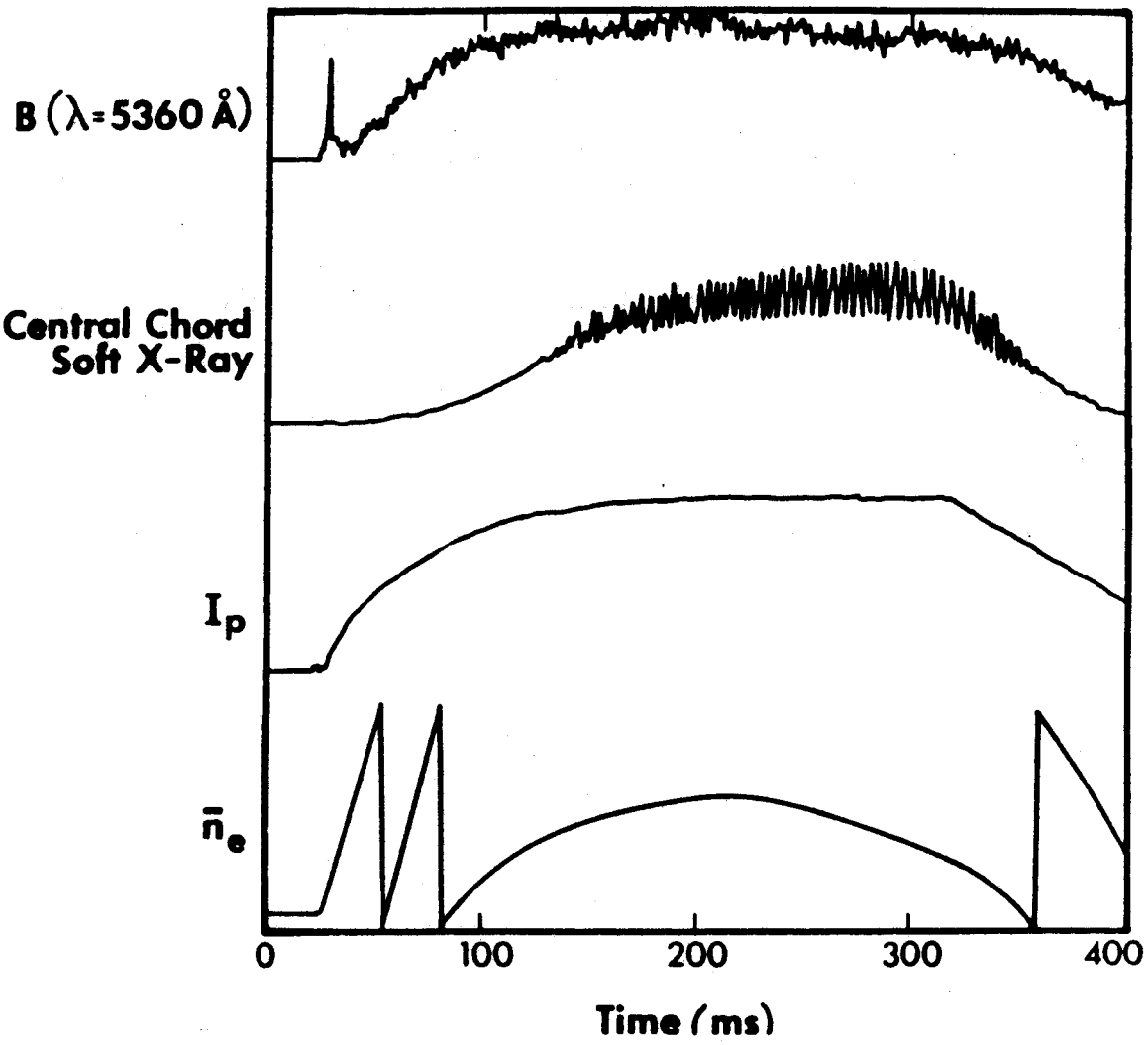

Figure 4.2 — Typical traces of the central chord visible continuum brightness (λ = 5360Å), central chord soft X-ray brightness, plasma current ($I_{max} \simeq 620$ kA), and central line-average density ($0.75 \times 10^{14} cm^{-3}$/fringe).

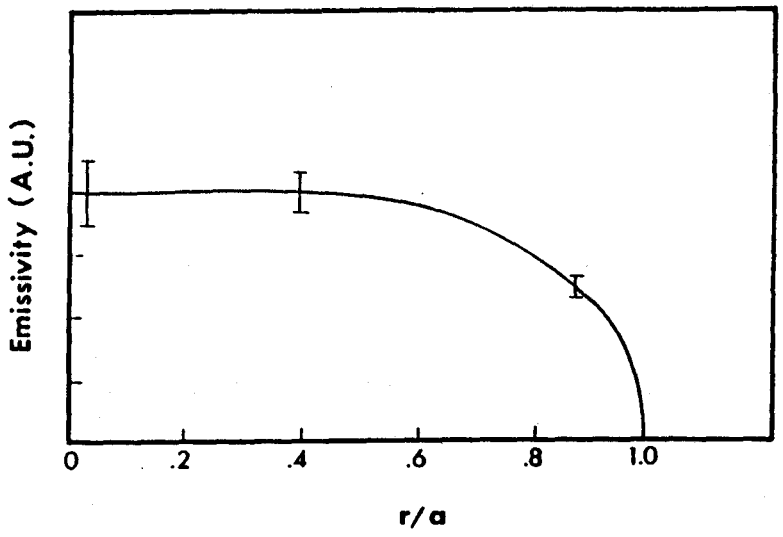

Figure 4.3 — Typical Abel inverted continuum emission profile. Since the central portion of the profile is usually quite flat, the effects of sawteeth are typically small on the central chord continuum brightness. Error bars are estimated from inversions of brightness fluctuations.

4.2 Method of Analysis

As shown in Fig. 4.2, the continuum brightness typically has a 3% - 5% RMS ($\nu \geq 50$ Hz) fluctuation component. This component is mostly composed of a 360 Hz fluctuation, probably due mainly to the slight plasma motion caused by the 360 Hz ripple component in the horizontal and vertical fields, and to fluctuations due to photon statistics. Both sources of 'noise' are uncorrelated with internal disruptions and can be eliminated by the averaging techniques described as follows.

The central-chord continuum brightness of the j-th shot is denoted $B_j(t)$, where $1 \leq j \leq M$ and M is the total number of shots analyzed. The central-chord soft X-ray crash time (time of the internal disruption) of the i-th sawtooth crash during the j-th shot is denoted t_{ij}, where $1 \leq i \leq N_j + 2$, and $N_j + 2$ is the total number of sawtooth crashes during the j-th shot. N_j is then the total number of sawtooth time periods for the j-th shot (between times $(t_{1j}+t_{2j})/2$ and $(t_{N_j+1j}+t_{N_j+2j})/2$). A sawtooth time period is defined as beginning at $t = (t_{ij} + t_{i-1j})/2$ and ending at $t = (t_{i+1j} + t_{i+2j})/2$ (see Fig. 4.4). By averaging the continuum brightness over a sufficient number of time periods, effects of internal disruptions on the continuum brightness are determined.

A smoothed brightness $\overline{B}_j(t)$ of the j-th shot is generated by first fitting a least squares second order polynomial $p(t')$ to $B_j(t')$ between times $t' = t - \tau_{SMj}/2$ and $t' = t + \tau_{SMj}/2$. τ_{SMj} is a smoothing time constant for shot j and is chosen to be about $4\tau_{STj}$, where τ_{STj} is the average sawtooth time period (as defined above) for shot j. The sawtooth period usually varies by less than 20% during most shots. $\overline{B}_j(t)$ is then equated to p(t' = t) and represents a smoothed ($\nu \leq 1/\tau_{SMj}$) brightness.

We now define:

$$\frac{\tilde{B}_j(t)}{\overline{B}_j(t)} \equiv \frac{B_j(t) - \overline{B}_j(t)}{\overline{B}_j(t)}$$

which represents the relative continuum brightness of shot j which has been effectively high pass filtered ($\nu \geq 1/\tau_{SMj}$). Between times $t = (t_{ij} + t_{i-1j})/2$ and $t = (t_{i-1j} - t_{i+2j})/2$, the $\tilde{B}_j(t)$ $\overline{B}_j(t)$ are summed into

a 21 bin array by first assigning $\tilde{B}_j(t^*)/\overline{B}_j(t^*)$ to the K-th bin element where:

$$t^* \equiv \left\{ (t_{ij} + t_{i+1j})/2 + (t_{i+2j} - t_{ij})\frac{K}{42} \right\}, \qquad 1 \leq K \leq 21.$$

The first term in the braces is the beginning time of the sawtooth period while the remaining term is the incremental time, which is K/21 of the sawtooth period duration. Since the data were digitized at 5 kHz, t^* is set to the nearest $200\mu s$. Figure 4.4 shows an example of assigning data to bins.

After summing over N_j and M, the total in each bin is divided by the total number of sawtooth periods added, T_M, where:

$$T_M \equiv \sum_{j=1}^{M} N_j.$$

The value in the K-th bin ($1 \leq K \leq 21$) after M shots is thus:

$$\tilde{f}_M(K) \equiv \frac{1}{T_M} \sum_{j=1}^{M} \sum_{i=1}^{N_j} \frac{\tilde{B}_j(t^*)}{\overline{B}_j(t^*)}.$$

In general, the relative brightness of shot j can be written as a sum of an uncorrelated component $U_j(t)$ and a correlated component $C_j(t)$, such that:

$$\frac{\tilde{B}_j(t)}{\overline{B}_j(t)} = U_j(t) + C_j(t).$$

The RMS value of the 21 bin array after adding M shots is:

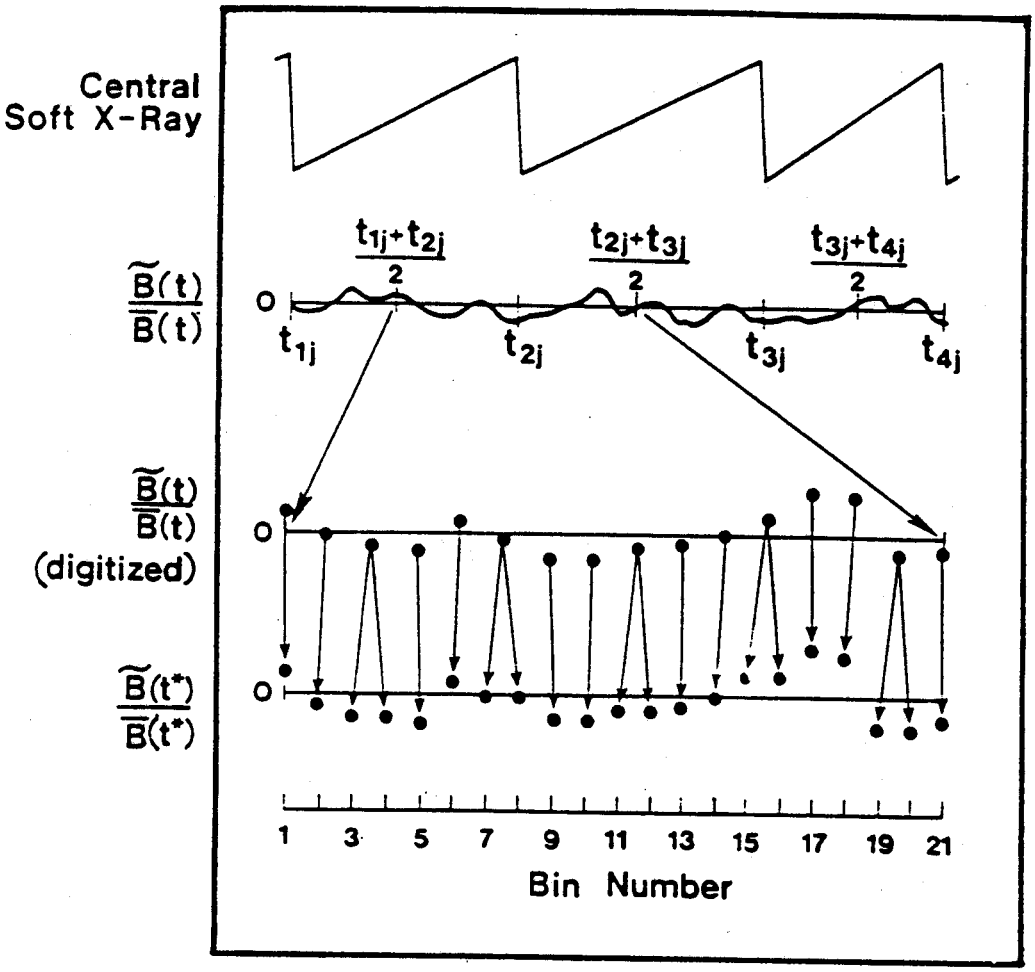

Figure 4.4 – $\tilde{B}(t)/\bar{B}(t)$ is summed into a 21 bin array for shot j. t_{ij} is the time of the i-th sawtooth crash for shot j. The continuum brightness (digitized at 5 kHz) between $(t_{ij} + t_{i-1j})/2$ and $(t_{i-1j} - t_{i-2j})/2$ is summed such that the closest data point to a particular bin is added to that bin.

$$\tilde{f}_{\mathrm{RMS}}(M) = \left[\frac{\sum_{\mathrm{K}=1}^{21}\left(\tilde{f}_{\mathrm{M}}(K)\right)^2}{21}\right]^{1/2},$$

$$= \frac{1}{T_{\mathrm{M}}}\left[\frac{\sum_{\mathrm{K}=1}^{21}\left(\sum_{\mathrm{j}=1}^{M}\sum_{i=1}^{N_{\mathrm{j}}} U_{\mathrm{j}}(t^*) + C_{\mathrm{j}}(t^*)\right)^2}{21}\right]^{1/2}.$$

For the case when $U_{\mathrm{j}} \gg C_{\mathrm{j}}$ and M (the number of shots) is small,

$$\tilde{f}_{\mathrm{RMS}}(M) \approx \frac{\overline{U}_{\mathrm{RMS}}}{\sqrt{T_{\mathrm{M}}}},$$

where $\overline{U}_{\mathrm{RMS}}$ is the average RMS value of $U_{\mathrm{j}}(t)$ after adding T_{M} sawteeth. Since $U_{\mathrm{j}}(t) \gg C_{\mathrm{j}}(t)$, $\overline{U}_{\mathrm{RMS}}$ is approximately the RMS value of $\tilde{B}(t)/\overline{B}(t)$. If $C_{\mathrm{j}}(t)$ has a sawtooth-like structure (see Fig. 4.5) which crashes from a relative amplitude $+C_0/2$ to $-C_0/2$, then for large T_{M}, $\tilde{f}_{\mathrm{RMS}}(M)$ should approach the RMS value of a sawtooth which is $(0.29)|C_0|$. Thus $\tilde{f}_{\mathrm{RMS}}(M)$ should approach a constant which is proportional to the sawtooth amplitude, after averaging over a sufficient number of sawtooth periods. For the sawtooth waveform described above, this 'sufficient' number is:

$$T_{\mathrm{M}} \gg \left(\frac{\overline{U}_{\mathrm{RMS}}}{(0.29)C_0}\right)^2.$$

For example, if $C_0 \cong 0.5\%$ and $\overline{U}_{\mathrm{RMS}} \cong 3\%$, then $T_{\mathrm{M}} \gg 428$. Since each shot only has from 30 to 60 sawteeth, many shots need to be averaged together.

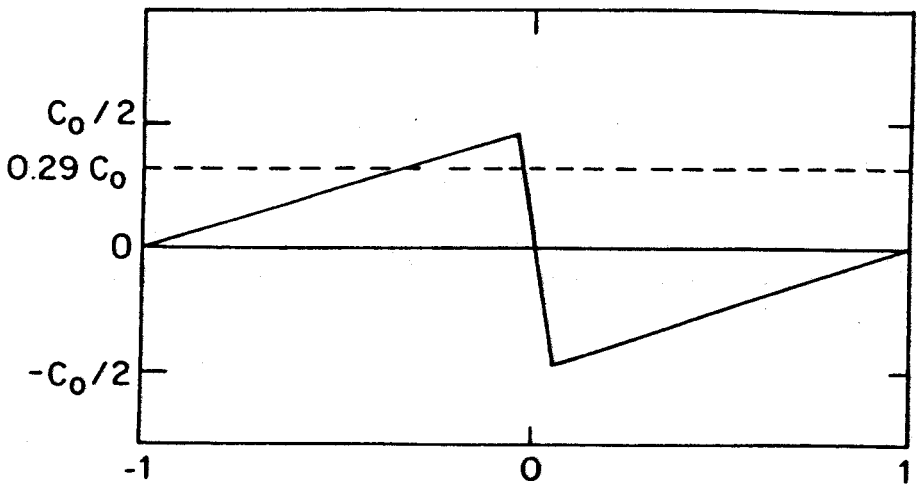

Figure 4.5 — A sawtooth waveform with an amplitude of C_0 has a RMS value of $(.29)C_0$. For large T_M, if $\tilde{f}_M(K)$ approaches this waveform, then $\tilde{f}_{RMS}(M)$ should approach $(.29)\,|\Delta B/B|$.

4.3 Experimental Results

Figure 4.6 shows the relative continuum fluctuation $\tilde{f}_M(K)$ after adding 675, 923, and 1623 sawtooth periods (T_M), in which $\overline{U}_{RMS} \cong 3.4\%$, $\bar{\tau}_{ST} \cong 5$ ms, $\bar{q}_1 \cong 2.7 \pm 0.2$ and $\bar{r}_m/a \cong 0.3 \pm 0.05$, as determined from a soft X-ray array. The line over a variable indicates an average over all shots. The continuum fluctuation appears to converge to a sawtooth-like waveform with $|\Delta B/B| \cong 0.5\%$. The relative standard deviation around a 'best fit' sawtooth (see Fig. 4.6) after adding 1623 periods is calculated to be 0.085%, which is consistent with $3.4\%/\sqrt{1623} = 0.083\%$. Fig. 4.7 shows the bin RMS $\tilde{f}_{RMS}(M)$ vs. T_M (the total

number of sawteeth added). For $T_M \gg (3.4/(0.29)(0.5))^2 = 583$, the bin RMS fluctuation approaches $0.29\,|\Delta B/B| = 0.14\%$ as the 'noise' is averaged out.

To study the effects of internal disruptions on edge emission, the continuum filter was replaced by a CIII filter ($\lambda = 4651$Å, 12Å FWHM). For typical Alcator C discharges ($T_{eo} \simeq 1-2$ keV) the CIII emission is localized near the limiter radius and is much brighter than the continuum integrated over the 12Å band pass. Thus the signal in this case is strongly dominated by CIII emission from the plasma edge.

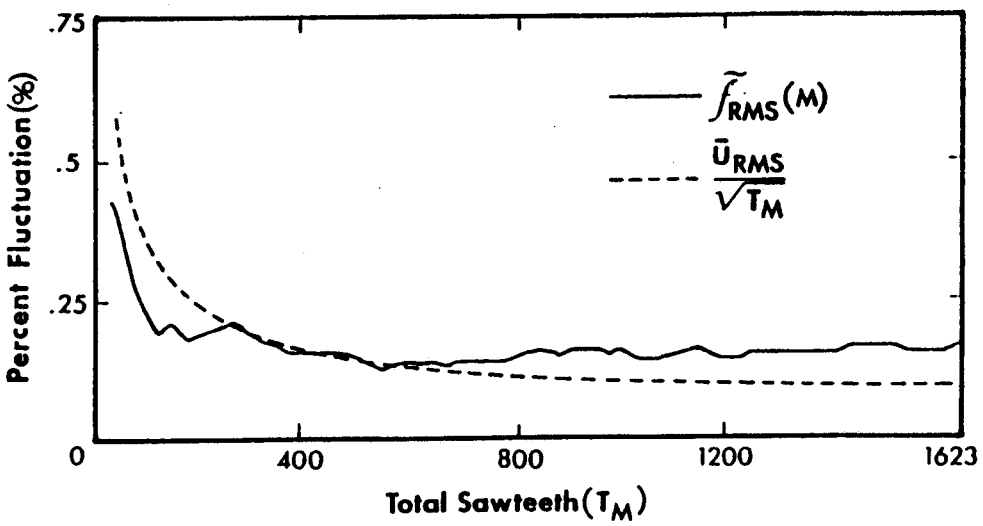

Figure 4.7 — $\tilde{f}_{\rm RMS}(M)$ is plotted vs. $T_{\rm M}$ (total sawteeth after shot M). For $T_{\rm M} \gg 583$, $\tilde{f}_{\rm RMS}(M)$ approaches (.5%)(.29)=.14% while $\bar{U}_{\rm RMS}/\sqrt{T_{\rm M}}$ continues to decrease.

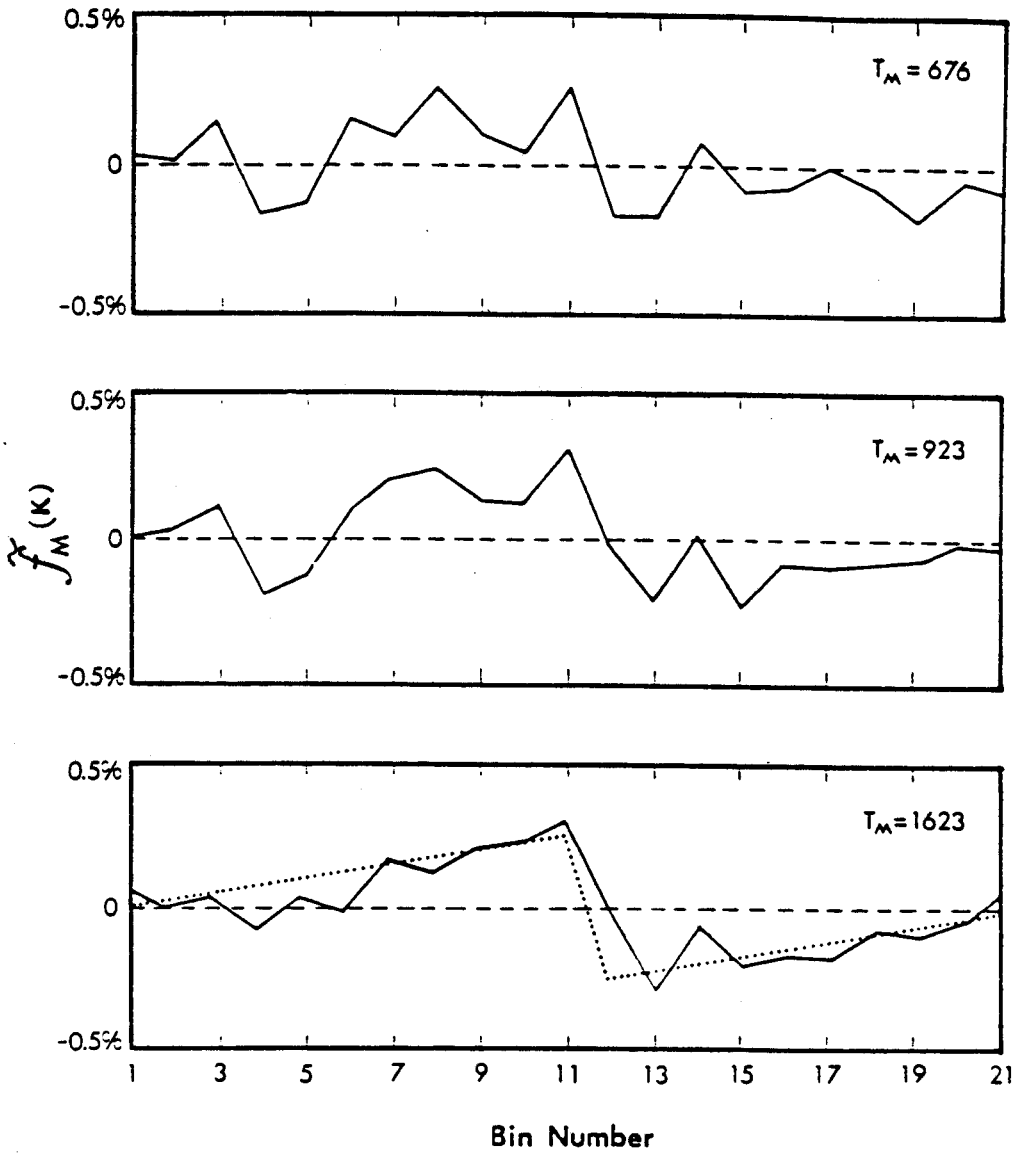

Figure 4.6 – $\tilde{f}_M(K)$ after adding 676, 923, and 1623 sawteeth. For $T_M = 1623$ the RMS fluctuation of $\tilde{f}_M(K)$ around a 'best fit' sawtooth (dotted line) is calculated to be 0.085%. This is consistent with the expected 'noise' level after adding 1623 sawteeth with a 3.4% fluctuation level ($3.4\%/\sqrt{1623} = 0.083\%$), assuming the correlated component $C_j(t)$ is much smaller than the uncorrelated component $U_j(t)$. This 'best fit' sawtooth has an amplitude of $\simeq 0.5\%$ which satisfies the above assumption ($(10.29)(0.5\%) \gg 3.4\%$).

Figure 4.8 shows the relative fluctuation level $\tilde{f}_M(K)$ with the CIII filter after averaging over 1172 sawtooth periods. For these data $\overline{U}_{RMS} \cong$ 3.5% and $\overline{\tau}_{ST} \cong 5$ ms. $|\Delta B/B| < 0.1\%$ which is consistent with the fact that sawteeth are a result of central perturbations ($r < r_m$) in the density and temperature profiles.

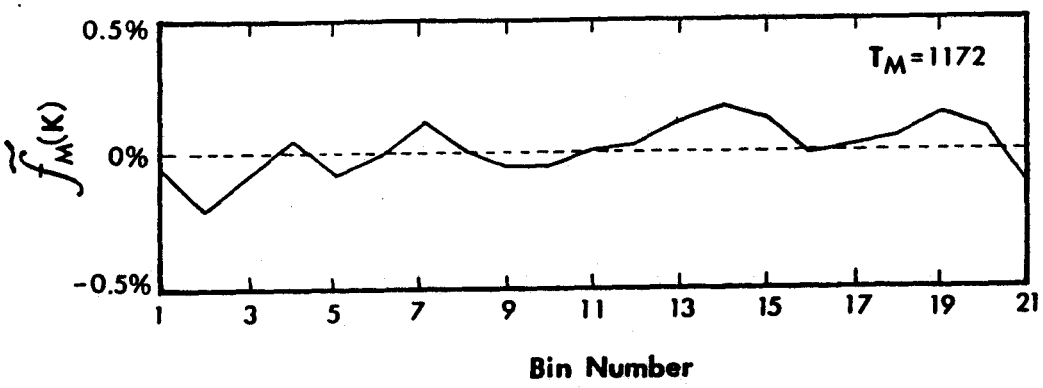

Figure 4.8 — $\tilde{f}_M(K)$ after adding 1172 sawteeth in the case where the usual continuum filter was replaced by a CIII (λ = 4651Å. $\Delta\lambda$ = 12Å) filter. CIII emission is localized near the limiter radius and dominates the signal integrated over this 12Å pass band. No effects of sawteeth are observed.

4.4 Sawtooth Modelling Comparisons

Since 1974, much theoretical and experimental work has been done in modelling the internal disruption[42-45]. For the purposes of this chapter, the density and temperature profiles are modelled just before and just after the internal disruption, allowing the determination of $\Delta B/B$. The initial density and temperature profiles used are $n(r) = n_0(1 - r^2/a^2)^{\alpha}$, $T(r) = T_0(1 - r^2/a^2)^{\gamma}$ where α and γ are independently determined variables. These profiles are then instantaneously flattened out to radius r_m, with total energy and particles conserved (see Fig. 4.9). Figure 4.10 shows a calculation of $\Delta B/B$ for $r_m/a = 0.3$. Also plotted on Fig. 4.10 is the inferred $|\Delta B/B| \cong 0.5\%$ (from Fig. 4.5) in which $\bar{r}_m/a \cong 0.3 \pm 0.05$ and $\bar{\gamma} \cong 1.8$ (calculated from I_p and $q_0 \simeq 0.9$). The inferred value of $\Delta B/B$ is thus consistent with this simple internal disruption model, within the statistical uncertainties of the sampled data and shot to shot variations in density and temperature profiles.

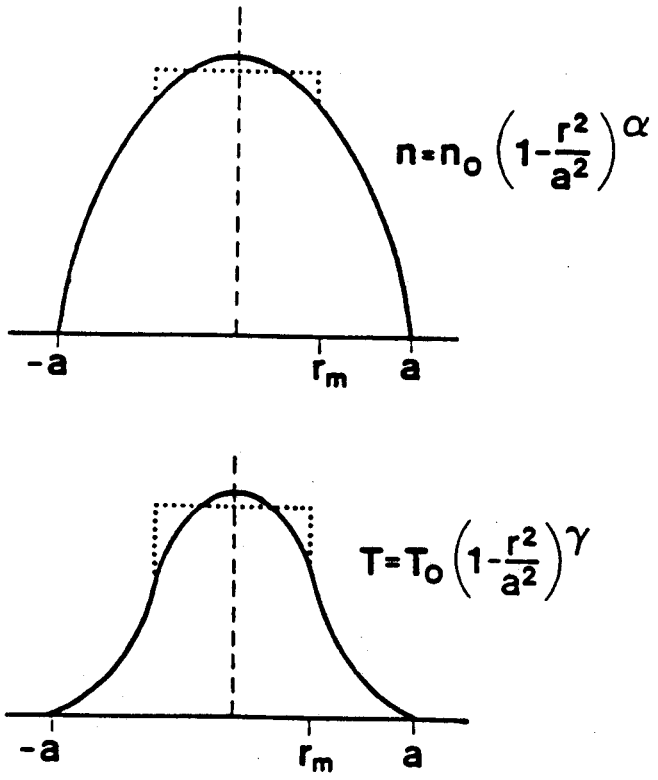

Figure 4.9 — Model of density and temperature profiles before (solid) and after (dotted) an internal disruption. The central temperature and density following the crash are calculated by conserving total particles and energy.

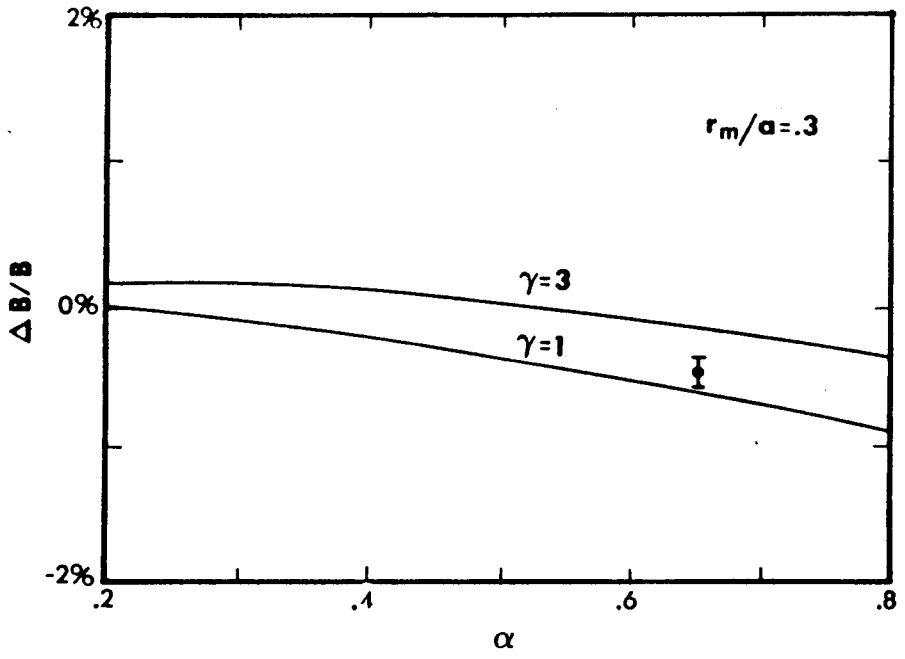

Figure 4.10 — Calculations of the relative change in the central chord continuum brightness $\Delta B/B$ utilizing the simple sawtooth model of Fig. 4.10. $\Delta B/B$ is a function of the initial density and temperature profiles (α, γ) and the relative mixing radius r_m/a, which is 0.3 in this case. Negative values of $\Delta B/B$ imply a sawtooth crash while positive values of $\Delta B/B$ imply an inverted sawtooth. The 'best fit' sawtooth amplitude of Fig. 4.7 ($\Delta B/B \simeq 0.5\% \pm .085\%$) is also plotted for comparison, and is seen to be consistent with the temperature and density profiles of these measurements.

4.5 Summary and Discussion

Sawtooth oscillations have been observed for the first time on the visible continuum central chord brightness in a tokamak plasma. These oscillations result from a central periodic flattening of density and temperature profiles, exhibit a sawtooth-like structure and are in phase with internal disruptions as observed in soft X-ray emission. As the sawtooth instability perturbs primarily the central regions of these moderate q_1, ohmically heated tokamak plasmas, its effect on the visible continuum signal provides further proof that this emission is also coming from the core of the plasma, rather than being due primarily to edge radiation. The fact that the effect is small is a direct consequence of the offsetting density and temperature dependences of the bremsstrahlung at these photon energies. The simple model used for the internal disruption seems sufficient for predicting $\Delta B/B$ for the observed temperature and density profiles.

Chapter 5 presents data taken during pellet fueled discharges[7] , where the density can become highly peaked ($n_e(0)/\overline{n}_e \cong 2$) and $|\Delta B/B| \cong 5\% - 20\%$. In these cases, each sawtooth crash is readily observable on the central chord visible continuum brightness, without the need to average over disruptions. As is shown in Fig. 5.11, predictions from this simple sawtooth model also show good agreement with the measured values of $\Delta B/B$ for these 'giant' sawtooth cases.

CHAPTER 5

Electron Density Profiles During Pellet Fueled Discharges

5.1 Introduction and Motivation

This chapter presents measurements and analysis of electron density profiles obtained from visible continuum measurements, during high density, clean ($Z_{\rm eff} \simeq 1.2$), pellet fueled discharges. Using independently determined measurements of $T_e(r)$, $E_{\rm brem}(r)$, and $Z_{\rm eff}(r)$, $n_e(r)$ can be inferred through

$$n_e(r) = \left\{ \frac{E_{\rm brem}(r) T_e^{1/2}(r)}{Z_{\rm eff}\ (r) \bar{g}_{\rm ff}(T_e(r)) e^{-hc/\lambda T_e(r)}} \right\}^{1/2} . \qquad (5.1)$$

Electron temperature profiles are determined from either Thomson scattering or ECE measurements, or, during sawtoothing discharges, can also be estimated from calculations of j(r). As seen from Eq. 5.1, the sensitivity to uncertainties in $T_e(r)$ is relatively small, due to the relatively weak temperature dependence.

The $Z_{\rm eff}(r)$ profiles for these high density discharges are assumed to be approximately flat. This assumption is consistent with the typically flat $Z_{\rm eff}(r)$ profiles measured in this density regime, during non-pellet discharges. However, allowing for changes in particle transport following pellet injection, impurity profiles and, thus, $Z_{\rm eff}(r)$ profiles might be expected to become more peaked. This question will be addressed in the next section, where it is found that measurements of the

changes in $\overline{Z}_{eff}$ after pellet injection were consistent with no significant peaking in $Z_{eff}(r)$ profiles. The *a priori* assumption that $Z_{eff}(r)$ profiles are flat after injection, is further examined in Sect. 5.3 by comparisons with interferometer and Thomson scattering density measurements.

The major motivation for using continuum measurements as a density diagnostic is the relatively high spatial resolution ($\simeq$ 1 cm.) which is achievable. By analyzing the time evolutions of these profiles, the radial particle transport can be obtained. Injecting pellets is one method of providing the relatively large time-varying profiles which are needed for determining the particle transport.

Energy and particle transport in tokamak plasmas is poorly understood. During pellet fueled, moderate-density ($\overline{n_e} \simeq 2 \times 10^{14}\text{cm}^{-3}$) discharges on Alcator C, χ_i (ion thermal diffusivity) is found to decrease from $\simeq 3\chi_i^{neo}$ to $\simeq \chi_i^{neo}$.[47] This decrease in the anomalous ion transport results in higher global energy confinement times which are consistent with neo-Alcator scaling, $\tau_E \sim \overline{n_e} R^{2.04} a^{1.04}$.

As will be discussed this chapter, in pellet fueled discharges where the pellet injection induces sufficiently large density increases($\Delta\overline{n}_e/\overline{n}_e \geq 0.9$), electron density profiles are observed to remain peaked after the density has decayed to a constant level[65]. ($\Delta\overline{n}_e/\overline{n}_e$ is the relative increase in the line-average density just after the pellet injection.) This effect of density profile peaking is correlated with changes in the ion thermal transport[41], since for discharges with the most peaked density profiles following pellet injection, χ_i is usually closest to χ_i^{neo}. Recent results from TFTR[67] also indicate more peaked density profiles after

pellet injections. Analysis of these peaked profiles is presented in Chapter 6, where changes in diffusion and convection fluxes after pellet injections will be determined.

5.2 Effects of Frozen H_2 Pellet Injections on $\overline{Z}_{eff}$

$\overline{Z}_{eff}$ (as defined in Eq. 3.5) is monitored during frozen H_2 pellet fueled discharges, in order to determine the effects of pellet injections on impurity transport. There is evidence that impurity transport changes after pellet injections. Impurity transport during pellet fueled discharges is studied by the injection of a small amount of vanadium just after the pellet injection.[32] In certain discharges, the V^{+20} decay time is seen to increase significantly.[32] Analysis of soft x-ray emissions further indicates that carbon, the most prevalent background impurity, may peak in certain discharges following pellet injection[33]. Thus, in order to justify using continuum measurements to infer density profiles, it is important to determine to what extent these changes in impurity transport effect Z_{eff} .

The volume-averaged Z_{eff} clearly must decrease just after pellet injection. However, if the impurity profiles become highly peaked due to changes in impurity transport, the line-average $\overline{Z}_{eff}$ may actually increase. Shown in Fig. 5.1 are traces of $\overline{Z}_{eff}(t)$ and Mo^{+30} brightness (maximum emission near plasma center) during two pellet fueled discharges. In one discharge, the Mo^{+30} brightness is seen to increase substantially after the density increase due to the pellet has decayed. In the other discharge shown, the Mo^{+30} brightness also increases after the injection but then returns to a pre-pellet value after a 'giant'

sawtooth. 'Giant' sawteeth are discussed in detail in Sec. 5.5, and are found to return both the impurity and background transport to pre-pellet conditions. Fig 5.2 shows the typical effects of a giant sawtooth on other plasma parameters.

As shown in Fig. 5.1, no significant difference in $\overline{Z}_{\rm eff}(t)$ between the two cases can be observed. Just after injection, $\overline{Z}_{\rm eff}(t)$ drops to a value close to unity, and then returns approximately to the pre-pellet value after the density increase due to the pellet has decayed. This is roughly consistent with a simple dilution model, where the impurity profiles following pellet injection are unchanged, and where the ratios of impurity to background densities decrease, due to the increased background density.

In order, quantitatively, to determine the possible effects of impurity peaking on $\overline{Z}_{\rm eff}$ measurements, a two-impurity model was constructed. The plasma initially is assumed to be comprised of two different types of impurities; one which centrally peaks following pellet injection (referred to as "peaking impurity"), and one whose profile remains flat after injection (termed "non-peaking impurity"). Initially both the peaking and non-peaking impurity profiles are assumed to be similar to the background electron density profile $\sim (1-(r/a)^2)^{1/2}$, such that $Z_{\rm eff}(r)$ is flat. A parameter χ is now defined to be the fraction of $\overline{Z}_{\rm eff} - 1$ (not fraction of impurities), before pellet injection, which is due to the non-peaking impurities. Thus, initially $\overline{Z}_{\rm eff} = 1 + \Delta\overline{Z}\chi + \Delta\overline{Z}(1-\chi)$, where $\Delta\overline{Z} \equiv \overline{Z}_{\rm eff} - 1$.

After pellet injection, the peaking impurity is assumed to change from the background electron density profile $n_{\rm imp} \sim (1-(r/a)^2)^{1/2}$ to a more highly peaked profile $n_{\rm imp} \sim (1-(r/a)^2)^{\delta'}$, while conserving

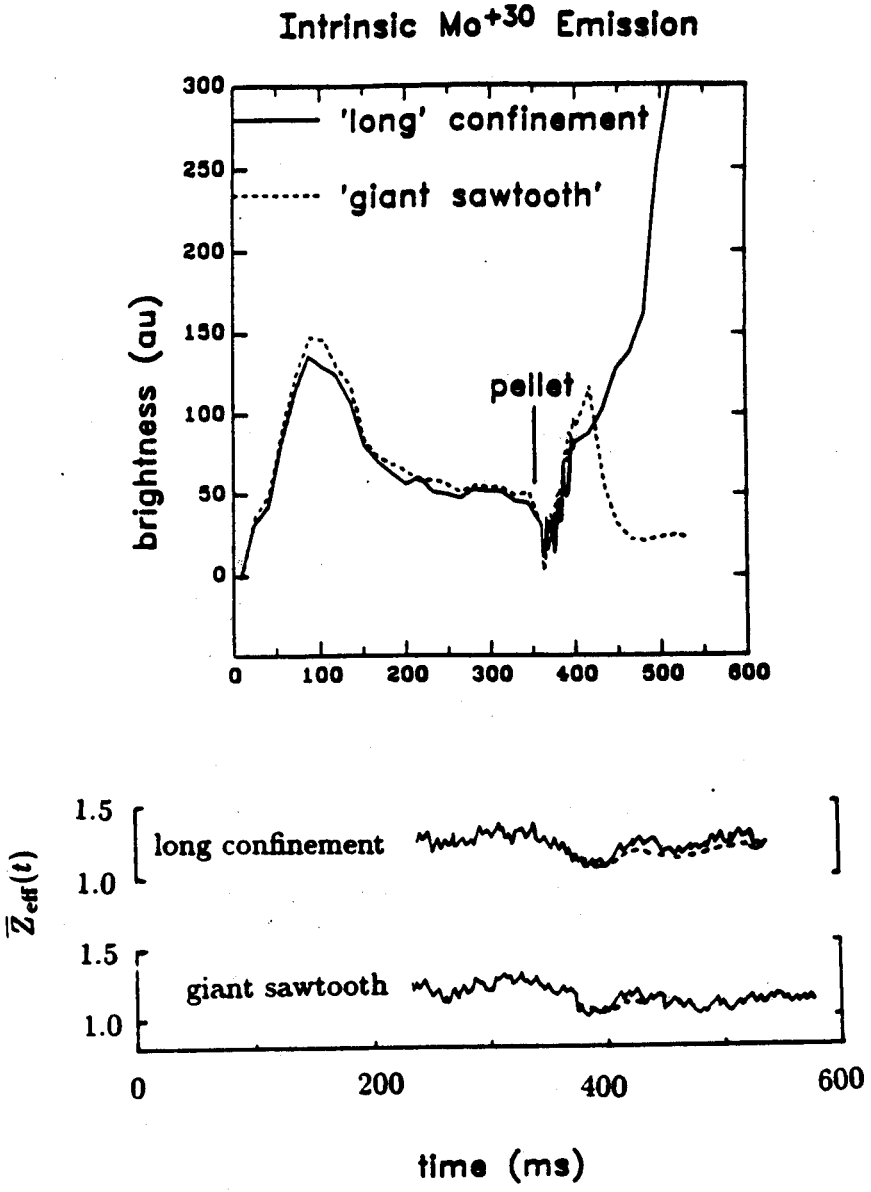

Figure 5.1 — $\bar{Z}_{eff}(t)$ and $Mo^{+30}(t)$ during pellet injected discharges. In one discharge, the Mo^{+30} brightness increases substantially long after injection, while in the other Mo^{+30} brightness returns approximately to a pre-pellet value after the giant sawtooth. The dashed traces of $\bar{Z}_{eff}(t)$ after injection are corrected for changes in density profiles after injection. Little or no change in $\bar{Z}_{eff}$ is seen after the giant sawtooth. The $\bar{Z}_{eff}(t)$ time scale is shifted $\sim +20$ ms with respect to the Mo^{+30} trace.

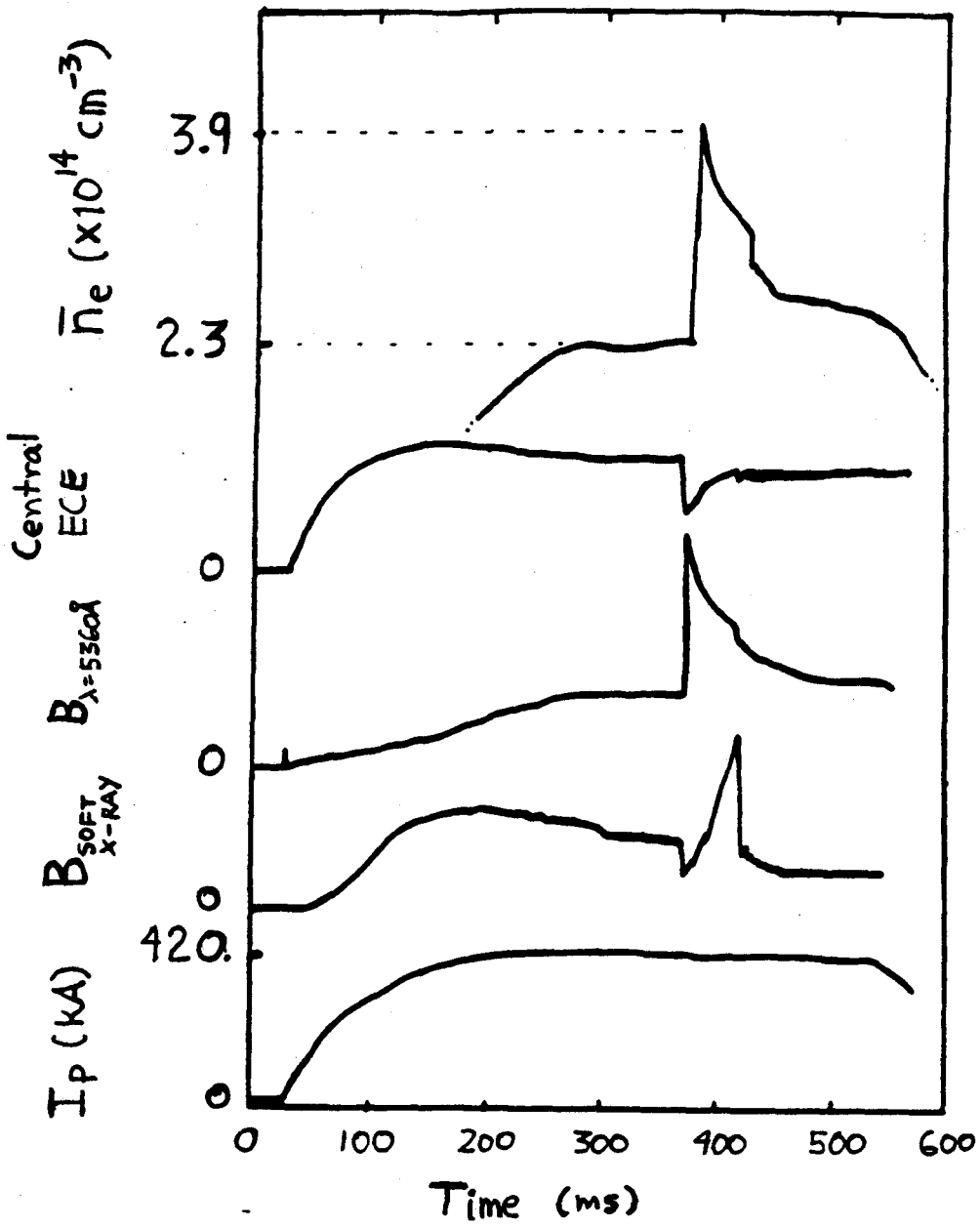

Figure 5.2 — Plasma parameters during a pellet fueled discharge. Traces shown are central-chord line-average density (from interferometer), central ECE emission, central-chord visible continuum brightness, central-chord soft X-ray brightness and plasma current. 'Giant' sawtooth occurs at ~ 410 ms.

impurity ions. The non-peaking impurity profile is assumed to be unchanged.

Results of this modelling are summarized in Figs. 5.3 and 5.4, where primed variables indicate having been evaluated after pellet injection. For pre-pellet values of $\overline{Z}_{\rm eff}$ equal to $1.2 \pm .1$, the post-pellet values of the $\overline{Z}'_{\rm eff}$ and central $Z'_{\rm eff}(0)$ are calculated as a function of the initial fraction of non-peaking impurities χ. The post-pellet peaking-impurity profile is assumed to be of the form $n_{\rm imp} \sim (1-(r/a)^2)^{30}$, since soft X-ray analysis has yielded similar profiles[33]. The ratio of post-pellet to pre-pellet central electron densities, $\overline{n}_e'/\overline{n}_e$, is assumed to be 1.5, since this is the density ratio for the data used in this comparison.

As defined in Eq 3.5, $\overline{Z}_{\rm eff}$ is the line-integral of $Z_{\rm eff}$, weighted approximately by $n_e^2/T_e^{1/2}$. Before pellet injection, this weighting function is approximately constant in radius, so that $\overline{Z}_{\rm eff}$ is the unweighted line-average of $Z_{\rm eff}(r)$. After pellet injection, when the electron density profile often become more peaked, $\overline{Z}'_{\rm eff}$ is weighted more towards the center. Since the impurities are assumed to accumulated in the center, it is therefore important to include the effects of more peaked background density profiles. Figure 5.3 shows the effects of varying the final electron density profiles on calculations of χ. The final electron density profile is approximated by $n'_e \sim (1-r^2/a^2)^{\alpha'}$, with where α' is varied between .5 and 2.

As an example, assume $\overline{Z}_{\rm eff}$ is measured to be 1.2 (before injection) and that after the pellet density has decayed such that $\overline{n}_e'/\overline{n}_e=$ 1.5, $\overline{Z}'_{\rm eff}$ has increased to 1.3 The intersections of the 3 curves in Fig. 5.3 associated with $\overline{Z}_{\rm eff} = 1.2$ with $\overline{Z}'_{\rm eff} - 1 = .3$ yields three values for

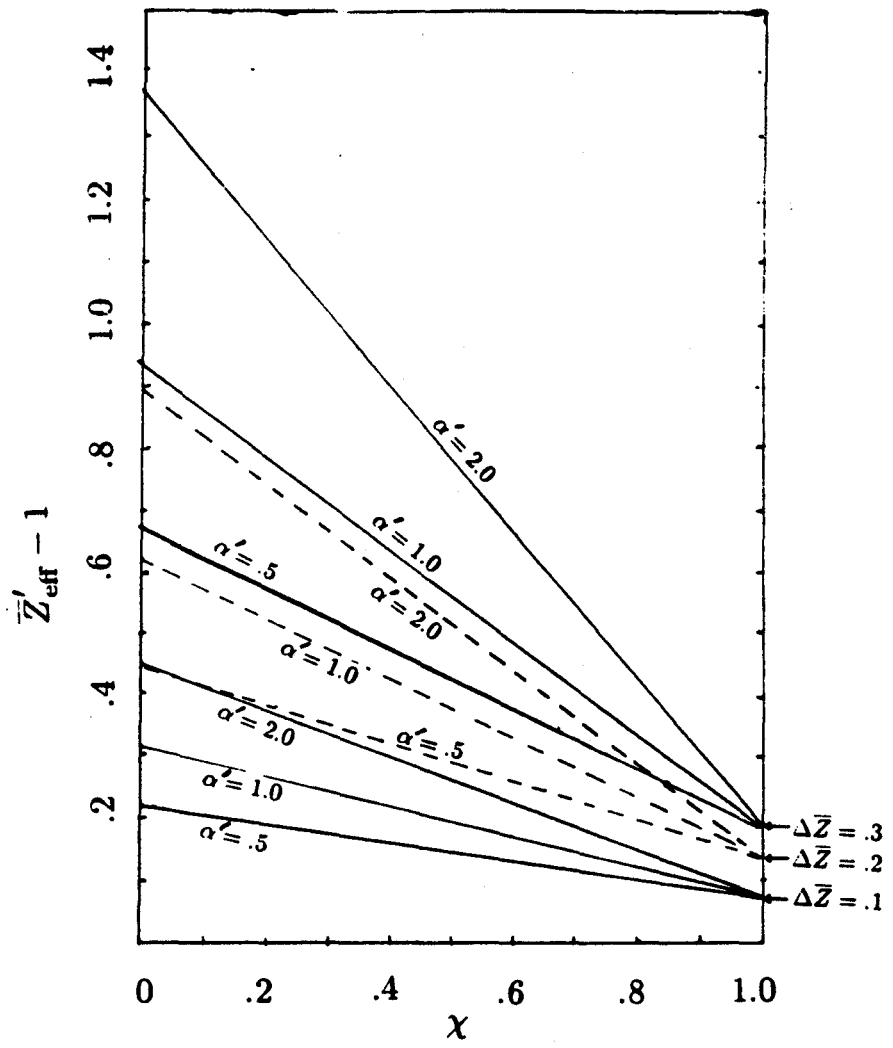

Figure 5.3 — Results from a two-impurity model, showing final $\overline{Z}'_{\text{eff}}$, versus the non-peaking fraction of impurities χ. $\Delta\overline{Z} \equiv \overline{Z}_{\text{eff}} - 1$, where $\overline{Z}_{\text{eff}}$ is the initial weighted line-average Z_{eff}, given in Eq. 3.5. For this simulation, $\overline{n}_e'/\overline{n}_e = 1.5$ and the peaking fraction of impurities are assumed to have final profiles of $n_{\text{imp}} \sim (1 - r^2/a^2)^{30}$. α' is the post-pellet density parabolic power. $n'_e \sim (1 - r^2/a^2)^{\alpha'}$.

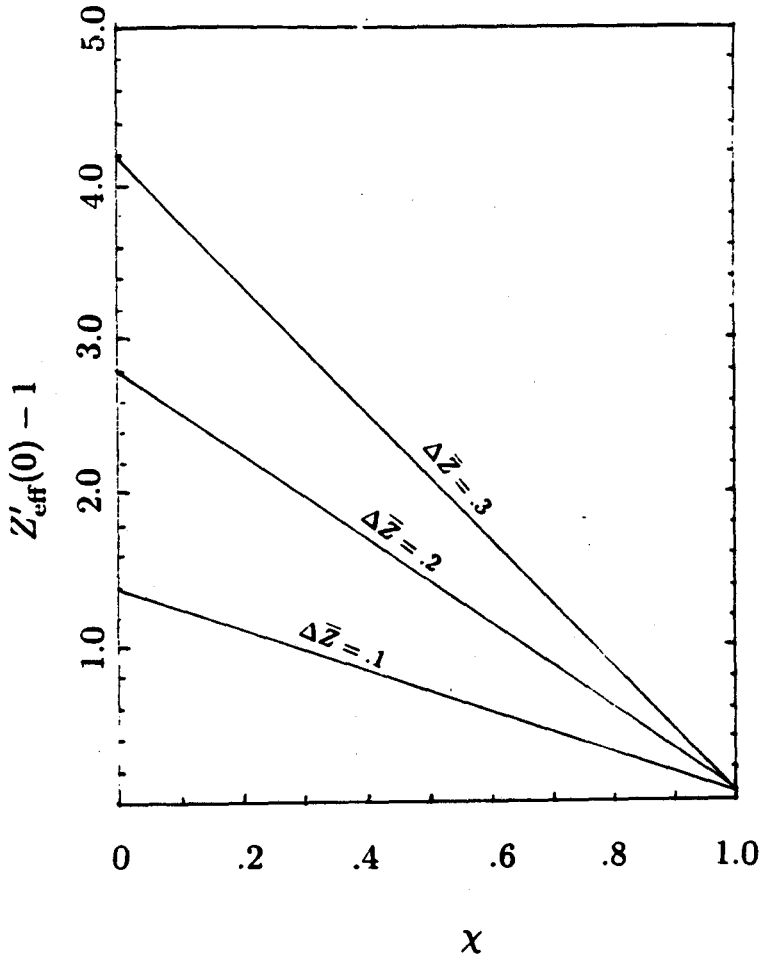

Figure 5.4 — Results from a two-impurity model, showing final $Z'_{eff}(0)$, versus the non-peaking fraction of impurities χ. $\Delta\overline{Z} \equiv \overline{Z}_{eff}$ - 1. For this simulation, $\overline{n}_e'/\overline{n}_e = 1.5$ and the peaking fraction of impurities are assumed to have final profiles of $n_{imp} \sim (1 - r^2/a^2)^{30}$.

χ- .46, .66, and .78, depending on the final electron density peakedness. From Fig 5.4, again using $\overline{Z}_{eff} = 1.2$ and these three values for χ, the final central values for $Z'_{eff}(0)$ are 2.5, 2.0, and 1.7 respectively. Although $\overline{Z}_{eff}$ typically decreases after pellet injection, this example illustrates how sensitive the inferred value of $Z'_{eff}(0)$ is to differences in the background density profiles.

As shown in Fig 5.2, $\overline{Z}_{eff}$ is seen to decrease slightly after pellet injection, from approximately 1.2 to 1.1. Assuming $\overline{Z}_{eff} - \overline{Z}'_{eff} \simeq -0.07 \pm .05$, from Figs. 5.3 and 5.4, $Z'_{eff}(0) = 1.13^{+.28}_{-.00}$, $\chi = 1.0^{-.13}_{+.00}$ if one assumes a post-pellet electron peaking of $n'_e = n'_{eo}(1-(r/a)^2)$, or $Z'_{eff}(0) = 1.13^{-.07}_{-.00}$, $\chi = 1.0^{-.08}_{+.00}$ assuming $n'_e = n'_{eo}(1-(r/a)^2)^2$. $Z'_{eff}(0)$ is 1.13 for both cases, indicating the measurements are consistent with pure dilution and no impurity peaking ($\chi = 1$). However, the uncertainties in $\overline{Z}_{eff} - \overline{Z}'_{eff}$ are large enough that $Z'_{eff}(0)$ on axis may be as large as 1.41 ($\chi = .87$) in the case where the post-pellet electron density profile is only slightly more peaked ($n'_e = n'_{eo}(1-(r/a)^2)$). The peakedness of n_e profiles following pellet injection, as determined from Abel inversions of the 5-chord interferometer data, are usually between these two cases, e.g. $n'_e = n'_{eo}(1-(r/a)^2)^{\alpha'}, 1.0 \leq \alpha' \leq 2.0$.

It should also be noted that if one assumed that all impurities which are initially present in the plasma before the pellet injection accumulate after the injection (equivalent to the case $\chi = 0$), $\overline{Z}_{eff}$ would increase from 1.2 to between 1.45 ($\alpha' = 0.5$) and 1.9($\alpha' = 2.0$), which is clearly outside the range of uncertainty these measurements of $\overline{Z}'_{eff}$.

These results are sensitive to the assumed profile shape of the peaking impurity. Assuming a more peaked impurity profile, a higher post-pellet $Z'_{eff}(0)$ will generally be inferred. $Z'_{eff}(0) - 1$ is found to be

approximately proportional to $\sqrt{\delta'}$, where δ' is the parabolic power of the peaked impurity. The effects of not conserving the total number of peaking impurities ions or changing the average charge state of the impurity (eg. due to plasma cooling) is found to only change the inferred value of χ and not $Z'_{eff}(0)$.

5.3 Qualitative Effects on Density Profiles

Electron density profiles, inferred from visible continuum measurements, have been monitored during H_2 pellet fueled discharges over the ranges: 200 kA $\leq I_p \leq$ 500 kA, 8 T $\leq B_t \leq$ 10 T, with relative pellet increases $0 < \Delta\overline{n}_e/\overline{n}_e \leq 2$, and background gases H_2 and D_2. As shown in Fig. 5.2, just after pellet injection, the central electron temperature drops approximately adiabatically, resulting in an initial drop in the central-chord soft X-ray brightness and central ECE emission. The central electron temperature then reheats slightly faster than the density decay rate. Thomson scattering and ECE profile measurements indicate that electron temperature profiles generally relax to the pre-pellet profile shapes on a very fast time scale ($\sim$ 1 ms). Thus, in cases where these measurements are not available, temperature profile shapes are obtained using pre-pellet profiles (estimated from j(r) calculations assuming $q_0 \simeq .9$), and using central values proportional to central ECE emission measurements.

For relatively large pellet induced density increases $\Delta\overline{n}_e/\overline{n}_e \geq 0.9$, density profiles typically remain more peaked following pellet injection.

Figure 5.5 shows the time evolution of continuum-inferred density profiles during a pellet fueled discharge where $\Delta\overline{n}_e/\overline{n}_e = 1.6$. The peak-to-average (P/A) increases quickly after the injection and remains peaked after the density has decayed to constant level. This clearly indicates a change in particle transport.

Changes in impurity transport are well correlated with changes observed in the background plasma after pellet injection. A trace amount of vanadium was injected into the plasma just after the pellet injection, and differences in the vanadium decay rates with varying pellet induced density increases ($\Delta\overline{n}_e/\overline{n}_e$) were observed. For discharges in which the density profiles were more peaked after pellet injection, the vanadium decay time was found to increase. Fig. 5.6 shows a comparison in the decay rates of V^{+20}, for both a 'small' ($\Delta\overline{n}_e/\overline{n}_e$=0.5) and 'large' ($\Delta\overline{n}_e/\overline{n}_e$= 1.2) pellet increase.[32] The slower decay rate for the 'large' pellet cases is attributed to an increase in confinement time of vanadium, although slower electron density decay rates, found for 'large' pellet injections, may also be partially responsible[49].

Shown in Fig. 5.7 are typical comparisons of the continuum inferred density profiles with density measurements obtained from Thomson scattering ($n_e(r = 0)$) and interferometer data. The Thomson scattering data were normalized to the central density inferred from continuum measurements before the pellet injection. Since these comparisons show good agreement, before and after giant sawtooth, this indicates that the Z_{eff} profile is indeed flat for these discharge, or at least flat to within the uncertainties of Thomson and Abel-inverted interferometer data. However, while this result doesn't preclude the possibility that a small amount of impurities accumulate on axis after pellet injection,

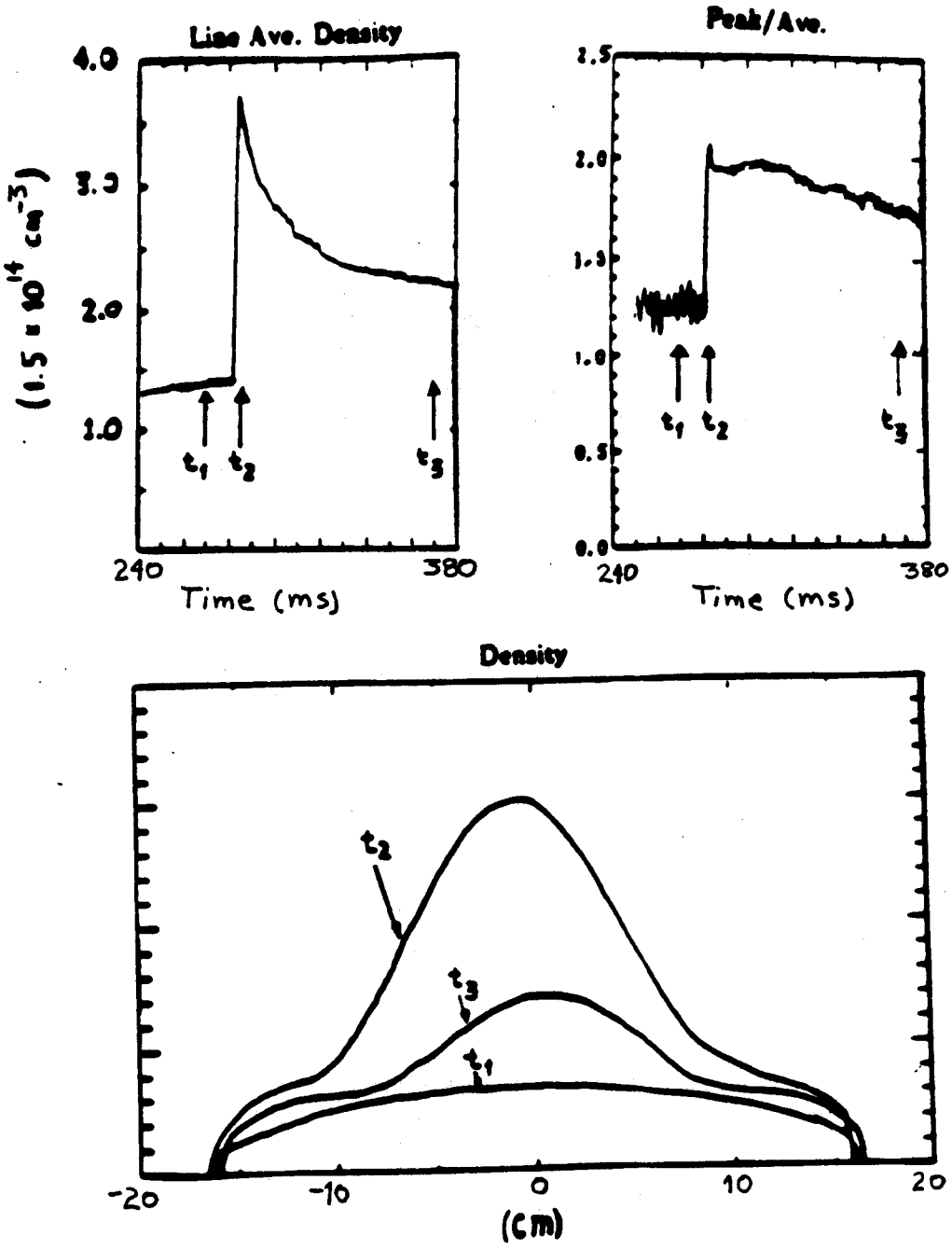

Figure 5.5 — Density profiles obtained from continuum brightness measurements during a pellet fueled discharge. Profiles become more peaked after the pellet injection, and remain peaked after the density has decayed to a steady-state level.

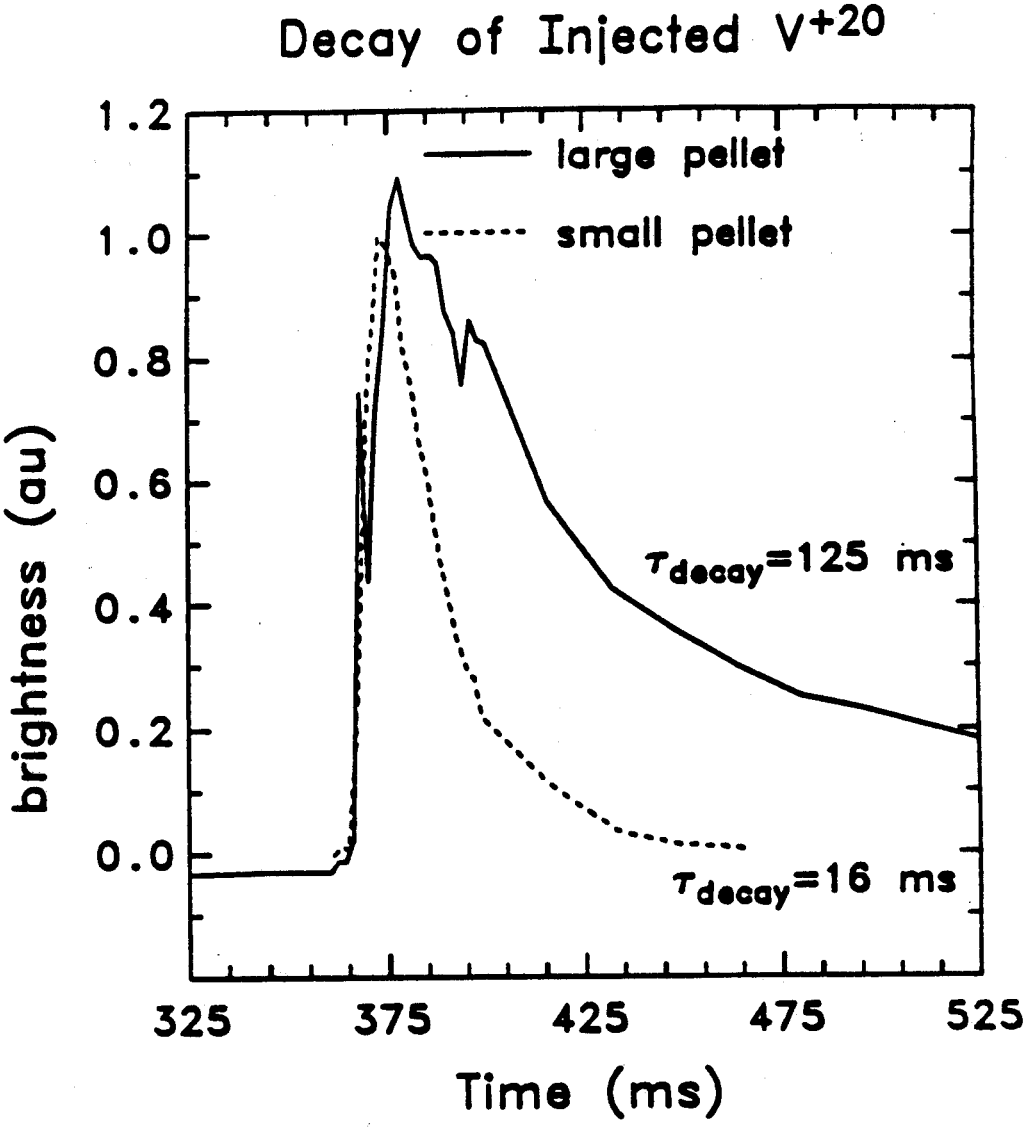

Figure 5.6 — V^{+20} brightness after a pellet injection. Traces show differences between 'large' and 'small' pellet cases. From Ref. [32].

this does indicate that the effects on the $Z_{eff}(r)$ profile are probably quite small.

The effects of injecting smaller pellets, $\Delta\overline{n}_e/\overline{n}_e \leq .5$, on the background density profiles are found to be qualitatively quite different. Figure 5.5 shows the density profiles during a pellet fueled discharge where $\Delta\overline{n}_e/\overline{n}_e \simeq 0.5$. Again, comparisons with Thomson and interferometer data usually are in good agreement for these cases. Due to the initial central perturbation of the pellet, the profiles peak slightly during the pellet decay period, but return to pre-pellet density profile shapes (P/A = 1.3) after the pellet density has decayed to a constant level.

Photographic exposures were taken of the injected pellets in order to monitor their ablation and trajectory through the plasma. It was found that pellets which induced smaller density rises $\Delta\overline{n}_e/\overline{n}_e$(which were previously shown not to induce a noticeable change in particle transport), didn't penetrate as far into the plasma. Since the background densities were similar, it is inferred that these smaller density increases were due to smaller pellets which deposited fewer particles into the plasma, further away from the plasma central axis. (Variations in pellet sizes are due to small variations in pellet injector conditions as the pellet is being formed in the barrel[50].) It is not clear from this data, however, whether the particle transport changes are due to the large density perturbations or due to increased pellet penetration distance.

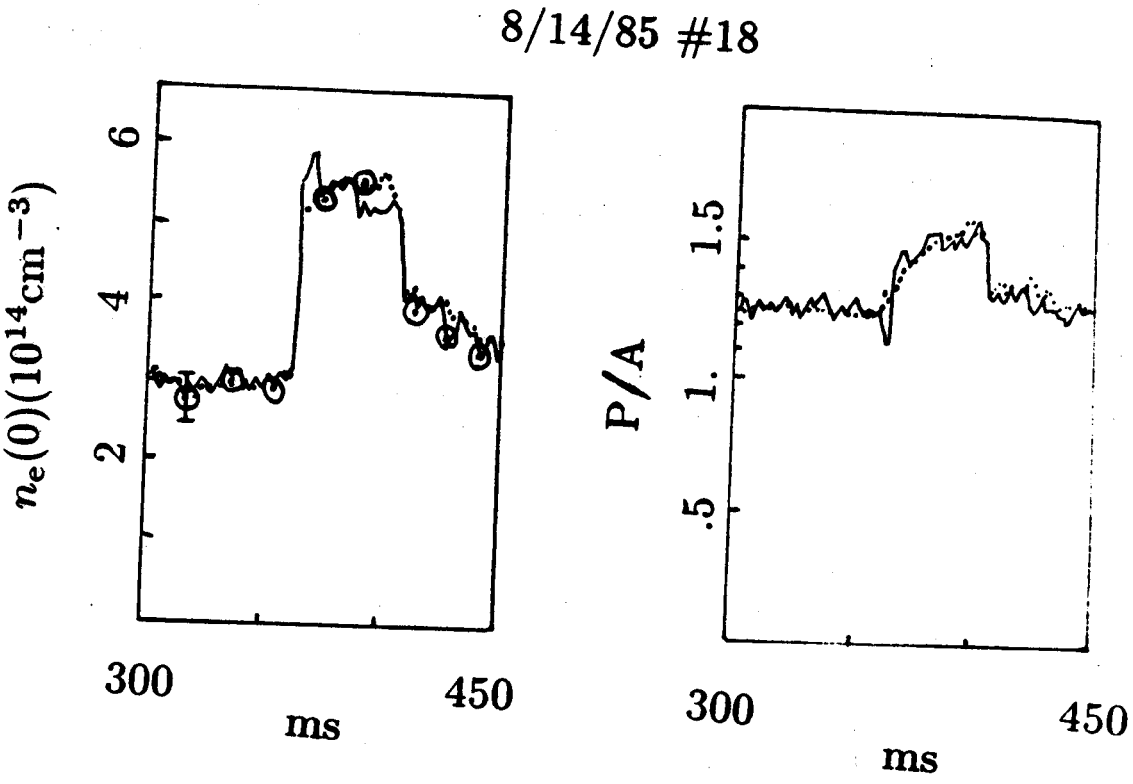

Figure 5.7 — Comparisons between continuum inferred values of the central and peak-to-average (P/A) densities with measurements from Thomson scattering and Abel-inverted interferometer data. Effect of a 'giant' sawtooth is seen at ~ 405 ms. Solid lines are continuum data, dotted lines are from Abel-inversions of interferometer data, and open circles are Thomson scattering data.

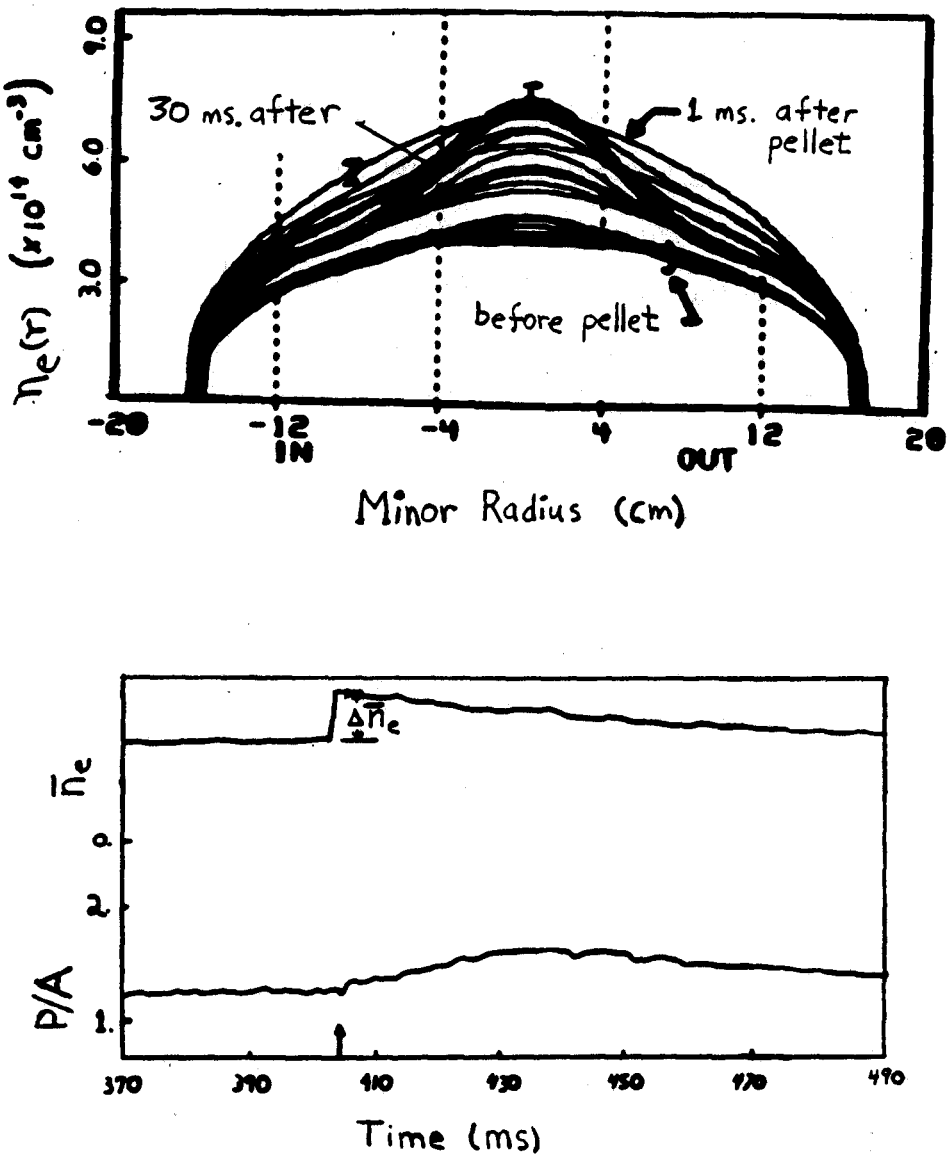

Figure 5.8 — Time evolution of the density profile during a 'small' pellet fueled discharge. No significant change in the final peak-to-average (P/A) is observed after the pellet density has decayed to a steady-state level.

5.4 Thresholds for Transport Changes

For discharges in which pellet fueling increases the density sufficiently, density profiles become more peaked after injection. Shown in Fig. 5.9 is the increase in the P/A, (determined from the difference in the P/A measured just before injection and that measured after the density has decayed to a new, constant level), vs. $\Delta\overline{n}_e/\overline{n}_e$. The final P/A value is, therefore, sensitive only to particle transport at that time, and not to the initial effects of the pellet perturbation. For discharges with giant sawteeth, the final P/A is measured just before the giant sawtooth crash which is usually 20–30 ms. after the pellet injection.

For discharges in which H_2 pellets were injected into D_2 background plasmas, and $\Delta\overline{n}_e/\overline{n}_e \geq 0.7$, the density profiles remain more peaked after the pellet density has decayed to a constant level (Fig. 5.6). For discharges with similar background densities but where $\Delta\overline{n}_e/\overline{n}_e \leq 0.7$, the density profiles returned to pre-pellet profiles after the decay. For discharges where H_2 pellets were injected into H_2 plasmas, the $\Delta\overline{n}_e/\overline{n}_e$ threshold is found to be slightly higher ~ 0.9 (see Fig. 5.10). Again, no steady-state peaking is observed for $\Delta\overline{n}_e/\overline{n}_e \leq 0.9$

Impurity transport is also well correlated with this apparent threshold for changes in background particle transport. Figure 5.11 shows changes in V^{+20} decay rates with increases in pellet density $\Delta\overline{n}_e/\overline{n}_e$, for discharges with H_2 pellets injected into D_2 plasmas.[32] For sufficiently large $\Delta\overline{n}_e/\overline{n}_e \geq 0.8$, a substantial increase in the decay time is observed. This is comparable to the changes in the background particle transport for pellet injections with $\Delta\overline{n}_e/\overline{n}_e \geq .7$ shown in Fig. 5.6.

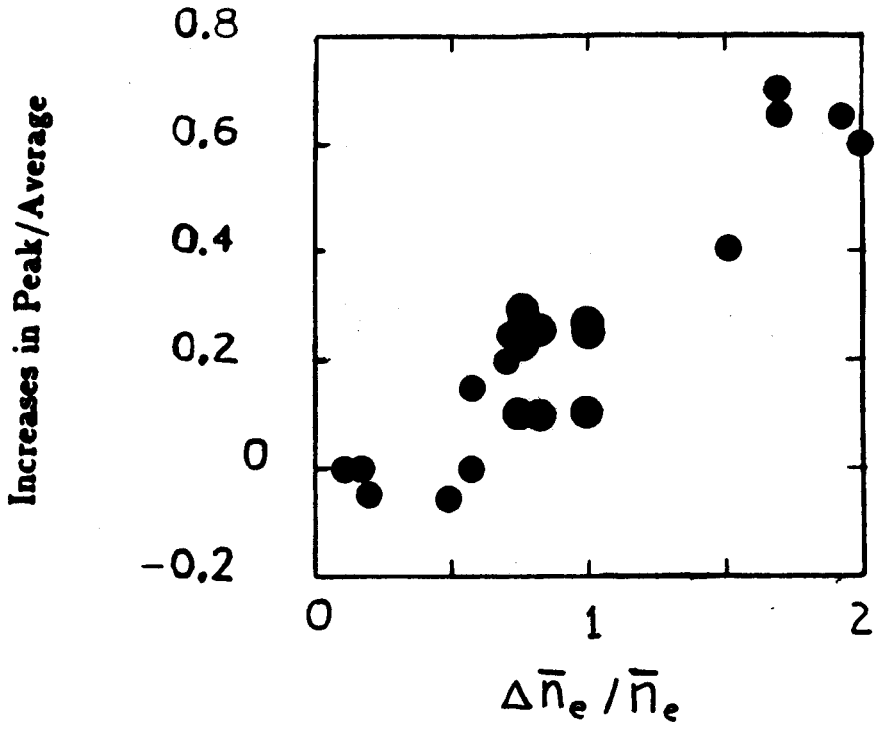

Figure 5.9 — Peak-to-average increases, measured after the pellet density has decayed to a steady-state level. For discharges with giant sawteeth, the P/A is measured just prior the giant sawtooth crash. Pellets are H_2, background gas is D_2.

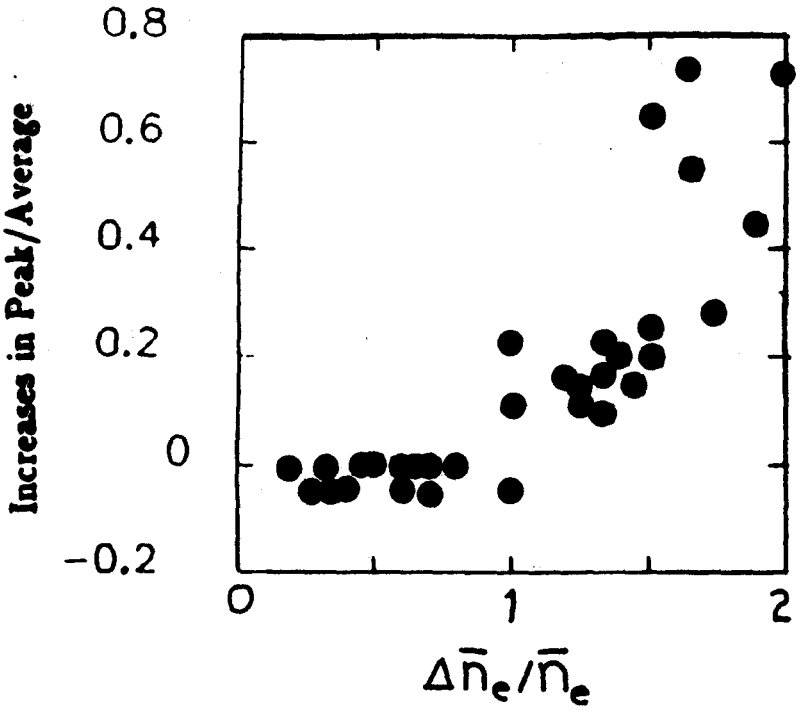

Figure 5.10 — Peak-to-average increases, measured after the pellet density has decayed to a steady-state level. For discharges with giant sawteeth, the P/A is measured just prior the giant sawtooth crash. Pellets are H_2, background gas is H_2.

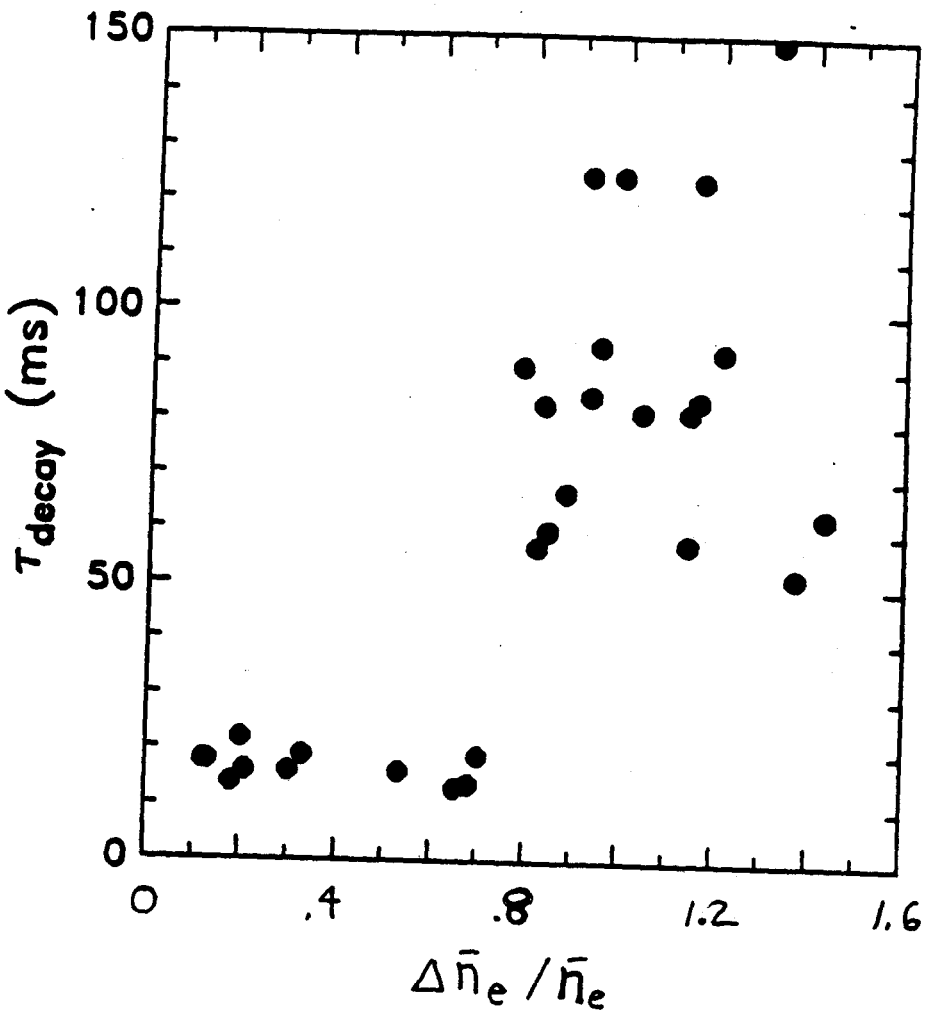

Figure 5.11 — V^{+20} brightness decay rate vs. the relative increase in the line-average density due to pellet injection ($\Delta\bar{n}_e/\bar{n}_e$) for H_2 pellets injected into D_2 background plasmas.[32]

Low current ($q_l \geq 6.5$) discharges are qualitatively different, in that no steady-state peaking is observed, even for the largest pellet induced density increases of $\Delta\overline{n}_e/\overline{n}_e \simeq 2$ (see Fig 5.12). Similarly, vanadium confinement time is also seen to decrease for these low current discharges.[51] Thus, it appears that both large ($\Delta\overline{n}_e/\overline{n}_e \geq .7 - .9$) density increases and, low to moderate values of q_l are necessary to change the particle transport after pellet injection.

5.5 Effects of Giant Sawteeth

In discharges with very peaked density profiles following pellet injection, a sawtooth instability, (which flattens temperature and density profiles inside some mixing radius $r_m \leq 0.5$), may result in a large change ($\simeq$ 10 %) in the central-chord continuum brightness. This is termed a giant sawtooth since, for typical temperature and density profiles of non-pellet discharges, the relative changes in the central-chord continuum brightness due to sawteeth are small ($\simeq 0.5$ %), as presented in Chapter 4.

As shown in Fig 5.2, other diagnostics, such as the soft X-ray brightness, central ECE emission, and central-chord interferometer also detect giant sawteeth. The relative decrease in central ECE emission (proportional to T_{eo}) due to the giant sawtooth is not very different than that which is typically measured during normal sawteeth ($\simeq$ 5%–10%). This is due to the fact that the temperature profiles, unlike the density profiles, are not more peaked just before the giant sawtooth. Giant sawteeth are also observed on the central-chord interferometer

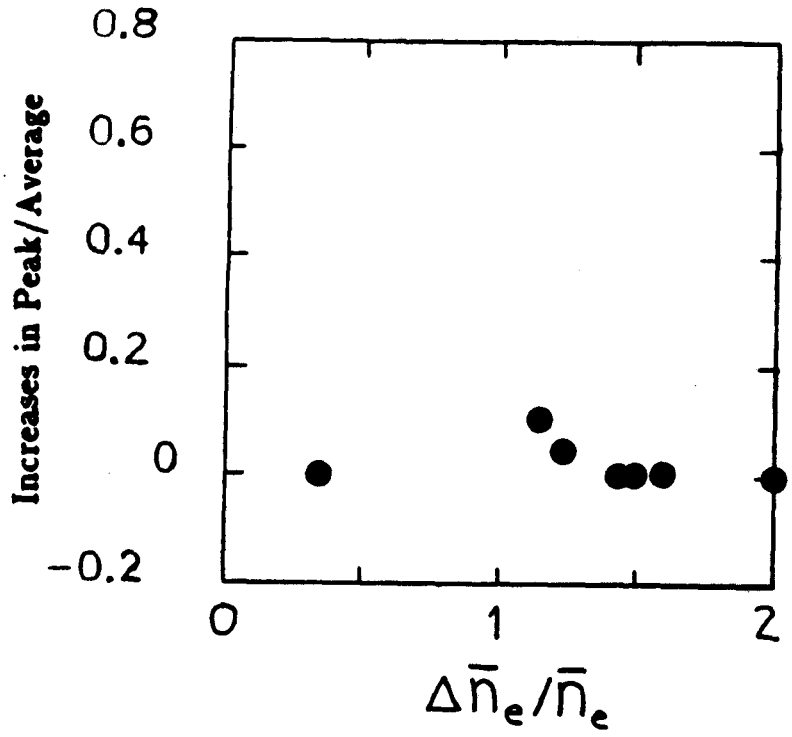

Figure 5.12 — Peak-to-average increases, measured after the density has decayed to a steady-state level. For these data, $q_l \geq 6.5$. Pellets are H_2, background gas is D_2.

measurement ($\Delta\bar{n}_e/\bar{n}_e \simeq 5\%$), indicating a more peaked pre-giant sawtooth density profile.

Within a few milliseconds after the giant sawtooth crash, the density profiles usually return to flatter, pre-pellet profiles. This is shown in Fig. 5.7, where the P/A after the giant sawtooth decreases abruptly from ~ 1.5 to ~ 1.3. After a giant sawtooth, the impurity transport is also observed to return to pre-pellet conditions. As shown in Fig. 5.1, the Mo^{+30} brightness is seen to return approximately to a pre-pellet level. During discharges where trace amounts of vanadium were injected after the pellet injection, the decay time of V^{+20} is much larger before a giant sawtooth than after the giant sawtooth.[32]

Shown in Fig. 5.13 are the changes in the continuum brightness profile due to a giant sawtooth. The central-chord brightness is seen to decrease by $\sim 10\%$, and the continuum brightness inversion radius is approximately 3.0 cm. ± 0.5 which is consistent within the uncertainties with that obtained from the soft-Xray brightness profile (~ 3.5 cm.) shown in Fig 5.15.

Using the simple sawtooth model of Fig 4.9, the central temperature and central-chord line-average density measurements, and assuming a mixing radius of r_m, the central-chord continuum brightness is calculated and compared to the measured brightness during giant sawteeth. Shown in Fig 5.14 is a comparison between the measured and calculated relative changes in the central-chord continuum brightness $\Delta B/B$. These comparisons show good agreement over a wide range of $\Delta B/B$. While not verifying the details of the sawtooth model shown in Fig 4.9, this agreement provides further evidence that the effects of

the giant sawtooth on the continuum brightness are mostly due to the more peaked density profiles after pellet injection.

Smaller sawteeth are usually observed on the soft X-ray brightnesses before a giant sawtooth occurs. However, these smaller sawteeth do not have the effect of changing the density profiles or impurity transport as with giant sawteeth, nor are they observable on the central-chord continuum brightness and the central-chord interferometer. As shown in Fig. 5.15, measurements from a soft X-ray array indicate that that the inversion radii of the sawteeth initially decrease just after injection and then increase until the the giant sawtooth occurs. Thus, it is likely that the mixing radius is smaller just after pellet injection, which would explain why these smaller sawteeth are not observed on the central-chord continuum brightness and interferometer.

Therefore, it appears that although sawteeth are necessary for returning the plasma to pre-pellet conditions, it is only when the sawtooth perturbation is large enough to flatten sufficiently the inner portion of the plasma, that the particle transport returns to pre-pellet conditions.

Recently, sawtooth oscillations inconsistent with the Kadomtsov model have been observed on other tokamaks[54,68]. Recent results at JET report 'compound' sawteeth which consist of alternating 'full' and 'partial' sawtooth oscillations, neither exhibiting precursor oscillations. The 'full' sawteeth are similar to standard sawteeth in that they result in a flattening of the density and temperature inside a central mixing radius. The 'partial' sawteeth, however, were found to be due to flattening of these profiles in an annular region, located outside the mixing region of the 'full' sawtooth. The giant sawteeth observed on Alcator C

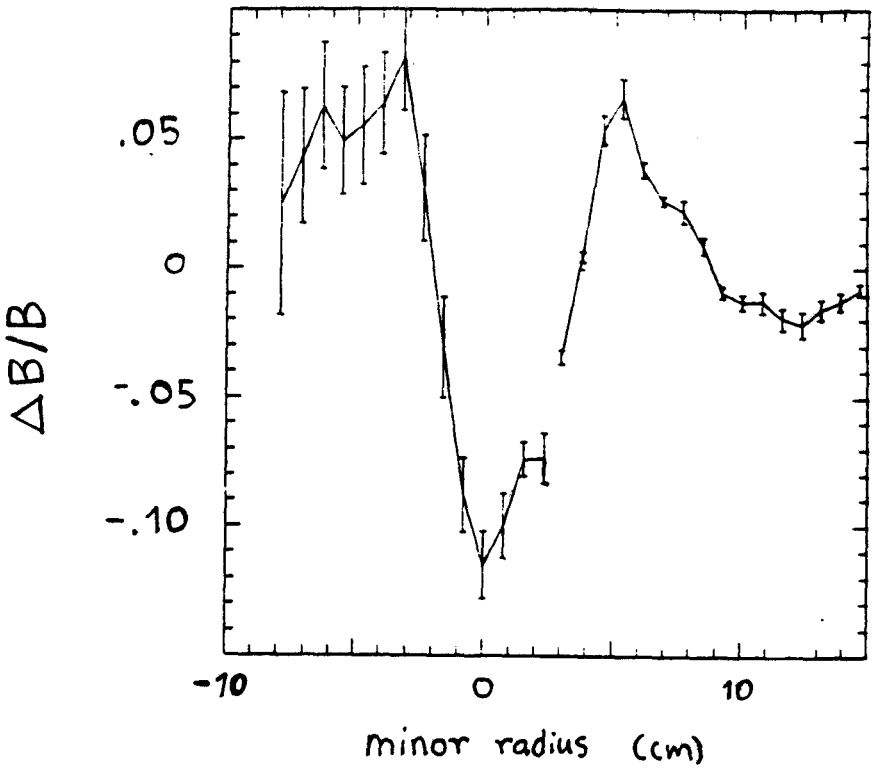

Figure 5.13 — Changes in the visible continuum brightness profile due to a giant sawtooth.

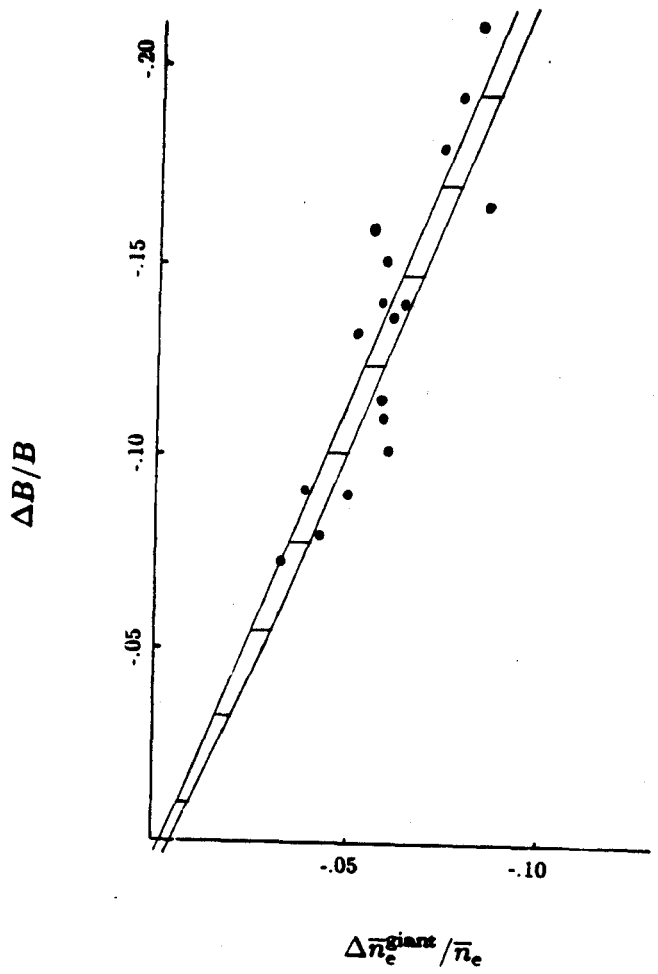

Figure 5.14 — Comparisons between measurements of $\Delta B/B$ and predictions from the sawtooth model shown in Fig. 4.9. $\bar{n}_e^{giant}/\bar{n}_e$ is defined as the relative change in $\bar{n}_e$ due to the giant sawtooth, as obtained from the central-chord interferometer measurements. The shaded area represents the span of $\Delta B/B$ predicted by the sawtooth model using the measured ranges of a_m/a and $\Delta T_{eo}/T_{eo}$ for this data ($0.37 \leq a_m/a \leq 0.43, -0.15 \leq \Delta T_{eo}/T_{eo} \leq -0.10$). $\Delta T_{eo}/T_{eo}$ is defined as the relative change in the central electron temperature due to the sawteeth as determined from central ECE emission measurements. a_m/a is the relative mixing radius as estimated from soft X-ray brightness measurements.

C are observed to have large precursors oscillations, which is consistent in this regards to the Kadomtsev model. The smaller sawteeth observed just before the giant sawtooth were shown (see Fig 5.15) to have smaller inversion radii, and are, therefore, probably not related to these 'partial' sawteeth observed on JET.

5.6 Summary and Discussion

Density profiles during high density, pellet fueled discharges have been obtained from measurements of visible continuum brightness profiles. In discharges where the pellet induced density increase is sufficiently large, $\Delta\overline{n}_e/\overline{n}_e \simeq .7 - .9$, density profiles remain more peaked after the density has decayed to a constant level. In these cases, Mo levels were observed to increase and the V^{+20} decay rate decreased. Due to the fact that the peaked density profiles are more peaked after pellet injection, effects of giant sawteeth are observable on the visible continuum brightness profiles. Just after a giant sawtooth, both the background and impurity particle transport quickly return to pre-pellet conditions. This implies that the sudden flattening of density and temperature profiles, due to giant sawteeth, is probably at least partially responsible for this change.

Thus, the more peaked post-pellet density profiles appear to be related to the changes in the particle transport. However, it is not known whether these initially more peaked profiles, due to large, penetrating pellets, directly induce changes in particle transport which are then maintained in some self-consistent manner or, whether other changes in

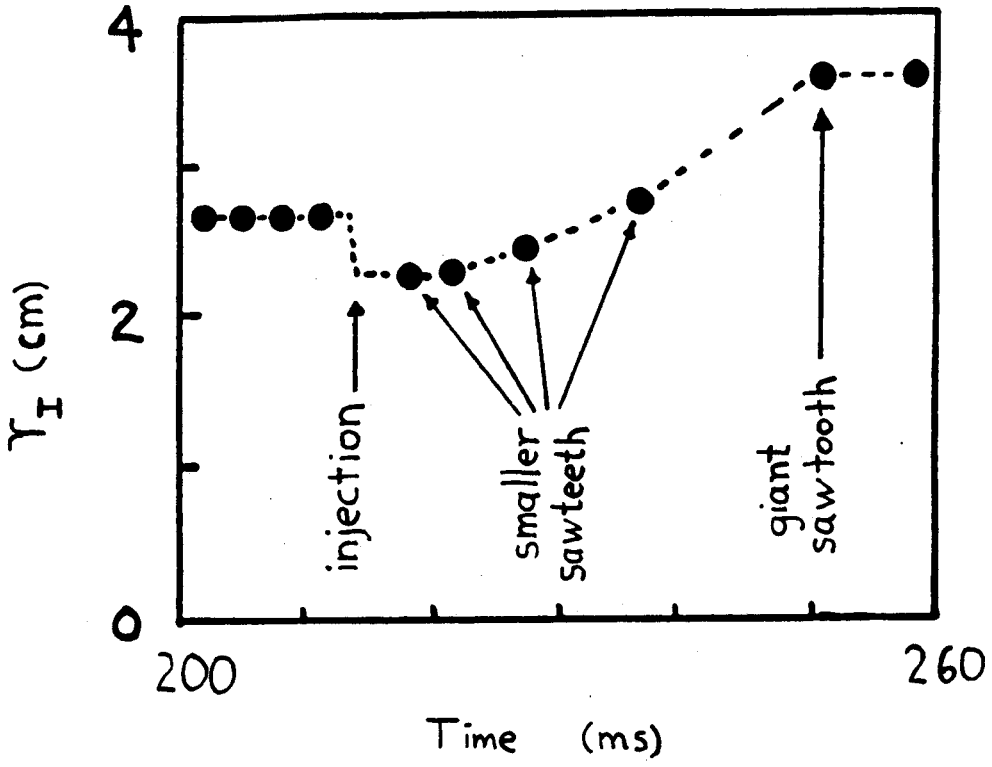

Figure 5.15 — The effects of a pellet injection on the soft X-ray inversion radius, r_I. r_I is the impact radius (inside the mixing radius r_m) in which the soft X-ray brightness is not effected by the sawtooth. The inversion radius clearly decreases after the pellet injection and then increases radially until a giant sawtooth occurs. From Ref [53].

the plasma due to the pellet injection are responsible, perhaps in conjunction with the more peaked profiles. For low current discharges, no steady-state peaking was observed after the pellet density had decayed to a constant level, even though, (for the large $\Delta\overline{n}_e/\overline{n}_e$ cases), the profiles were very peaked just after injection. Thus, simply increasing the peakedness of the density profiles is clearly not sufficient to induce a lasting change in the particle transport.

CHAPTER 6

Particle Transport During Pellet Fueled Discharges

6.1 Introduction

In this chapter, the background particle transport is determined from analysis of electron density profiles during pellet fueled discharges. As was described in the last chapter, these density profiles are determined from visible continuum brightness profile measurements for high density, clean ($\overline{Z}_{\rm eff} \simeq 1.2$) discharges. Of particular interest is the determination of the changes in the particle transport after the injection of a large large pellet, where density profiles are observed to remain peaked the pellet induced density rise has decayed to a constant value.

Radial particle fluxes $\Gamma(r,t)$ are determined, in the central region of the plasma, from analysis of $n_e(r,t)$ following the pellet injection. In order to relate the inferred flux to changes in macroscopic transport parameters (which in general may depend on $\nabla_r n, \nabla_r T, n, T...$), one must first assume a general form for the particle flux. This functional form for the flux can be motivated by both theoretical and practical considerations. For this analysis, only two terms, density gradient diffusion ($-\mathrm{D}\nabla_r \mathrm{n}$) and radial convection ($\mathrm{n}V_r$), are included. Since the results for D and V from this analysis are found to have substantial uncertainties, (due mostly to uncertainties in the data), using additional flux terms (eg. $\propto T$) would most likely result in less meaningful solutions with very large uncertainties. Particle fluxes proportional to $n\nabla_r T/T$, which are predicted in some transport theories[55,56,61], can

be determined from the calculated convection flux, since the temperature profiles are approximately Gaussian shaped, and thus, $n\nabla_r T/T \propto nr/a_T^2 (a_T \equiv$ Gaussian temperature width).

The radial flux (inside the limiter radius $r < a$) is assumed to be symmetric both poloidally and toroidally. Thus, the 1-D radial particle flux is assumed to have the form:

$$\Gamma(r,t) = -D(r,t)\nabla_r n(r,t) - n(r,t)V(r,t) \tag{6.1}$$

where, by convention, a positive V(r,t) implies an inward particle flow.

The particle transport equation is then given as:

$$\frac{\partial n(r,t)}{\partial t} + \frac{1}{r}\frac{\partial}{\partial r} r\Big\{ - D(r,t)\frac{\partial n(r,t)}{\partial r} - n(r,t)V(r,t)\Big\} = N(r,t) \tag{6.2}$$

where $N(r,t)$ is the source term, which is only significant near the edge of the plasma, once the pellet ablation is complete.

6.2. Estimating Transport Coefficients

In order to estimate the magnitudes of D and V during pellet fueled discharges, the following simple spatial and temporal forms for D and V are assumed:

$$D(r,t) = D_0 \tag{6.3}$$

$$V(r,t) = V_0 r/a \quad .$$

Equation 6.2 can now be written as:

$$\frac{\partial n(r,t)}{\partial t} + \frac{1}{r}\frac{\partial}{\partial r} r\{-D_0 \frac{\partial n(r,t)}{\partial r} - n(r,t)V_0 r/a\} = N(r,t). \tag{6.4}$$

The general Green's function solution to Eq. 6.4 is presented in Appen. A. Assuming an edge source approximated by $N(z) = N_0\delta(z - z_0)$, $(r_0/a \equiv z_0)$, steady-state profile shapes are found to be mostly dependent on the value of the 'convection parameter', S, where

$$S \equiv \frac{aV_0}{2D_0}.$$

Shown in Fig 6.1 are the steady-state profiles (from Eq. A.10) for different values of S, assuming $z_0 = .95$. Plotted in Fig 6.2 is the peak-to-average (P/A) of these profiles vs. S, for the cases $z_0 = 0.90$ and $z_0 = 0.95$. Since the profile shapes in the central region are only weakly dependent on the radial location of the source, the steady-state profiles

more realistic, distributed edge sources should also only be dependent on S.

In Appen. B the eigenvalues of the homogeneous portion of Eq. 6.4 are derived. The lowest order 'eigentime', τ_0, is found to be:

$$\tau_0 \simeq (a^2/D_0)\{(2.405)^2 - (2.000)S + (.21805)S^2 \qquad (6.5)$$

$$-(1.2487 \times 10^{-3})S^4 + (6.1507 \times 10^{-6})S^6\}^{-1}$$

This expression has been found to be accurate over the range $-5. \leq S \leq 5$. For the non-convection case of S=0, τ_0 is the lowest order Bessel decay time. For comparison, the semi-analytic expression for τ_0 given in Ref[63] yields, for S=1, $\tau_0 = .98a^2/(4D_0)$, whereas Eq. 6.5 yields $\tau_0 = 1.000a^2/(4D_0)$. A similar expression for τ_1, and a general method for obtaining the higher order τ_n's, is presented in Appen. B.

The eigenfunctions of the homogeneous part of Eq. 6.4 are found (in Appen. A) to involve confluent hypergeometric functions. However, it is interesting to note that the lowest order eigenfunction, for the case S=1, is found to have a particularly simple analytical form, given by:

$$n(z \equiv r/a) = n_0(1 - z^2)e^{-z^2}, \qquad 0 \leq z \leq 1 \ . \qquad (6.6)$$

Rough estimates for D_0 and V_0 can now be determined by using measurements of both the decay times of $\bar{n}_e$, which correspond to $\tau_0(D_0, S)$, and measurements of the steady-state profiles after the decay, which determine S (from Fig 6.2). Figure 6.3 shows calculated

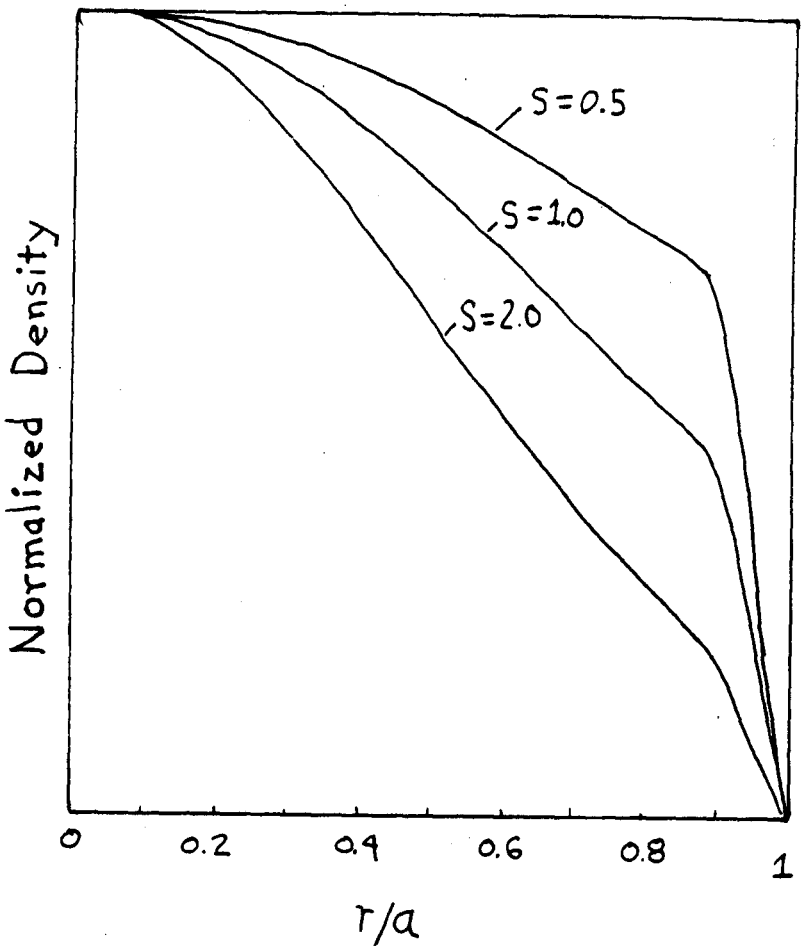

Figure 6.1 – Steady-state eigenprofile solutions using values for the convection parameter of S = .5, 1.0, and 2.0. The source is taken to be a δ function at r/a=0.9, and the profiles are normalized at origin.

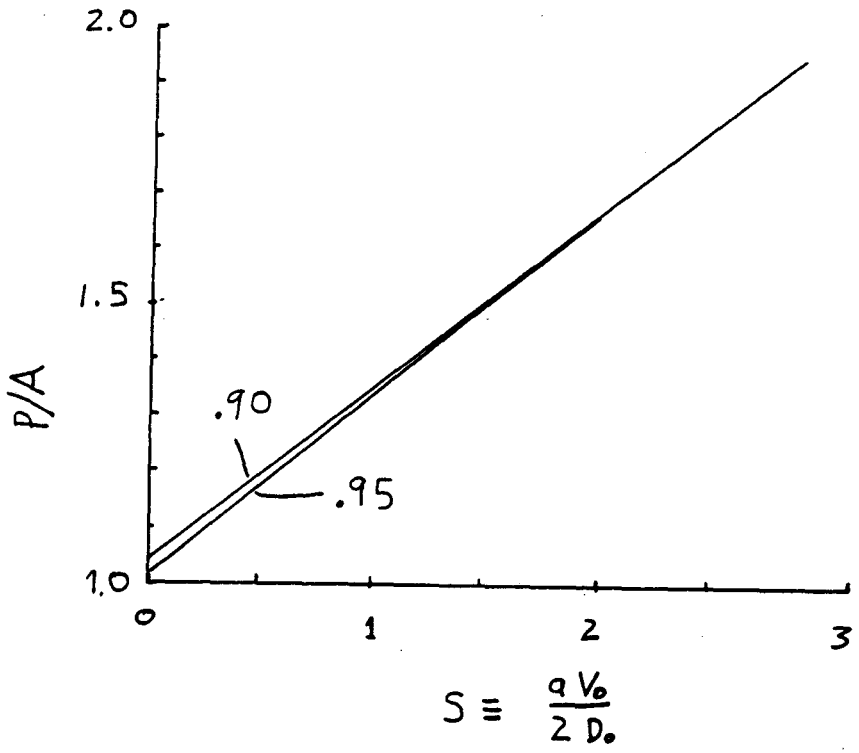

Figure 6.2 — The peak-to-average values of steady-state profiles vs. S for sources at radii r/a = 0.9 and 0.95

values of D_0 and V_0 as functions of τ_0 and S. These values are, therefore, temporal and spatial averages of D(r,t) and (r/a)V(r,t) during the density decay period.

Time-dependent Green's function simulations are performed by using the density profiles measured just after the pellet injection as the initial profiles. The magnitudes of the source, D_0, and S are then varied until the results of the simulations approximately match the measured time histories of the line-average and P/A densities.

6.3 Method For Determining $D(r,t)$ and $V(r,t)$

D(r,t) and V(r,t) can be determined within the high density, source free region of the plasma, from measurements of $n_e(r,t)$ during the density decay period. Integrating Eq. 6.2 out to a radius r results in an integral particle transport equation:

$$\frac{1}{r}\int_0^r \left[r'\frac{\partial n(r',t)}{\partial t}\right]dr' - D(r,t)\frac{\partial n(r,t)}{\partial r} - n(r,t)V(r,t) = \frac{1}{r}\int_0^r r'N(r',t)dr' \ . \tag{6.7}$$

Since the source term in Eq. 6.7, which is probably neither toroidally nor poloidally symmetric, is difficult to ascertain experimentally, V and D are calculated inside some radius, $r < r_{crit}$, where the source term is small. Assuming that the edge source is mostly due to electron-impact ionization, $N(r) \simeq n_n n_e \langle \sigma v \rangle$($n_n$ is the neutral density), and estimating $\partial n/\partial t \sim n_e/\tau_0$, r_{crit} is determined implicitly through:

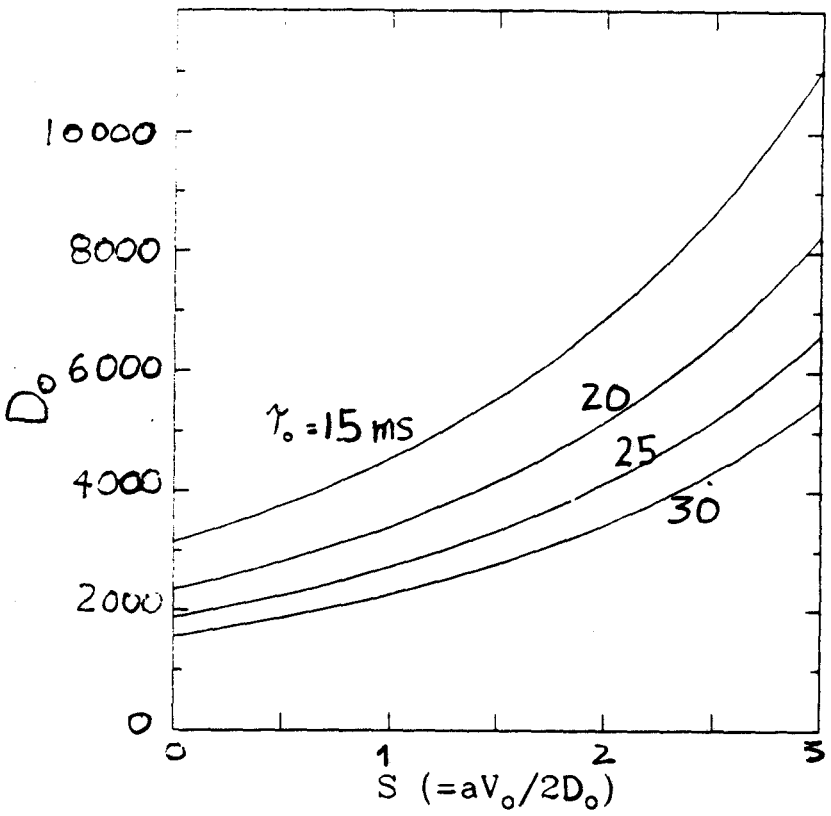

Figure 6.3a — D_0 vs S for various values of τ_0 (longest lived decay time).

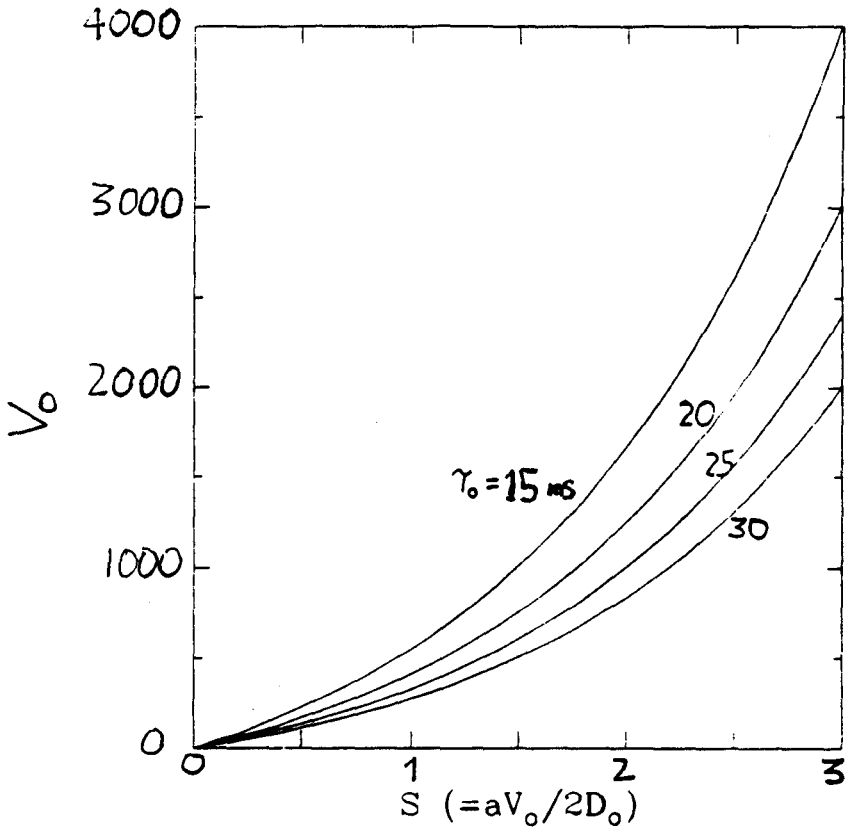

Figure 6.3b — V_0 vs S for various values of τ_0.

$$n_n(r_{crit}) \simeq \frac{1}{\tau_0 \langle \sigma v \rangle} \tag{6.8}$$

The reaction rate, $\langle \sigma v \rangle$, for ionization has a relatively weak dependence on electron temperature – for temperatures in the range 10 eV $\leq T_e \leq$ 100 eV, the corresponding rates are between $6 \times 10^{-9} \leq \langle \sigma v \rangle \leq 3 \times 10^{-8}$. [57] Using a typical decay time $\tau_0 = 30$ ms, $n_n(r_{crit})$ is calculated to be in the range $1 \times 10^9 \leq n_n(r_{crit}) \leq 5 \times 10^9$. For typical high density Alcator C discharges, this radius corresponds to $.85a \leq r_{crit} \leq .95a$. [58]

At radii r $\leq r_{crit}$, the divergence of the flux is balanced by the time derivative of the density. However, in order accurately to determine the diffusion and convection terms, it is necessary further to show that each term is separately larger than the source. This is verified *a posteriori* by noting that since S is generally found to be of order 1, the diffusion and convection fluxes must be of the same order of magnitude (although opposite signs). Both terms must, therefore, be of the same order of magnitude as the time derivative term, which was shown to dominate over the source term.

Thus, Eq. 6.7 can be rewritten as:

$$D(r,t)\frac{\partial n(r,t)}{\partial r} + n(r,t)V(r,t) = \frac{1}{r}\int_0^r r' \frac{\partial n(r',t)}{\partial t} dr' \tag{6.9}$$

which is generally valid for radii r/a $\leq$ 0.85 for typical high density Alcator C discharges.

$D(r,t)$ and $V(r,t)$ can now be determined algebraically from measurements of $n(r,t), \partial n(r,t)/\partial r$, and $\partial n(r,t)/\partial t$ at two times, t_1, t_2, assuming $D(r,t_1) \simeq D(r,t_2)$ and $V(r,t_1) \simeq V(r,t_2)$. In principle, $t_1 - t_2$ could be chosen arbitrarily small. However, due to finite uncertainties in the data, $t_1 - t_2$ must be large enough so that the changes in the profiles between t_1 and t_2 are much larger than their uncertainties.

In order to decrease the effects of the uncertainties in the profiles at times t_1 and t_2, profiles at fifty time points between t_1 and t_2 (data are digitized at 5 kHz) are used and a least-squares solution for D(r,t) and V(r,t) is computed. This results in radial profiles for D(r,t) and V(r,t), averaged over a 10 ms. time period. This algorithm was checked by inputting the Green's function solutions to Eq. 6.4 during a pellet injection simulation. Analysis of these profiles yielded the correct radial shapes (given by equation 6.3) and values of D_0 and V_0.

6.4 Results of Analysis

This section presents the results of particle transport analysis, using the previously described methods, for three common, but qualitatively different types of pellet injection discharges: 1) large post-pellet peaking, 2) discharges with giant sawteeth, and 3) high $q_l(\geq 6.5)$ discharges. In each case, D(r,t) and V(r,t) are calculated over the source free region, $r < r_{crit}$. These results are then compared with transport simulations using the Green's function solution to Eq. 6.4 given in App. A.

6.4.1 Peaking Discharges

This section presents transport analysis for discharges in which the density profiles are observed to remain peaked after the pellet injection. As shown in Fig 6.4, the peakedness of density profile is seen to increase from P/A$\sim$ 1.3 to P/A$\sim$ 1.5 after the pellet injection. Also shown is the central-chord soft-Xray brightness which increases substantially after the injection. These changes are maintained until $\sim$ 370ms.. at which time a minor disruption results in the plasma returning to pre-pellet conditions.

D(r) and V(r) are calculated using the results of Sect. 6.3, at different times after the pellet injection. Also calculated is the local convection parameter profile, $S'(r)$, defined as:

$$S'(r) \equiv \frac{aV(r)}{2D(r)}\frac{a}{r} \tag{6.10}$$

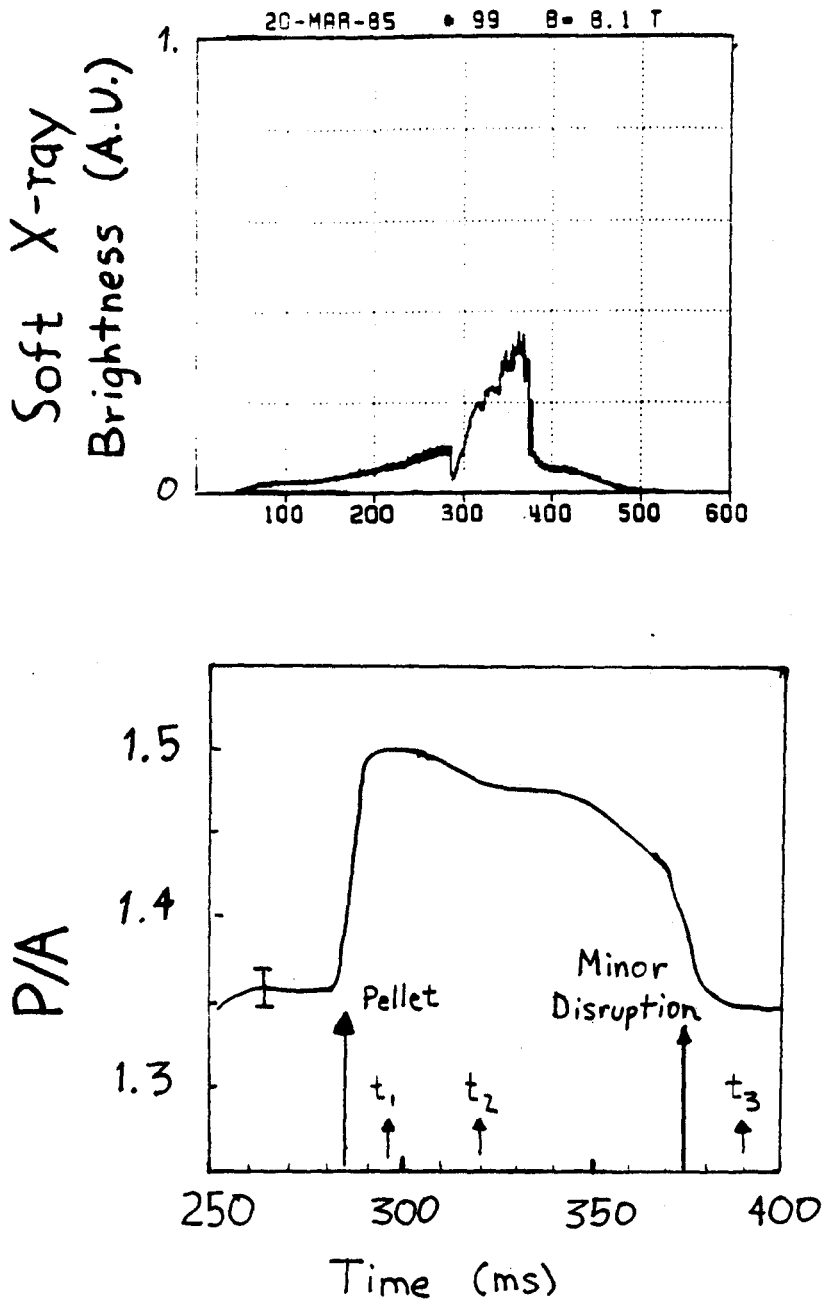

Figure 6.4 — The P/A and central soft-Xray brightness from a discharge showing peaked density profiles after pellet injection. t_1, t_2, and t_3 are the times at which D(r) and V(r) are calculated (see Fig. 6.5).

The $S'(r)$ profile is an indication of the deviation of the flat D(r) and the linear V(r) profiles given in Eq. 6.3 (which would result in a flat $S'(r)$profile).

Shown in Fig. 6.5, are the profiles of D(r), V(r), and $S'(r)$, calculated at times t_1, t_2, and t_3, as defined in Fig. 6.4. At t_1, 10 ms after injection, $S'(r)$is seen to be approximately flat with a central value near $S'(r = 0) \simeq 1.5$. Density profiles are seen to be peaked at this time. D(r) is found to have a central value of $\simeq$ 2500 cm^2/sec, while V(r) is seen to be approximately linear out to r/a=0.5, with V(r/a = 0.5) $\simeq$ 100 cm/sec.

At t_2, 35 ms. after injection, S(r) is seen to be approximately unchanged. D(r=0) is still $\sim$ 2500 cm^2/sec, but now has a more hollow profile shape. V(r) is still approximately linear, but V(r/a=0.5) has increased in value to $\sim$ 350 cm/sec. Thus, during this period when the density is decaying and the temperature is reheating, both D and V (outside $r/a \geq 0.25$) increase.

At t_3, 105 ms. after injection, the density profile has returned to a flatter, pre-pellet P/A value. V(r) is similar to the lower values found just after injection (at t_1), while D(r) appears not to change much from time t_2.

Both D and V increase during the density decay period of the discharge, possible due either to the decreasing density or the increasing temperature during that time. After 370 ms., at which time the temperature and density remain relatively constant, V(r) decreases while D(r) decreases only slightly. These results imply that the increase in the density profile peakedness after pellet injection is due to mostly to enhanced inward particle convection.

The spatial averages of D(r), V(r), and $S'(r)$ are calculated every millisecond during the density decay period. In these cases D(r), V(r), and $S'(r)$ are averages over a 5 ms time period using 25 density profiles. $\bar{D}$ and $\bar{S}'$ are defined as the averages of D(r) and S(r) out to r/a = 0.5. (Outside $r > .5$ the uncertainties in D(r) and V(r) are large due the relatively small changes in the density profiles at those radii.) $\bar{V}$ is defined as the linear average of V(r) out to r/a =0.5, multiplied by 4. If $V(r) = V_0 r/a$, this average would be equal to V_0.

Shown in Fig. 6.6 are $\bar{D}$, $\bar{V}$, and $\bar{S}'$, for this discharge (along with results from two other discharges showing similar peaking). $\bar{S}'$ is seen to remain fairly constant (near ~1.3) until 370 ms. $\bar{D}$ is seen to increase from ~ 3000 cm^2/sec just after injection, to ~ 5000 cm^2/sec, 50 ms after injection. $\bar{V}$ also increases, from $\bar{V}$ ~ 400 cm/sec to $\bar{V}$ ~ 1000 cm/sec. From Fig. 6.5, this increase in $\bar{D}$ can be attributed to changes in the D(r) profile shape.

At 370 ms., when the $\bar{S}'$ and the density P/A return to pre-pellet values, $\bar{D}$ is seen to remain approximately unchanged, while $\bar{V}$ decreases by almost a factor of 2. This again indicates that the increases in S after pellet injection are due mostly to increases in inward particle convection.

Also shown in Fig 6.6 are traces of two other peaking discharges. One trace is similar to results from the above discharge in that the decrease in the density peakedness at 355 ms is due to decreases in V, while D remains approximately unchanged. For the other discharge shown in Fig 6.6, $\bar{S}'$ is greater than 2 during the pellet density decay period. $\bar{V}$ is seen to be large as 1200 cm/sec, while the time history of $\bar{D}$ is similar to the other two discharges. This again implies that the

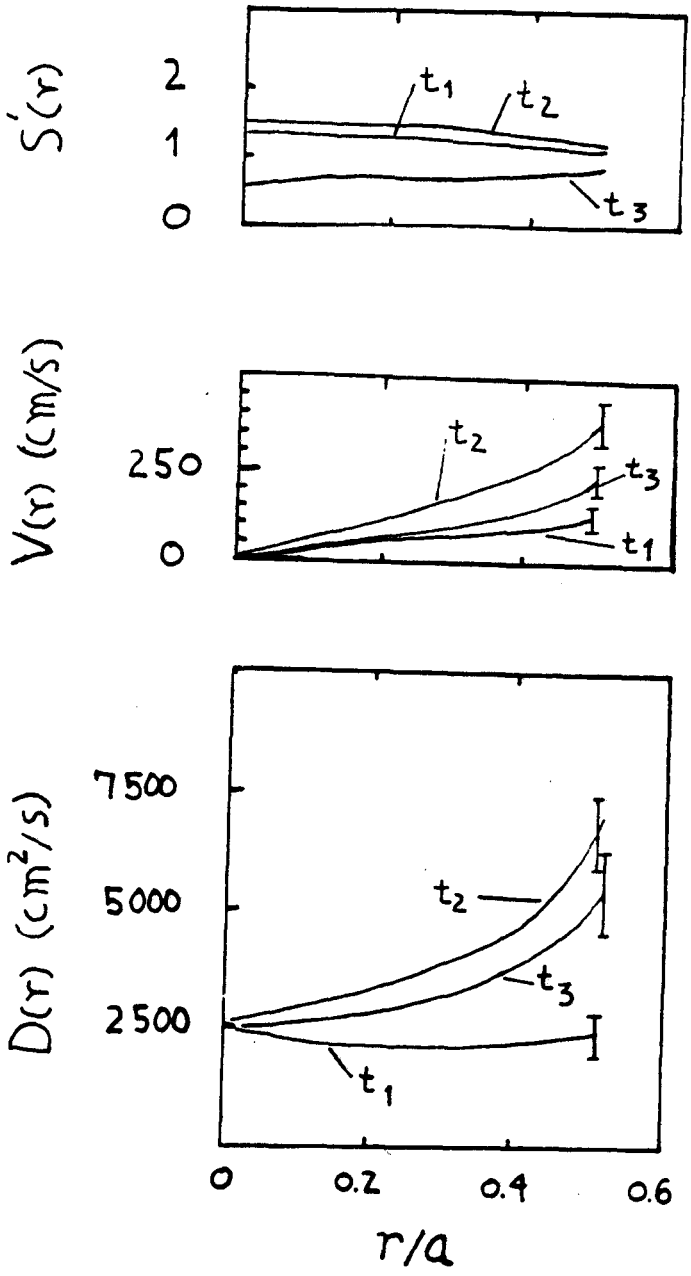

Figure 6.5 – D(r), V(r), and $S'(r)$ at times t_1, t_2 and t_3 for the peaking discharge shown in Fig 6.4. Error bars are calculated from linear regression analysis of profiles.

highly peaked (large $\bar{S}'$) discharges are mostly due to an enhanced inward convection.

A simulation of the peaking discharge of Fig. 6.4, along with the measured density data, is shown in Fig 6.7. Before the pellet injection, the density profiles are simulated by using the steady-state eigenprofiles solutions (Fig 6.1) having the same P/A as the measured data. Profile simulations are then started using the measured density profile just after the pellet injection, when $\overline{n}_e$ is maximum. The transport associated with the fast profile changes during the pellet ablation and density rise ($\leq 1-2$ ms) are not included in these simulations. D_0 and V_0 are initially estimated using the results of Fig. 6.2, and are then iteratively varied in order to obtain a 'best fit' to the data. N(r,t) is assumed to have the form: $N(r,t) = N_0\delta(z - z_0)$ with z_0 at .90. N_0 is determined from the final line-average density (after the density increase from the pellet has decayed to a constant value).

Using values of $D_0 = 3200$ cm^2/sec and $V_0 = 360$ cm/sec, the measured line-average density and the P/A during the density decay are fairly well simulated. These estimates for D_0 and V_0 are close to the values of $\bar{D}$ and $\bar{V}$ given above for times just after the pellet injection. This is due to fact that these 'best fit' values for D_0 and V_0

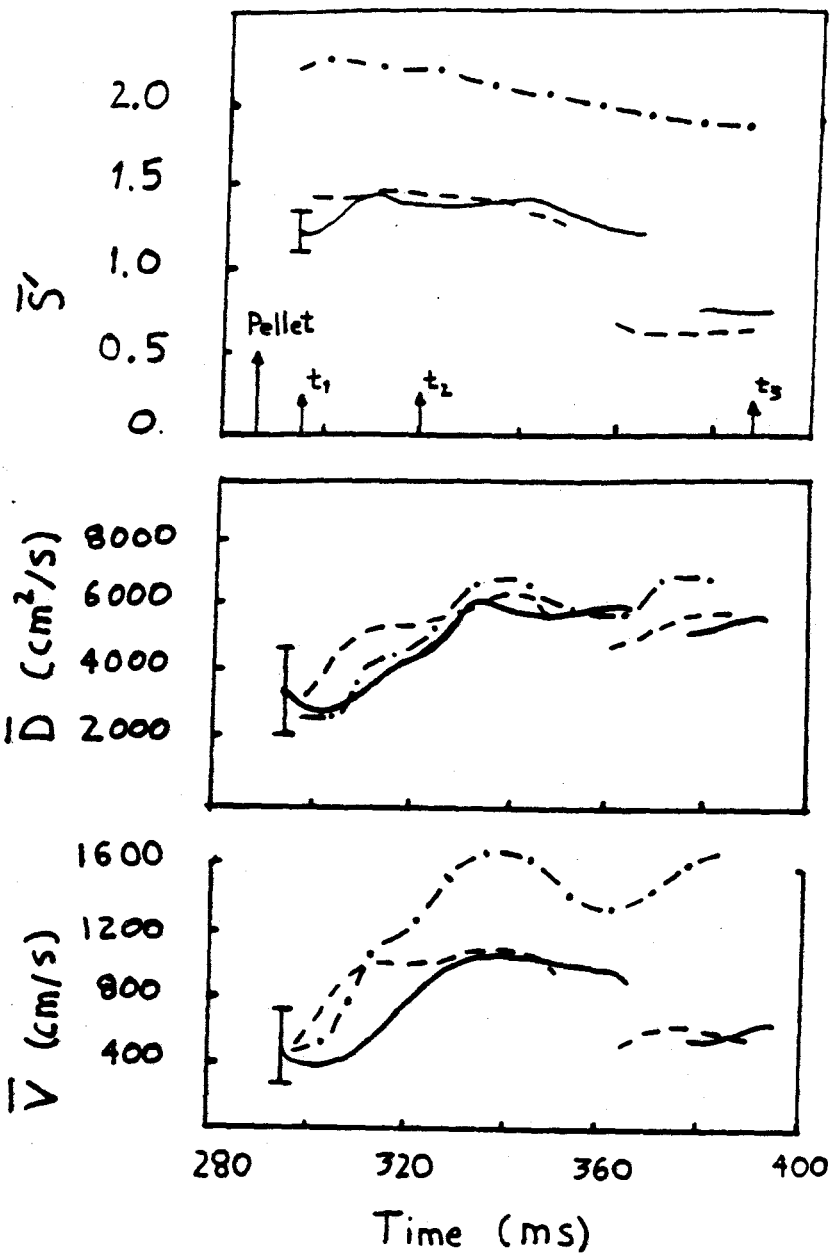

Figure 6.6 — The solid traces are $\bar{D}$, $\bar{V}$, and $\bar{S}'$ for the peaking discharge of Fig. 6.4. The effective transport during the transition period near 370 ms. (near 355 ms for dashed curve) is not shown. The dashed traces are the results from two other peaking discharges, one which returns to flatter, pre-pellet profiles after 355 ms, while the other remains peaked. Traces are smoothed ~ 10 ms with error bars indicating the approximate scatter.

are most sensitive just after the pellet injection, when the density profiles are changing the most quickly. V_0 (normalized to 1 before the injection) is found to increase to 1.3 after the injection.

6.4.2 Discharges with Giant Sawteeth

Giant sawteeth, as discussed in Sect 5.4, are sawtooth-like instabilities, which generally result in prompt a return to flatter, pre-pellet density profile and pre-pellet impurity transport. Typical traces from a discharge with a giant sawtooth are shown in Fig 5.2.

As shown in Fig 6.8, just before the giant sawtooth, D(r) is hollow, with a central value of D(r=0) $\simeq$ 2000 cm^2/sec, $S'(r)$ is flat, with a central value of $S'(r=0) \simeq 1.1$, and V(r) is approximately linear with r, with V(r/a = 0.5) $\simeq$ 350 cm/sec. After the giant sawtooth, $S'(r)$ and V(r) are seen to decrease, while D(r) remains relatively unchanged.

As shown in Fig 6.9, $\bar{D}$ remains unchanged after the giant sawtooth, while both $\bar{V}$ and $\bar{S}'$ are seen to decrease. Comparing Figs 6.9 and 6.7, the time histories of $\bar{D}$ are similar over most of the discharge, while after the giant sawtooth, $\bar{V}$ is lower than for the peaking case until after 370 ms, when the peaking discharge returns to a flatter, pre-pellet condition. This again provides evidence that changes in $\bar{V}$ after pellet injection are responsible for the peaked profiles found both before giant sawteeth, and during the peaked discharges presented in the last section.

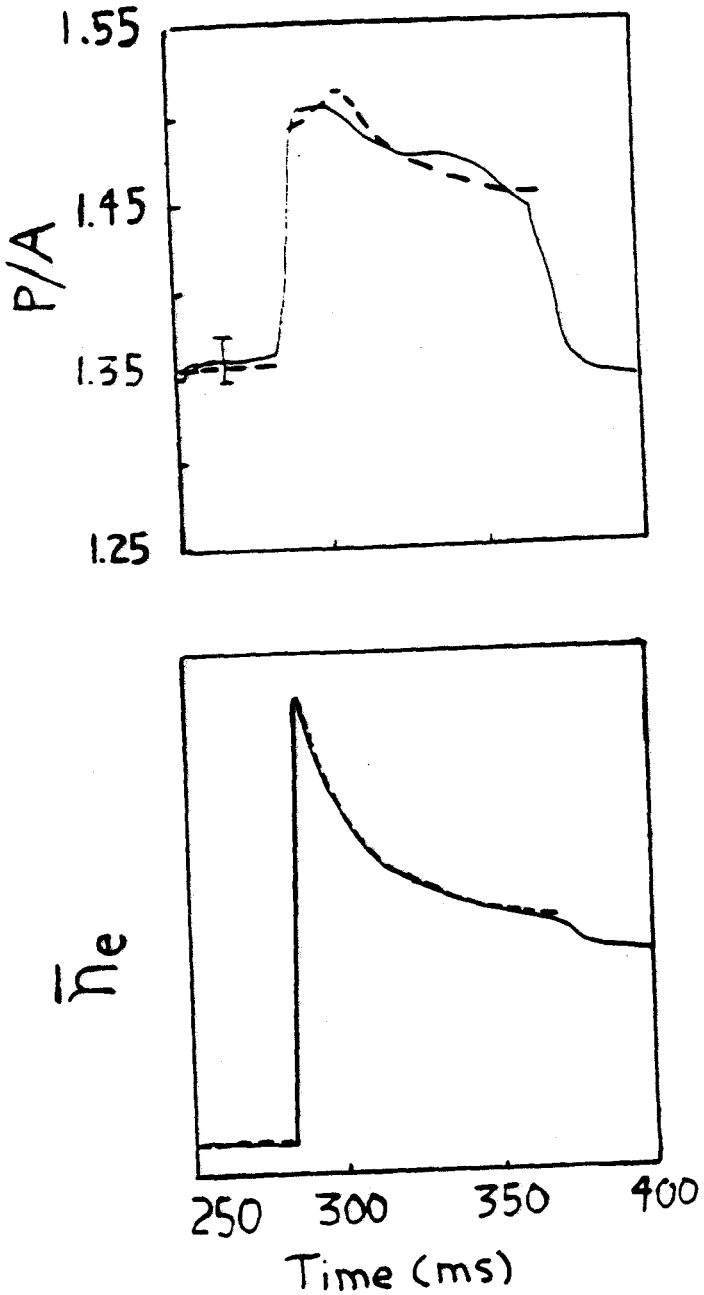

Figure 6.7 — Comparison between simulated results (dashed) and measured line average and P/A density (solid). Simulation uses values of D_0 = 3200 cm^2/sec and V_0 = 360 cm/sec during the decay.

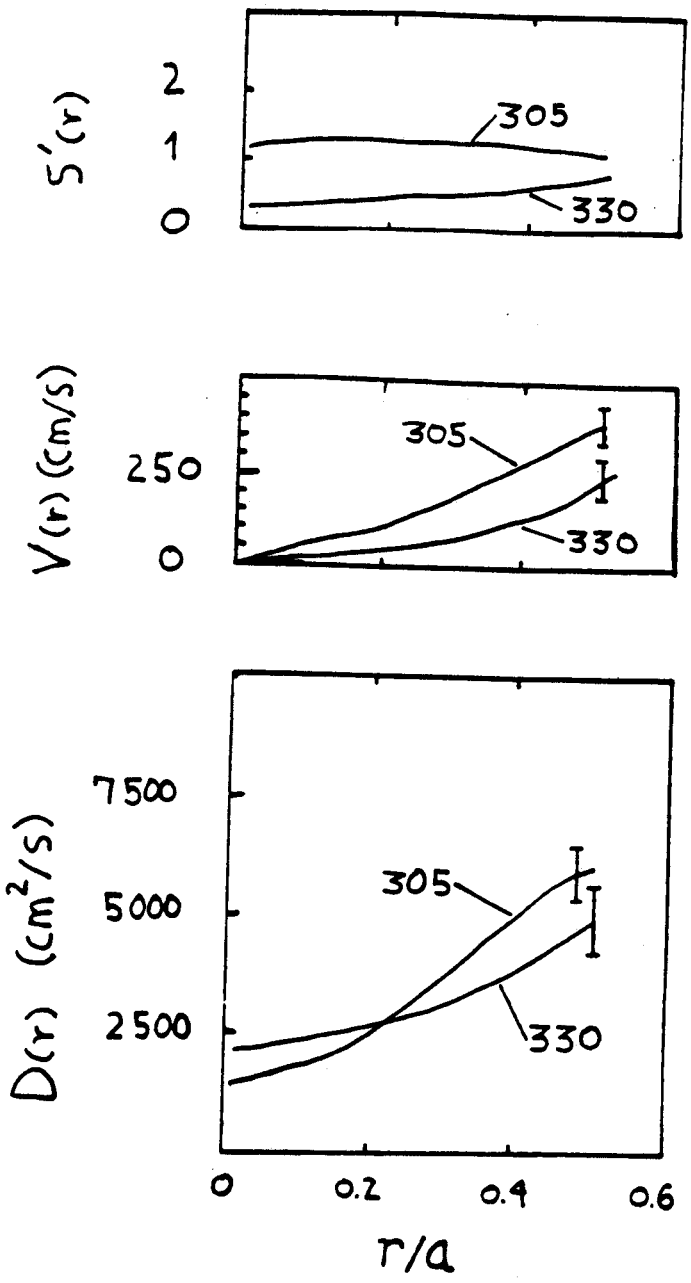

Figure 6.8 — D(r), V(r), and $S'(r)$ before (t=305 ms) and after (t=330 ms) a giant sawtooth.

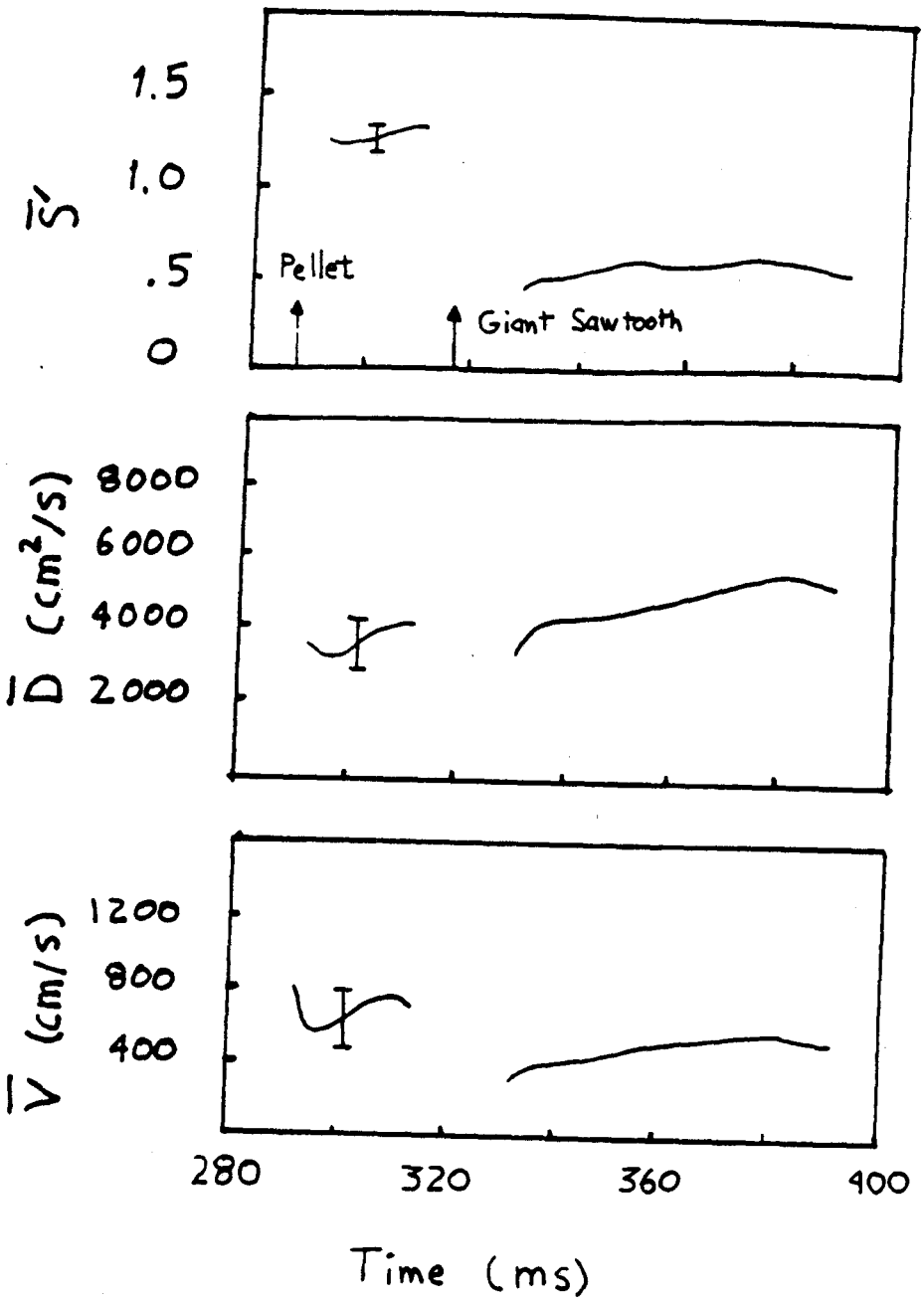

Figure 6.9 — $\bar{D}$, $\bar{V}$, and $\bar{S}'$ for the giant sawtooth discharge of Fig. 6.8. The effective transport (see Sect 6.4.4) due the giant sawtooth near 317 ms. is not shown.

A simulation of a pellet fueled, giant sawtooth discharge, is shown in Fig 6.10. 'Best fit' values obtained are: D_0 = 4300 cm^2/sec, V_0 = 690 cm/sec before the giant sawtooth, and D_0 = 4300 cm^2/sec, V_0 = 450 cm/sec after the giant sawtooth. These results are in reasonable agreement with results of Fig. 6.9 before and after the giant sawtooth. N(r,t) is again assumed to have the form: $N(r,t) = N_0\delta(r - r_0)$, with r_0 at .90. N_0 is seen to increase from 1.22 before the giant sawtooth to 1.53 after the giant sawtooth.

6.4.3 High q_l Discharges

Low current, high q_l ($q_l \geq 6.5$) discharges are characterized by a faster post-pellet density decay time and, as shown in Fig. 5.9, exhibit no lasting profile peaking effects after pellet injection, even for the largest pellet induced density increases.

Shown in Fig. 6.11 are the calculated values of D(r), V(r), and $S'(r)$ at 10 ms. and 55 ms. times after the pellet injection. Just after injection, D(r) is seen to be relatively flat, with a central value of D(r=0) $\simeq$ 3500 cm^2/sec, $S'(r)$ is flat with a central value of $S'(r = 0) \simeq 1.3$, and V(r/a = 0.5) $\simeq$ 100 cm/sec.

55 milliseconds after the pellet injection, the central value of $S'(r)$ is seen to decrease to $S'(r = 0) \simeq 0.5$, while V(r) and D(r) increase near r/a $\simeq$ 0.5.

Shown in Fig. 6.12 are $\bar{D}$, $\bar{V}$, and $\bar{S'}$, calculated every millisecond during the density decay period. $\bar{S'}$ is seen to decrease from $\sim$ 1.3

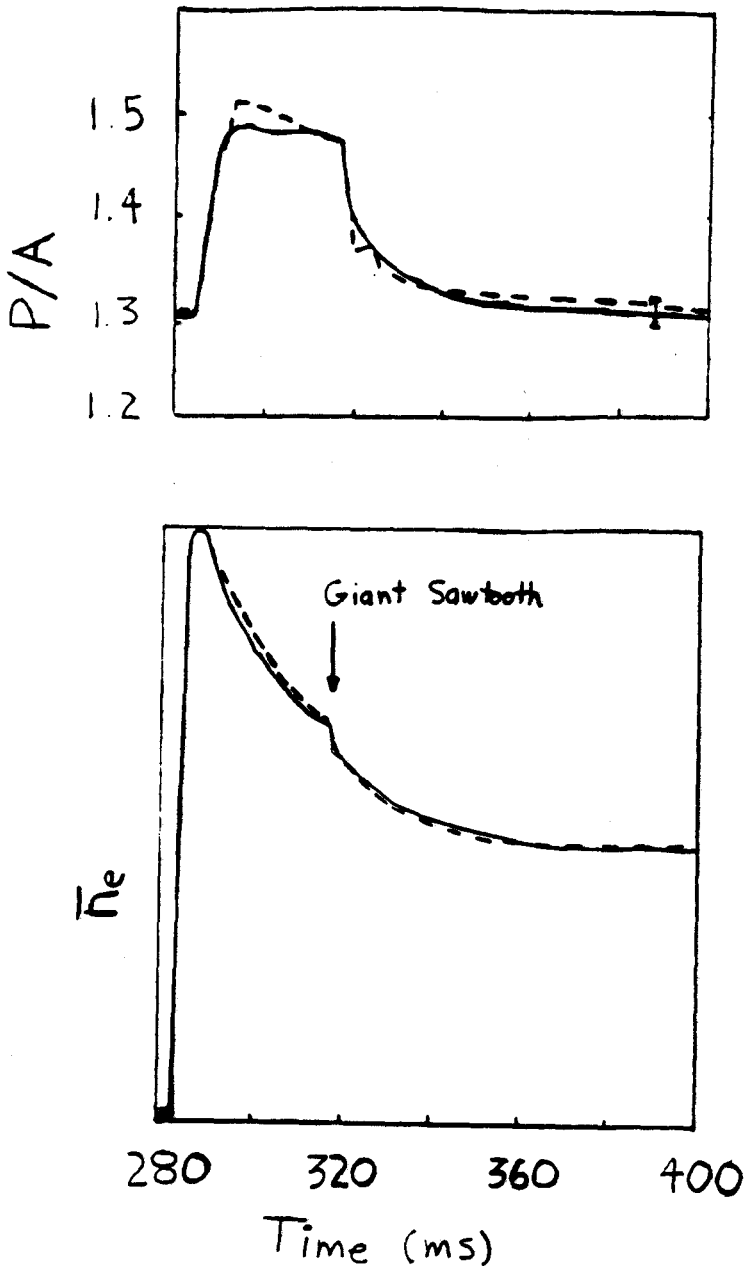

Figure 6.10 — Comparsion between simulated (dashed) and measured line average and P/A density (solid). Simulation uses D_0 = 4300 cm^2/sec and V_0 = 690 cm/sec before the giant sawtooth. Giant sawtooth is simulated by flattening profile inside radius r/a = 0.4 at 317 ms, and then changing transport parameters to D_0 = 4300 cm^2 sec and V_0 = 450 cm/sec.

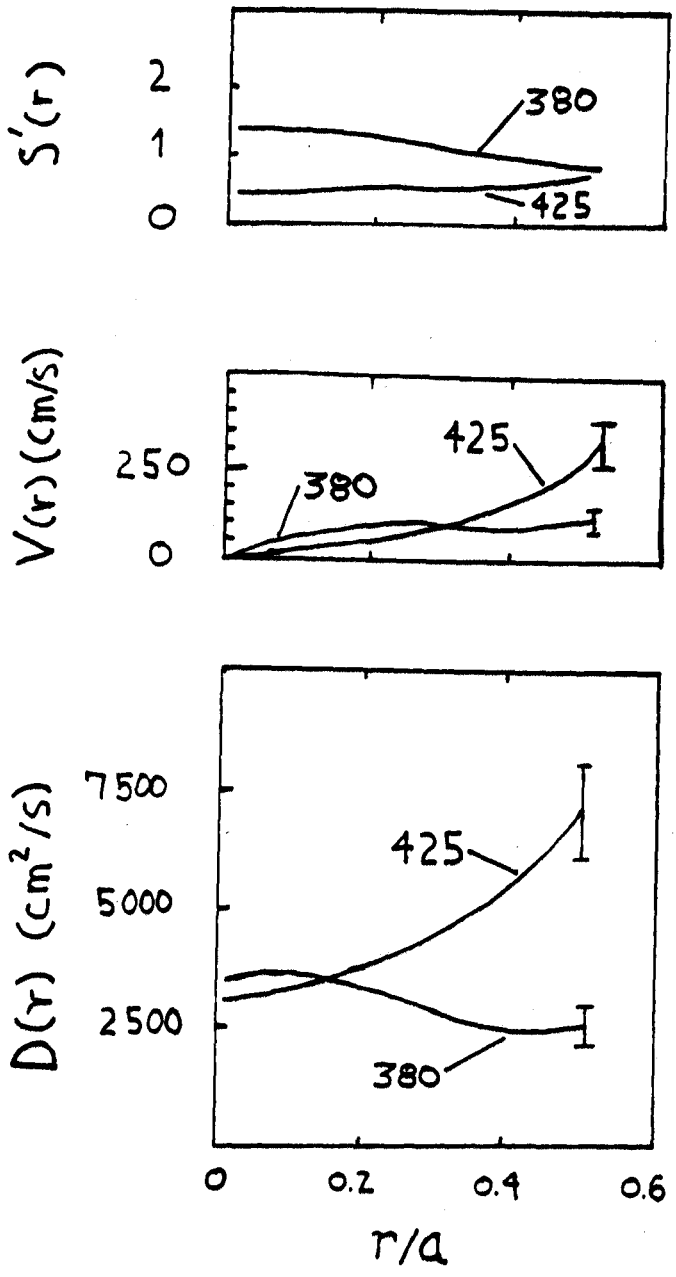

Figure 6.11 – D(r), V(r), and $S'(r)$ 10 ms.(t=380) and 55 ms. (t=425) following pellet injection for a high q_l discharge.

just after injection, to $\sim$ 0.65, 55 ms. after injection. $\bar{D}$ is found to increase from $\sim$ 3000 cm^2/sec to $\sim$ 7500 cm^2/sec, while $\bar{V}$ is seen to remain near 600 cm/sec. This value for $\bar{D}$ is larger than for the previous cases (all of which were less than 6000 cm^2/sec), although the large uncertainty in the absolute amplitudes make this comparison questionable. This larger value for D is, however, consistent with the fact that lower particle confinement is found for low current discharges[64].

A simulation of this high q_l discharge is shown in Fig 6.13. 'Best fit' values obtained are: D_0 = 2800 cm^2/sec, V_0 = 315 cm/sec, N_0 = 1.12. The simulated line-average density fits the data fairly well, while the P/A clearly is not as accurate. This is due to the fact that (as shown in Figs. 6.11 and 6.12) $\bar{S}'$ changes by a factor of 2 during the first 20 ms. after the injection. These 'best fit' simulation values are close to the measured values of $\bar{V}$ and $\bar{D}$ just after the pellet injection, when the density is decaying most quickly.

6.4.4 Discussion of Results

In summary, for all three cases presented above, the D(r) profiles are usually found to be slightly hollow, both during the peaked and non-peaked portion of the discharge, (although D(r) is usually flat just after pellet injection). It is interesting to compare D(r) profiles obtained at JET[66] during ICRF experiments. It was found that after switching off $\sim$2 MW of ICRF power, the neutral particle influx decreases almost instantaneously, which then results in a decay of the

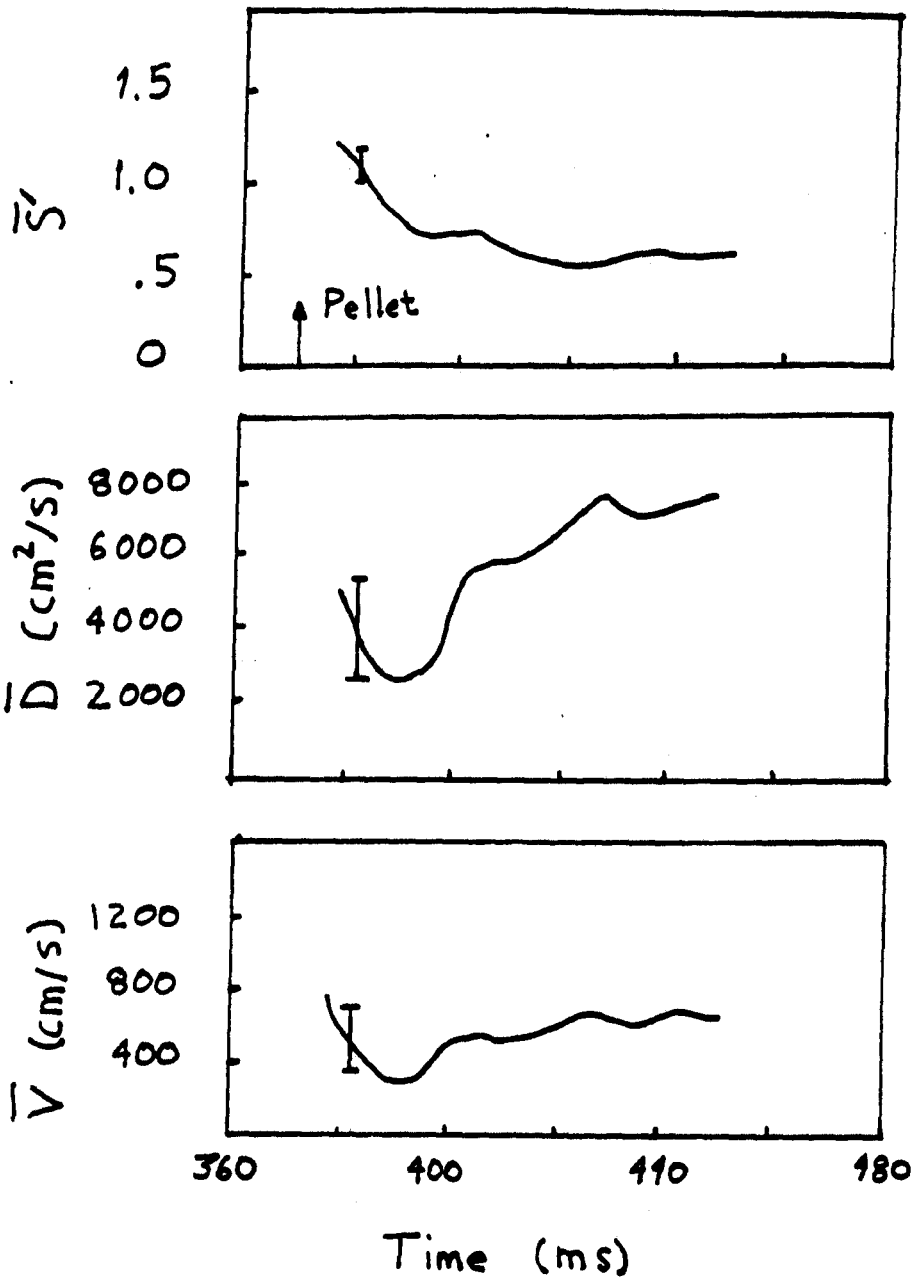

Figure 6.12 — $\bar{D}$,$\bar{V}$ .and $\bar{S}'$ for the high q_l discharge of Fig. 6.11.

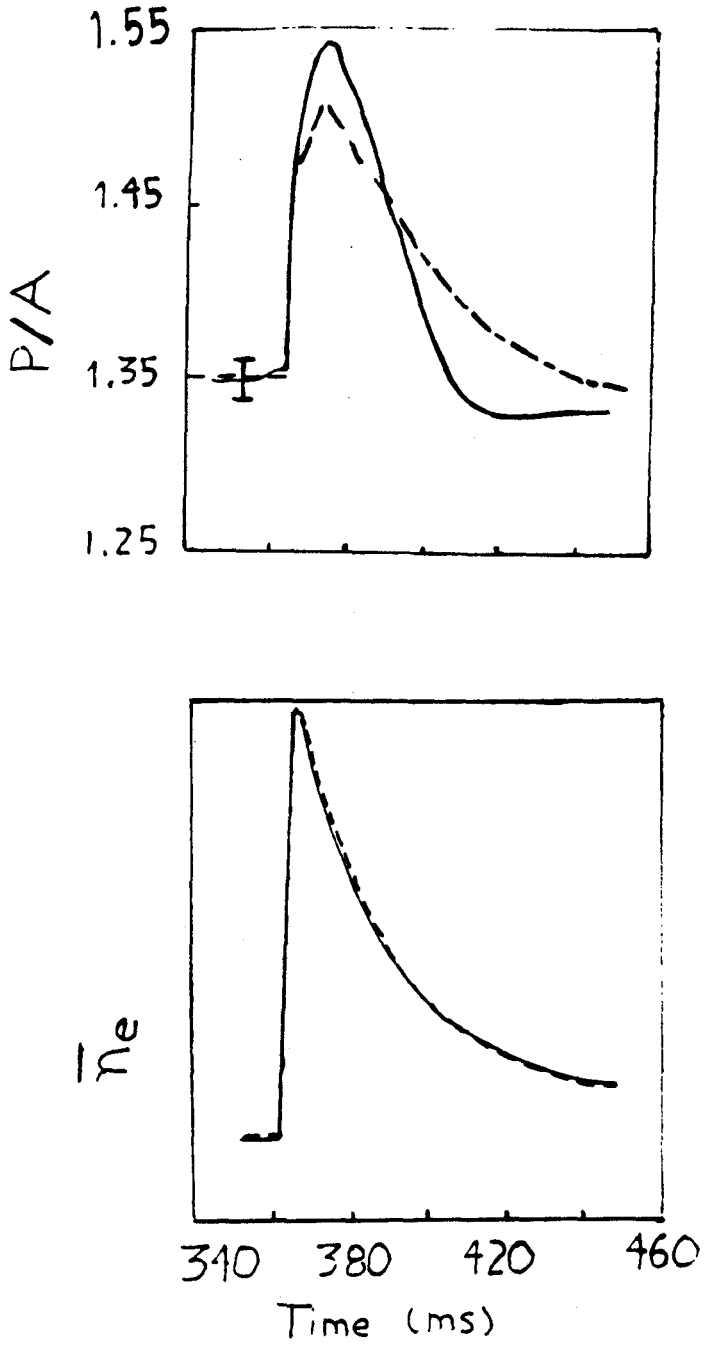

Figure 6.13 — Comparison between simulated (dashed) and measured line-average and P/A density (solid) for high q_l discharge. Simulation uses values of D_0 = 2800 cm^2/sec and V_0 = 315 cm/sec.

background density. Analysis of the density profiles during the decay period indicated that in order to accurately simulate the density profiles, the D(r) profile needed to be slightly hollow, given analytically as: $D(r) = D_0(1 + \alpha_n r^2/a^2)$, where $D_0 = 3300$ cm^2/sec and $\alpha_n = 2$. This result is very similar to the central values and the profile shapes of D(r) shown in Figs. 6.5, 6.8, and 6.11. It is surprising that these results are so similar, given the fact that the JET plasma density was approximately 10 times lower ($n_e(0) = 3 \times 10^{13}$ cm^{-3}) and the central temperature was slightly higher (2.5 keV) than that in the Alcator C discharges.

It should also be noted that sawtooth activity is usually not observed during the density decay period for Alcator C discharges which exhibit post-pellet peaking. In order to determine the effects of sawteeth (both giant and periodic) on the inferred values of $\bar{D}$ and $\bar{V}$, simulated density profiles were periodically flattened inside a typical sawtooth mixing radius and then analyzed using the methods of Sect 6.3. Results indicated that the effects of giant sawteeth were to decrease the calculated values of $\bar{D}$ and $\bar{V}$ substantially near the sawtooth crash time, in some cases resulting in negative values for both. Clearly negative diffusion is unphysical, but in this case is due to the effective transport from the sudden density profile changes. For example, if 50 density profiles (spanning a 10 ms. time period) are used to determine D(r) and V(r), D(r) and V(r) cannot be accurately determined in the 10 ms. time period around the giant sawtooth (5 ms before and after the crash time). This effect is observed in Fig. 6.6 (near 370 ms - solid, and 355 ms - dashed) and Fig 6.9 (near giant sawtooth).

The effects of small periodic sawteeth on the relatively flat density profiles, found in discharges after a giant sawtooth, were also studied. $\bar{D}$ and $\bar{V}$ are both found to decrease, approximately by the same proportion, with the average decrease (averaged over a sawtooth period) depending on the assumed mixing radius, the sawtooth period, and the background density peakedness. This implies that the enhanced values for V found in peaking discharges, are not directly due to the lack of sawteeth at that time, since only V (not D) was found to decrease when the profiles return to flatter pre-pellet (sawtoothing) conditions. Furthermore, small sawteeth are often observed prior to the giant sawtooth, while $\bar{V}$ is found to be larger at that time. Therefore, it is concluded that changes in sawtooth activity after pellet injection are probably not responsible for the observed changes in $\bar{V}$.

The sensitivity of these values for $\bar{D}$ and $\bar{V}$ to variations in the digital filtering time period τ_b of the raw brightness signals was also studied. As shown in Figs. 5.6, 5.9, and 5.12, $\bar{D}(t)$ and $\bar{V}(t)$ are smoothed over a 10 ms. time period, with the error bars indicating the approximate scatter in the data. Increasing τ_b was found to decrease the scatter in the resulting $\bar{V}(t)$ and $\bar{D}(t)$ traces. However, when τ_b was increased to a value close to the averaging time for the D(r) and V(r) profiles (number of density profiles used to determine D(r) and V(r) divided by the data digitization rate), the smoothed traces of $\bar{D}(t)$ and $\bar{V}(t)$ decreased noticeably ($\simeq 50\%$). Thus, the brightness signals used to determine $\bar{D}(t)$ and $\bar{V}(t)$ in the previous sections were

smoothed over 1 ms., resulting in less scatter in $\bar{D}(t)$ and $\bar{V}(t)$, but with no appreciable change in their average values.

6.5 Theoretical Comparisons

Neoclassical particle transport theory[55] predicts the background particle transport that should be present in axisymmetric toroidal confinement systems. Using the approximations $T_e \sim T_i$ and $\nabla n_e \sim \nabla n_i$, neoclassical particle fluxes can be written as:

$$\Gamma^{neo} = D_n^{neo}\frac{\partial n}{\partial r} + nV^{neo} + D_T^{neo}\frac{n}{T}\frac{\partial T}{\partial r} \tag{6.11}$$

Since temperature profile shapes remain relatively constant and approximately Gaussian shaped (of width a_T) after injection, the last term in Eq. 6.11 is $\propto -2nr/a_T^2$. Eq. 6.12 can thus be written as:

$$\Gamma^{neo} = D_n^{neo}\frac{\partial n}{\partial r} + nV_T^{neo} \tag{6.12}$$

where V_T^{neo} includes the temperature gradient induced flux. Shown in Fig 6.14 are the neoclassical diffusion and convection velocity profiles (from Ref[55]), for the peaking discharge of Fig 6.4, calculated before pellet injection and during the peaking period of the discharge. D_n^{neo} clearly has a much smaller amplitude and has a different profile shape than that which is measured (even with the inclusion of the Hinton-Chang correction[59] which can increase both D_T^{neo} and V_T^{neo} by a factor of $\sim 1.0 - 1.5$, depending on the collisionality and minor radius).

V_T^{neo} is also smaller than the measured values over most of the plasma radius, although near the origin, where V_T^{neo} is maximum, the

measured values are similar to the neoclassical predictions. This result is consistent with fact that the *net* particle flux near the origin, during non-pellet ohmically heated plasmas has previously been reported to be approximately neoclassical[69], (from analysis of the density profile re-peaking between sawteeth). Since the density profiles are centrally quite flat for these non-pellet discharges, $\partial n/\partial r$ is small near the origin, and the *net* flux near the origin is due mostly due to inward convection. Thus, these results and the convection velocities found near the origin after pellet injection, are consistent with neoclassical values. However, the magnitudes of D_n^{neo} and V_T^{neo} are much smaller than the measured values over most of the plasma radius, and are calculated to change very little after injection (see Fig. 6.13). Therefore, the changes in particle transport which are responsible for the more peaked density profiles observed after pellet injection, are probably not due to changes in neoclassical fluxes.

A transport mechanism which appears, at least qualitatively, to be consistent with some of the results of Sect. 6.4, is the η_i mode ('mixing mode'[60]). The η_i mode is a temperature gradient driven instability which results in both increased diffusion and convection, and was originally proposed as a possible explanation for the anomalously fast density rise times in Alcator discharges[60]. When the local value of η_i, defined as $\eta_i \equiv \frac{\partial ln(T_i)}{\partial r} / \frac{\partial ln(n_i)}{\partial r}$ (the ratio of the density scale length to the temperature scale length) is sufficiently large, ion-acoustic waves are predicted to induce radial particle fluxes. Since the density profile shapes during pellet fueled discharges have been correlated with changes in particle transport, it is interesting to compare predictions for D and V from this theory with the measured values.

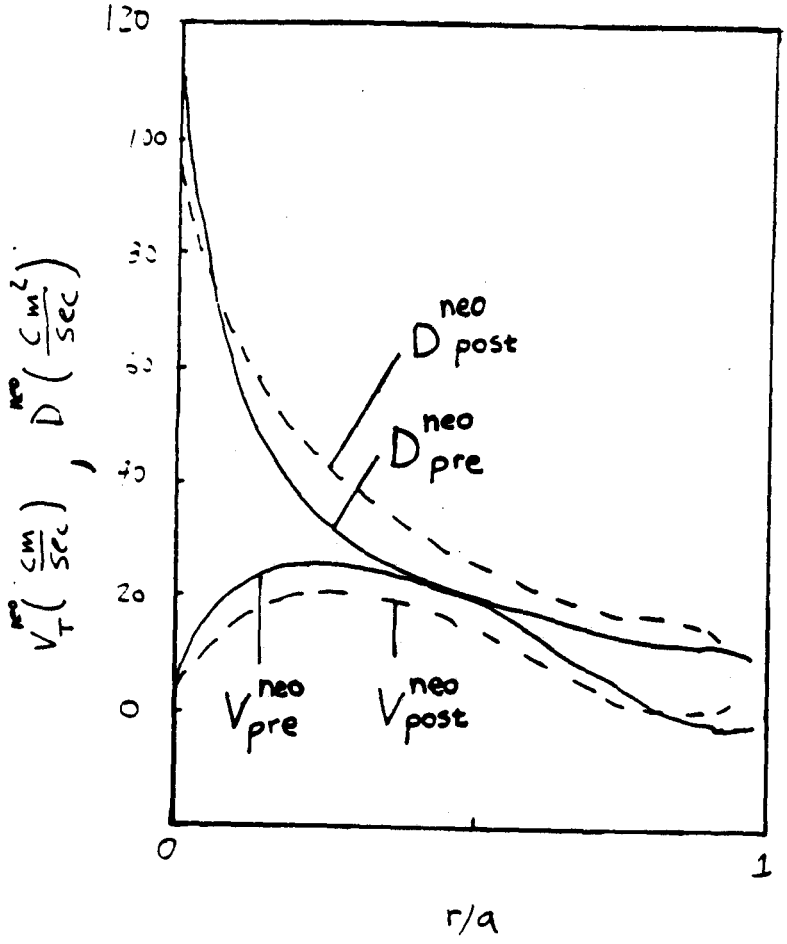

Figure 6.14 — Neoclassical values for D and V (from Ref [55]), calculated before injection (solid) and 30 ms. after (dashed) injection, for peaking discharge shown in Fig. 6.4. Pre-pellet discharge parameters are: $n_e = n_0(1-r^2/a^2)^{.5}, n_0 = 2.2 \times 10^{14}\text{cm}^{-3}; T_e = T_0 e^{-r^2/(.55a)^2}, T_0 = 1500\text{eV}; E_t = 0.5\text{V}$. Post-pellet discharge parameters are: $n_e = n_0(1-r^2/a^2)^1, n_0 = 4.4 \times 10^{14}\text{cm}^{-3}; T_e = T_0 e^{-r^2/(.55a)^2}. T_0 = 1200\text{eV}; E_t = 0.7\text{V}$. E_t is the estimated toroidal electric field used to calculate the neoclassical Ware pinch.

The particle flux predicted from η_i transport theory[56,61,62] can be written (for $\eta_i \simeq \eta_e$) as:

$$\Gamma_\eta = -D_\eta \left[\frac{\partial n}{\partial r} - \frac{1}{c_T} \frac{n}{T_e} \frac{\partial T_e}{\partial r} \right] \tag{6.13}$$

where D_η is non-zero only for the case $\eta_i > \eta_{crit} \simeq 1.5$(Ref 62), and positive values of c_T imply inward particle convection.

In the collisionless regime, ($\nu_e^* < 1$), the dissipative trapped-electron response results in a phase-shift between the fluctuating particle density and the fluctuating electrostatic potential of the wave. The net particle flux, in this regime, is found to be directed radially outward ($c_T < 0$). Assuming $\eta_e \simeq \eta_i$, D_η can be written as[62]:

$$D_\eta(r) = 2\epsilon^{3/2} \left[\frac{\pi}{2} \ln(1+\eta_i) \right]^2 \left(\frac{1+\eta_i}{\tau} \right)^3 \frac{C_s^2 \rho_s^2}{\nu_{ee} L_s^2} \tag{6.14}$$

where C_s is the sound speed ($C_s \equiv \sqrt{T_e/m_i}$), $\tau \equiv T_e/T_i$, $\rho_s \equiv C_s/\omega_{ci}$, $\epsilon \equiv r/R_o$, and $q\ L_s \equiv (\epsilon/q)\partial q/\partial r$. $q(r)$ is estimated as $q(r) \simeq q_0 + (q_l - q_0)r^2/a^2$.

Using the approximation $T_e = T_0 e^{-r^2/a_T^2}$, Eq. 6.13 can be rewritten as:

$$\Gamma_\eta = -D_\eta \frac{\partial n}{\partial r} - n \frac{2 D_\eta r}{c_T a_T^2} \tag{6.15}$$

$$\Gamma_\eta = -D_\eta \frac{\partial n}{\partial r} - n V_\eta \tag{6.16}$$

where $V_\eta(r) \equiv -2D_\eta r/c_T a_T^2$, and positive values of the V_η represent inward flow. In the collisionless regime, ($\nu_e^* < 1$), $c_T = -4/3$, and thus, V_η is directed radially outward. For typical post-pellet Alcator C discharges, ν_e^* is, in fact, less than or close to one over most of the central

portion of the discharge. For this analysis, it will be assumed that the collisionless theory is applicable, since an extension of this theory into the more collisional plateau regime is not yet available[70].

Qualitatively, these theoretical results can be seen to be consistent with some of the results of Sect. 6.4. The effects of a negative convective flow on the background transport would be to decrease the resulting value of the convection parameter S. Assuming that η_i transport decreases or 'turns off' after a pellet injection, the convection parameter, S, would then be predicted to increase, resulting in more peaked density profiles, which could then be maintained self-consistently if η_i remains below $\eta_{i,crit} \simeq 1.5$. After a giant sawtooth, when density profiles return to flatter pre-pellet conditions, η_i increases, resulting in a 'turning on' of the η_i transport and a decrease in S. In high q_l discharges, where the temperature profiles are generally more peaked, η_i would not decrease to the same level (near η_{crit}) after pellet injection, even for large pellet density increases.

A more quantitative comparison can be made by estimating the effects of η_i transport on changes in S, D, and V. A simple model is first constructed which assumes that the total transport is due the combination of η_i transport and a constant background transport. A local convection parameter, $S'_\eta(r)$, due only to the η_i mode, is written as: $S'_\eta(r) = a^2 V_\eta(r)/2r D_\eta(r) = a^2/(a_T^2 c_T) \equiv S_\eta$. Using the value $a_T/a = 0.55$, $S_\eta \simeq -2.5$ in the collisionless regime. For more peaked temperature profiles, S_η would have a larger negative value. The total effective convection parameter is given as:

$$S_T = \frac{a}{2}\left(\frac{V_\eta - V_b}{D_\eta + D_b}\right)$$

where subscript 'b' identifies the background parameters. This can be rewritten as:

$$S_T = \frac{1 - \frac{V_b}{V_\eta}}{\frac{1}{S_\eta} - \frac{1}{S_b}\frac{V_b}{V_\eta}} \tag{6.17}$$

It is clear that the effect of adding a negative (outward) convective velocity and increasing the total diffusion will decrease S_T. From Sect. 6.4, $\bar{S}'$ is found to decrease from $\sim 1.2 - 1.4$ (after the pellet injection) to $\sim 0.5 - 0.7$ after the minor disruption (or giant sawtooth). Using the estimates of $S_\eta = -2.5$, $S_b = 1.3$, and $S_T = 0.6$, and using Eq. 6.17, it is found that $V_\eta/V_b \simeq -0.43$, $V_T/V_b \simeq 0.57$, and $D_\eta/D_b \simeq 0.22$, $D_T\ D_b \simeq 1.22$. Thus, using $S_\eta = -2.5$, it is found that the diffusion should increase by $\sim 20\%$ while the (inward) convection in should decrease by $\sim 43\%$.

The values of $D_\eta(r)$ and $V_\eta(r)$, predicted from Eq. 6.14, are shown in Fig. 6.15. $D_\eta(r)$ and $V_\eta(r)$ are seen to be very sensitive to the background density profile peakedness, due to the $(1 + \eta_i)^3$ dependence of D_η and $V\eta$. The maximum values of $D_\eta(r)$ and $V_\eta(r)$ are predicted to be near $r/a = 0.4$. For density profiles of $n = n_0(1 - r^2/a^2)^\alpha$ with $.5 < \alpha < 1.0$, the maximum values (near r/a=.4) of D_η are between $10^3 cm^2/sec - 10^4 cm^2$ sec, and for V_η, between $10^2 cm/sec - 10^3 cm/sec$. Comparing these values with those presented in Sect. 6.4, it appears that for typical background density and temperature profiles, η_i transport is sufficiently large to substantially affect the particle transport.

Using the simple model described above, which assumes that the particle transport just after the pellet injection is due only to a constant background transport, the saturation levels of D_η and V_η are calculated to be: $D_\eta \simeq (0.22)D_b \simeq (.22)(6000) = 1300\ cm^2/sec$. $V_\eta \simeq$

$(0.43)V_b \sim (.43)(1000) = 430$ cm/sec. Thus, this model would predict that $\bar{D}$ would increase by ~ 1300 cm^2/sec and $\bar{V}$ would decrease by 430 cm/sec, after a giant sawtooth or minor disruption, when the density profile returns to flatter, pre-pellet shape. These predictions from this simple model are illustrated in Fig 6.16.

As shown in Figs. 6.6 and 6.9, $\bar{V}$ is seen to decrease $\sim 50\%$, from ~ 1000 cm/sec to ~ 500 cm sec after the giant sawtooth or minor disruption. This is roughly consistent with the results of the above model. As shown in Figs. 6.6 and 6.9, $\bar{D}$ is seen to remain relatively constant just after the giant sawtooth or minor disruption. This is inconsistent with the predictions of the above model, although the uncertainties are close to the relative increases predicted ($\sim 20\%$). $D_\eta(r)$ and $V_\eta(r)$ are predicted to be zero at the orgin ($D_\eta(r) \propto \epsilon^{3/2}$), which is consistent with the small changes in D(r=0) shown in Figs. 6.5 and 6.8.

Therefore, it is concluded that certain aspects of η_i transport theory are consistent with the measurements presented in Sect 6.4. More detailed comparisons are difficult to obtain since the η_i transport parameters are dependent on scale length parameters ($L_s, L_n/L_T$), which have relatively large uncertainties, especially near the origin. For example, L_s is estimated using $q(r) \simeq q_0 + (q_l - q_0)r^2/a^2$. If $q(r)$ were actually flatter near the origin, which might be expected for sawtoothing discharges, this would result in an increase in L_s, and decreases in V_η and $D_\eta(\propto 1/L_s^2)$. Similarly, uncertainties in η_i, due to uncertainties in the ion temperature and density profile shapes near the origin, result in large uncertainties in D_η and V_η ($\propto \eta_i^3$).

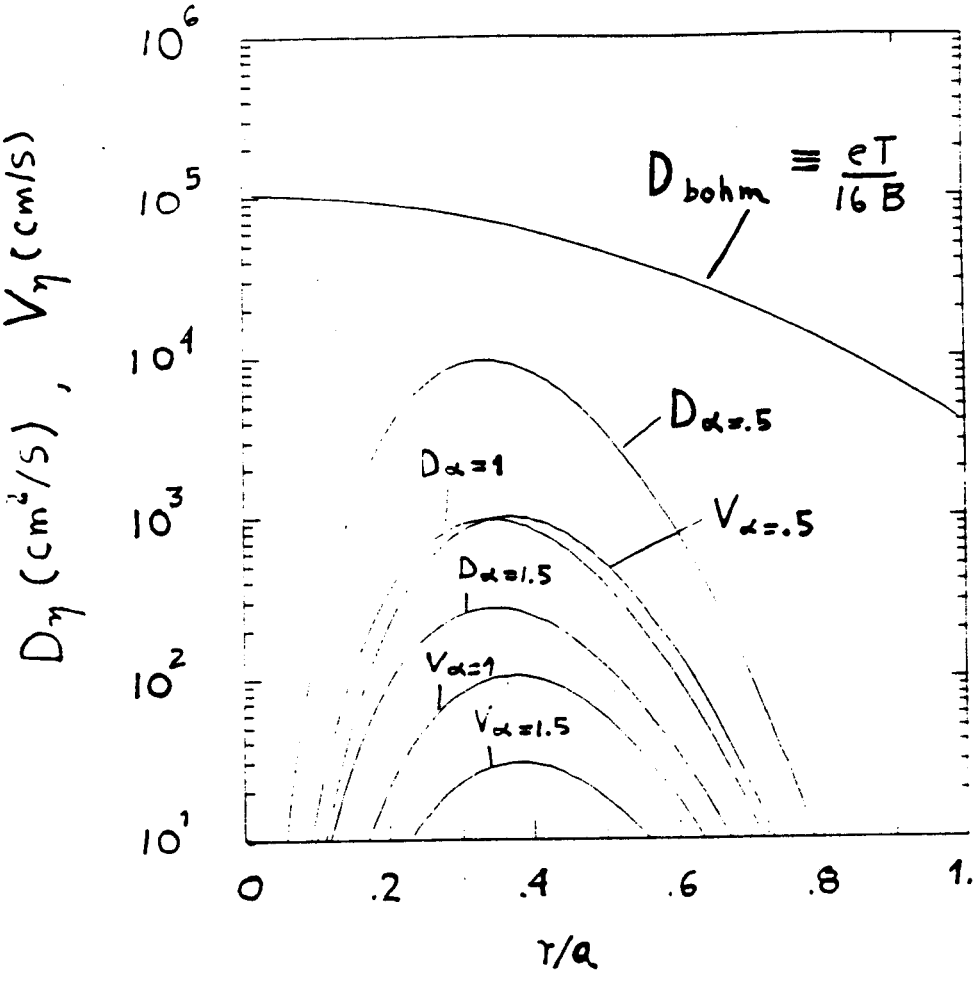

Figure 6.15 — $D_\eta(r)$ and $V_\eta(r)$ for different density profiles. Assumed discharge parameters are: $n_e = n_0(1-r^2/a^2)^\alpha, n_0 = 4\times10^{14}\text{cm}^{-3}, \alpha = 0.5, 1.0, 1.5; T_e = T_0 e^{-r^2/(.55a)^2}, T_0 = 1500\text{eV}; q_0 = 0.9, q_l = 4.$

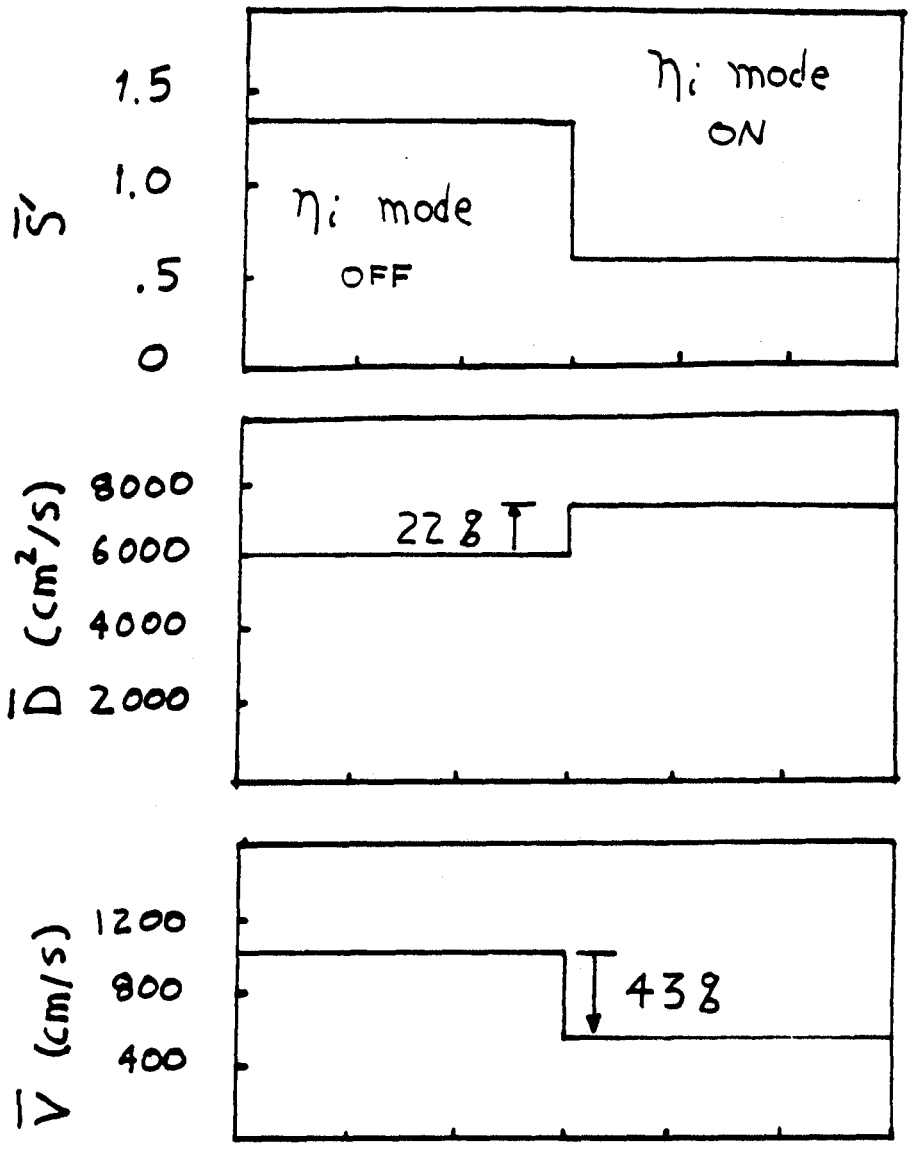

Figure 6.16 — Predicted effects of η_i transport on D, V, and S. Initially, the transport consists of the background values D_b = 6000 cm^2 sec and V_b = 1000 cm sec. After the η_i mode turns on (S_η = −2.5), D is seen to increase by 22% (1300 cm^2 sec) and V to decrease by 43% (430 cm/sec).

6.6 Summary and Discussion

Density profiles obtained from visible continuum measurements have been studied during pellet fueled discharges in order to ascertain the changes induced in the particle transport. A method for obtaining D(r,t) and V(r,t) in the high density, central source-free region of the plasma is developed, allowing changes in diffusion and convection fluxes to be determined. Specifically, results from three common pellet injection cases are presented: discharges with giant sawtooth, large peaking,and high q_I. These results indicate that the increased peaking in the density profiles, also found prior to the giant sawtooth is due mostly to increases in the inward convection flux. D(r) is found to be slightly hollow, with a central value usually near 2500 cm^2/sec. It was determined that increases in $\bar{V}$ found during peaked post-pellet discharges were probably not directly due to the changes in sawtooth activity at that time.

Calculations from neoclassical transport theory result in values for D and V which are too small to account for changes in transport after pellet injection. Values for V near the origin, however, are found to be close to neoclassical values, as was also previously reported on Alcator C during non-pellet discharges[69].

Collisionless η_i theory, relevant for the central region of the Alcator C plasmas studied, is predicted to result in a net outward particle flux[61]. Qualitatively, this type of transport is found to be consistent with the results of Sect. 6.4. Quantitatively, certain features of this theory are also in agreement. Using the value $c_T = -4.3$ predicted by this theory, fractional changes in V for discharges which become highly peaked after pellet injections, are found to be roughly consistent with a model in which the η_i mode is 'turned off' after the pellet injection.

highly peaked after pellet injections, are found to be roughly consistent with a model in which the η_i mode is 'turned off' after the pellet injection. The saturation levels for D_η and V_η are also in reasonable agreement with these measurements, although they are found to be very sensitive to uncertainties in the scale length parameters, especially near the origin. The radial profiles of $D_\eta(r)$ and $V_\eta(r)$ are predicted to be proportional to $\epsilon^{3/2}$, which is consistent with the fact that D(r=0) is observed to change very little after a giant sawtooth or minor disruption.

There are still many questions concerning the changes in particle transport on Alcator C after pellet injections. While it appears that some of these results are consistent with predictions from η_i theory, clearly any other theory that would predict an increase in outward flux with an increase in η_i, might similarly be consistent. The strong correlation between impurity and background transport is also not understood. If the η_i mode is quenched after pellet injection and no other background transport strongly affects the impurities, classical transport might be expected to become relevant. This would result in centrally peaked impurity profiles after pellet injection, (as is in fact observed for Mo). After the giant sawtooth, when the η_i mode returns, impurity transport would be predicted to return to pre-pellet conditions (which is also observed).

CHAPTER 7

Thesis Summary and Recommendations for Future Work

A spatially resolving visible light detector system is used to measure continuum radiation near 5360Å on the Alcator C Tokamak. Accurate determinations of Z_{eff} are obtained from continuum measurements using independently determined temperature and density measurements. Density profiles during high density, clean ($\overline{Z}_{eff} \simeq 1.2$), pellet fueled discharges, are also determined and are used to study the changes in particle transport after injection.

For discharges with sufficiently large pellet density increases ($\Delta\overline{n}_e/\overline{n}_e \simeq .7 - .9$), density profiles are found to become peaked after injection. These profiles either remain peaked for most of the remainder of the discharge or return to pre-pellet flatter profiles after a 'giant' sawtooth. Both the threshold for transport changes and the effect of giant sawteeth are well correlated with changes in trace impurity transport.

Analyses of density profiles after pellet injection yield information about the radial diffusion and convection velocity of the plasma particles. The peakedness in the density profiles, observed after pellet injection, is attributable mostly to increases in inward convection. It is concluded that neoclassical fluxes are too small to account for these changes. Predictions from collisionless η_i transport theory[56] are found to be roughly consistent with the changes in V after pellet injection.

Impurity transport is found to be well correlated with the changes in the background particle transport. However, the relationship between the two is not clear. The increased peaking in impurity profiles may be due to the quenching of the η_i mode after pellet injection, which would then lead to the classical result of peaked impurity profiles.

This thesis has presented measurements and analysis of one-dimensional (radial coordinate) visible continuum brightness profiles using multichannel detector systems. It is suggested that using two orthogonal viewing arrays, two-dimensional profiles could be reconstructed. Measurements of poloidally asymmetric profiles could, in principle, be used to determine both radial and poloidal transport. Spatial and temporal details of the density profile perturbations during giant sawteeth might also be determined. Since recent sawtooth measurements[54] have been found in some cases to be inconsistent with the Kadomtsev model[41], this is currently an area of both experimental and theoretical interest. It is also suggested that by using a 2-D viewing continuum array, spatially resolved density fluctuation profiles could be studied. Since the bremsstrahlung emission is approximately proportional to $n^2/T^{1/2}$, brightness fluctuations would be due mostly to density fluctuations. Intersecting brightness chords could then be cross-correlated (over a sufficient time period) to yield fluctuation profiles.

APPENDIX A

Green's Function Solution to Transport Equation

This section presents the general Green's function solution for the non-homgeneous particle transport equation (Eq. 6.3). As discussed in Chapter 6, the diffusion coefficient D and convection veloctiy V are assumed to have the following simple forms:

$$D(r,t) = D_0 \tag{A.1}$$

$$V(r,t) = V_0 r/a$$

where positive V_0 denotes inward radial flow.

Thus, the particle transport equation is given as:

$$\frac{\partial n(r,t)}{\partial t} + \frac{1}{r}\frac{\partial}{\partial r} r\{-D_0 \frac{\partial n(r,t)}{\partial r} - n(r,t)V_0 r/a\} = N(r,t) \tag{A.2}$$

New variables are introduced :

$$z \equiv r/a, \quad 0 \leq z \leq 1 \tag{A.3}$$

$$x \equiv z^2, \quad 0 \leq x \leq 1$$

$$S \equiv aV_0/2D_0$$

The solution to Eq. A.2 (also Eq. 6.3) has been found to be:

$$n(x,t) = \int_0^t \int_0^1 N(x',t')G(x,x',t,t')\mathrm{d}x'\mathrm{d}t' \tag{A.4}$$

$$- \sum_{n=0}^{\infty} b_n e^{-t/\tau_n} e^{-Sx} M_n(x)$$

where,

$$G(x,x',t,t') = \sum_{n=0}^{\infty} \frac{e^{-Sx} M_n(x) M_n(x') e^{-(t-t')/\tau_n}}{I_n} \qquad (A.5)$$

$M_n(x)$ is a shortened notation for the confluent hypergeometric function $M_n(\frac{-\tau^*}{\tau_n S}, 1, Sx)$ (see Ref. 64). τ_n are the 'eigentimes' of the homogeneous portion of Eq. A.2 and are generally a function of S and D_0. $\tau_n(D_0, S)$ is calculated in Appendix B by expanding $\tau_n(D_0, S)$ around S=0. τ^* is defined as $\tau^* \equiv a^2/4D_0$.

The second term in Eq. A.4 describes the time history of the source free density profiles. b_n is the Fourier-hypergeometric coefficients of the initial density profile n(x,t=0):

$$b_n = \frac{\int_0^1 e^{Sx}\{e^{-Sx} M_n(x) n(x, t=0)\} dx}{\int_0^1 e^{Sx}\{e^{-Sx} M_n(x)\}^2 dx}$$

I_n in Eq. A.5 is a normalization integral given by:

$$I_n = \int_0^1 e^{Sx}\{e^{-Sx} M_n(x)\}^2 dx$$

An important example is for the case where the edge source is approximated by a delta function near the edge x_0 (remembering that $x = z^2$):

$$N(x,t) = A(t)\delta(x - x_0) \qquad (A.6)$$

In this case, Eq. A.4 becomes:

$$n(x,t) = \int_0^t A(t') G(x, x_0, t, t') dt'$$

$$- \sum_{n=0}^{\infty} b_n e^{-t/\tau_n} e^{-Sx} M_n(x)$$

or,

$$n(x,t) = \int_0^t A(t') \sum_{n=0}^{\infty} \frac{e^{-Sx} M_n(x) M_n(x_0) e^{-(t-t')/\tau_n}}{I_n} dt' \qquad (A.7)$$

$$- \sum_{n=0}^{\infty} b_n e^{-t/\tau_n} e^{-Sx} M_n(x)$$

Assuming a simple time dependence for A(t), the time integral can be performed analytically. For example, assuming $A(t) = A_0 + A_1 e^{-t/\tau_N}$, (where τ_N is the decay time for the source) the solution is given as:

$$n(x,t) = \sum_{n=0}^{\infty} \frac{e^{-Sx} M_n(x) M_n(x_0)}{I_n} \left[A_0 \tau_n (1 - e^{-t/\tau_n}) + \frac{A_1 \tau_n \tau_N}{\tau_N - \tau_n} (e^{-t/\tau_N} - e^{-t/\tau_n}) \right] \qquad (A.8)$$

$$- \sum_{n=0}^{\infty} b_n e^{-t/\tau_n} e^{-Sx} M_n(x)$$

For the case $t \to \infty$, Eq. A.8 becomes:

$$n(x, t = \infty) = \sum_{n=0}^{\infty} \frac{e^{-Sx} M_n(x) M_n(x_0) A_0 \tau_n}{I_n} \qquad (A.9)$$

Equation A.9 is the steady-state solution with a delta function source at $x = x_0$ Since τ_n can be written as $a^2/(D_0 f_n(S))$ (as is shown in Appendix B), $M_n(\frac{x\tau_n}{a^2}, 1, Sx) = M_n(f_n(S)/4, 1, Sx)$ is only a function of S, and after substituting $z^2 = x$ into the equation:

$$n(z, t = \infty) = \frac{A_0 a^2}{D_0} \sum_{n=0}^{\infty} \frac{e^{-Sz^2} M_n(z^2) M_n(z_0^2)}{I_n f_n(S)} \qquad (A.10)$$

The profile shape of $n(z, t = \infty)$ clearly only depends on S and z_0. The peak-to-average of the steady-state profile vs. S is shown in Fig. 6.2 for the cases $z_0 = 0.9$ and $z_0 = 0.95$. These results indicate that the peakedness of these steady-state profiles are only weakly dependent on the exact position of the edge source. Thus, using more physical, distributed edge sources should also result in steady-state profiles shapes which are only dependent on S.

APPENDIX B

Calculation of Eigenvalues $\tau_n(D_0, S)$

In order to utilize the Green's function solution presented in Appendix A, it is necessary to know the 'eigentimes' τ_n, which are generally a function of D_0 and $S \equiv aV_0/2D_0$. These eigentimes are derived from the eigenvalues of the homogeneous portion of Eq. 6.3. D and V are assumed to have the following simple forms:

$$D(r,t) = D_0 \tag{B.1}$$

$$V(r,t) = V_0 r/a,$$

where positive V_0 denotes inward radial flow. The homogeneous transport equation is given as:

$$\frac{\partial n(r,t)}{\partial t} - \frac{1}{r}\frac{\partial}{\partial r} r\{-D_0 \frac{\partial n(r,t)}{\partial r} - n(r,t)V_0 r/a\} = 0 \tag{B.2}$$

Seperating n(r,t) into n(r,t)=y(r)T(t), Eq. B.2 becomes:

$$\frac{1}{y}\frac{\partial}{\partial r} r(-D_0 \frac{\partial y}{\partial r} - \frac{yV_0 r}{a}) = \frac{-1}{T}\frac{\partial T}{\partial t} = \frac{1}{\tau_n} \tag{B.3}$$

where $\tau_n > 0$ is a constant to be determined from the boundary conditions.

The time solution is clearly :

$$T(t) = T_0 e^{-t/\tau_n} \tag{B.4}$$

The equation for y(r) is now:

$$\frac{\partial}{\partial r} r\left(D_0 \frac{\partial y}{\partial r} + \frac{y V_0 r}{a}\right) = \frac{-y}{\tau_n} \qquad (B.5)$$

The series solution to Eq. B.5 has been found to be (within a constant) :

$$y(r) = 1 - \frac{(-S' - C)}{2^2} r^2 - \left(\frac{-S' + C)(-2S' + C)}{2^2 4^2} r^4 \right. \qquad (B.6)$$
$$\left. - \frac{(-S' - C)(-2S' - C)(-3S' + C)}{2^2 4^2 6^2} r^6 + \ldots \right.$$

where S' and C are functions of D_0, τ_n and $S \equiv aV_0/2D_0$ given by:

$$S' \equiv \frac{-4S}{a^2} \qquad (B.7)$$
$$C \equiv \frac{1}{\tau_n D_0}$$

Imposing the boundary condition on Eq. B.6 of $y(r = a) = 0$ and defining $y_a(S', C(S')) \equiv y(r = a)$ Eq. B.6 becomes:

$$y_a = 0 \equiv 1 - \frac{(-S' + C)}{2^2} a^2 + \left(\frac{-S' + C)(-2S' + C)}{2^2 4^2} a^4 \right. \qquad (B.8)$$
$$\left. - \frac{(-S' + C)(-2S' + C)(-3S' - C)}{2^2 4^2 6^2} a^6 + \ldots \right.$$

In order to determine C(S') in Eq. B.8, (which will lead to the solution for $\tau_n(S')$ from Eq. B.7), C(S') is written as a Taylor expansion around S'=0:

$$C(S') = C_{S'=0} + \left.\frac{dC}{dS'}\right|_{S'=0} S' - \frac{1}{2}\left.\frac{d^2C}{dS'^2}\right|_{S'=0} S'^2 + \ldots \qquad (B.9)$$

The first term in Eq. B.7, $C(S'=0)$, corresponds to an eigenvalue of the Bessel function J_0 (since the case $V_0 = 0$ simplifies Eq. B.2 into the differential Bessel Equation of zero order). To simplify things, consider only the first eigenvalue, so that $\tau_0(S'=0) = \tau_{0J} = a^2/(2.405)^2 D_0$, where τ_{0J} is the lowest order eigentime of J_0. Higher orders can be calculated in a similar manner.

Thus, from Eq. B.7,

$$C(S'=0) = \frac{1}{\tau_0(S'=0)D_0} = \frac{(2.405)^2}{a^2} \qquad (B.10)$$

which is the constant term in Eq. B.9.

In order to obtain the higher order Taylor coefficients of Eq. B.9, first note that since $0 = y_a$, it follows that :

$$0 = \frac{dy_a}{dS'}$$

$$0 = \frac{d^2 y_a}{dS'^2}$$

$$\vdots$$

Therefore,

$$\frac{dy_a(S', C(S'))}{dS'} = \frac{\partial y_a}{\partial S'} - \frac{\partial y_a}{\partial C}\frac{dC}{dS'} = 0 \qquad (B.11)$$

or,

$$\frac{dC}{dS'} = \frac{-\partial y_a / \partial S'}{\partial y_a / \partial C} \qquad (B.12)$$

The numerator and denominator of Eq. B.12 are calculated by taking the partial derivatives of Eq. B.8 with respect to S' and C, resulting in a ratio of two infinite summations. $\frac{dC}{dS'}_{S'=0}$ is then obtained

by inputting $S' = 0$ and $C(S' = 0) = (2.405)^2/a^2$ (Eq. B.10) into the resulting expression. After summing 9 terms, the numerator is calculated to be -5.396935×10^{-2}, the denominator $-.1079387$. Thus the second term in Eq. B.9 is:

$$\left.\frac{dC}{dS'}\right|_{S'=0} = 0.50000 \qquad (B.13)$$

Higher order terms are determined in a similar manner but become progressively more complicated to calculate.

For example, the next term in Eq. B.9 is written as:

$$\left.\frac{d^2C}{dS'^2}\right|_{S'=0} = \left.\frac{\frac{-\partial y_a}{\partial C}\left(\frac{\partial^2 y_a}{\partial S'^2} - \frac{\partial^2 y_a}{\partial S'\partial C}\frac{dC}{dS'}\right) + \frac{\partial y_a}{\partial S'}\left(\frac{\partial^2 y_a}{\partial S'\partial C} + \frac{\partial^2 y_a}{\partial C^2}\frac{dC}{dS'}\right)}{(\partial y_a/\partial C)^2}\right|_{S'=0} \qquad (B.14)$$

Each partial derivative in Eq. B.14 is calculated from Eq. B.8 by substituting S'=0 and C(S'=0) = $(2.405)^2/a^2$. $\left.\frac{dC}{dS'}\right|_{S'=0}$, which appears in Eq. B.14, was calculated previously to be 0.5000.

A general algorithm was written which calculates the higher order Taylor coefficients for Eq. B.9. After substituting the definition for S' and C into Eq. B.9, an expression for τ_0 is found to be:

$$\tau_0 \simeq (a^2/D_0)\{(2.405)^2 - (2.000)S - (.21805)S^2 \qquad (B.15)$$

$$-(1.2487 \times 10^{-3})S^4 + (6.1507 \times 10^{-6})S^6\}^{-1}$$

This expression has been found to be accurate in the range $-5. \leq S \leq 5.$ by verifying that y_a is zero for these predicted values of τ_0. Negative values for S represent radially outward particle flows $V_0 < 0$.

Higher order eigentimes are calculated by expanding around the higher order zeros of J_0. For example, using C(S'=0) = $(5.5201)^2/a^2$ in the above analysis results in expression for $\tau_1(D_0, S)$:

$$\tau_1 \simeq (a^2/D_0)\{(5.5201)^2 - (2.000)S + (.31145)S^2 \qquad (B.16)$$

$$+(3.6483 \times 10^{-4})S^4 - (5.8701 \times 10^{-6})S^6\}^{-1}$$

References

1. Gross, R.A., "Fusion Energy", Wiley and Sons, New York, 1984.
2. Miyamota, K., "Plasma Physics for Nuclear Fusion", MIT Press, Cambridge, MA, 1980.
3. Bateman,G.,"MHD Instabilities",MIT Press, Cambridge, MA, 1978.
4. Artsimovich, L.A., *Nucl. Fusion* **12** (1972) 215.
5. "Plasma Physics and Controlled Nuclear Fusion Research", (Conf. Preceeding, 1968)(IAEA, Vienna, 1969) Translation of Russian Paper: *Nucl. Fusion. suppl.* (1969).
6. Parker, R.R., Greenwald, M., Luckhardt, S.C., Marmar, E.S., Porkolab, M., Wolfe, S.M, *Nucl. Fusion* **25**, 1127 (1985).
7. Greenwald, M., *et al.*, Phys. Rev. Lett. **53** (1984)352.
8. Karzas, J., Latter, R., Astrophys. J., Suppl. Ser. 6, (1961) 167.
9. Griem,H. " Plasma Spectroscopy". McGraw-Hill, New York, 1964.
10. Kramers, H.A., Phil. Mag. **46** (1923) 836.
11. Brussaard, P.J., Van de Hulst, H.C., Rev. Mod. Phys., Vol 34 **3** (1962) 507.
12. Vershkov, V.A., I.V. Kurchatov Inst. Of Energy, Moscow, Private comm. (1985).
13. Vershkov, V.A.,Krupin, V.A., Pimenov, A.B., Khvostenko, P.P., Sov.J.Plasma Phys. **10** 515 (1984).
14. Foord, M.E., Marmar, E.S, Terry, J.L., Rev. Sci. Inst. **53**, 1407 (1982).
15. Kadota,K., Otsuka, J..Fujita,J.,*Nucl. Fusion* **20** 209 (1980)
16. Marmar, E.S., *et al, Bull. Am. Phys. Soc.* **25** 951(1980).
17. Fonck, R.J., *et al.*, "Particle Fueling and Impurity Control in PDX", Princeton Plasma Physics Laboratory - PPPL-2175 (1984).
18. Hawryluk,R.J., *et al.*, Proc. 4th Int. Symp., Rome, 1984, Vol. 2, 1012.

19. Rebut, P.H., *et al.*, Proc. 4th Int. Symp., Rome, 1984, Vol. 2, 991.

20. Born,M., Wolf,E.,"Principles of Optics", Macmillan, New York, 1964.

21. Oriel Manuf. Cat., H14, Oriel Co., Stamford, CO, 1979.

22. "Starfire - A Commerical Tokamak Fusion Power Plant Study", Argonne National Laboratory - ANL/FPP-80-1, Argonne, IL, 1980.

25. Rice,J.E.,*et al.*, "Influx and Sources of Medium and High Z Intrinsic Impurities on the Alcator C Tokamak", Plasma Fusion Center-PFC/JA-83-35, MIT, Cambridge, MA, (1983).

26. McCracken, G.M., Stott, P.E., *Nucl. Fusion* **19** (1979), 889.

27. Moreno,J.C., Ph.D. Thesis," An Experimental Study of Visible and UV Impurity Emission from the Alcator C Tokamak", Plasma Fusion Center - PFC/RR-85-20, MIT, Cambridge, MA, (1985).

28. Rice J., Plasma Fusion Center, Cambridge, MA, Private comm. (1985)

29. Braginskii,S.I.,"Reviews of Plasma Physics",1, Consultants Bureau, New York, 1965.

30. Stacey, W.M., "Fusion Plasma Analysis", Wiley and Sons, New York, 1980.

31. Marmar,E.S., *et al.*, *Nucl. Fusion* **22**, 1567 (1982).

32. Terry, J.L., *et al. Bull. Am. Phys. Soc.* **30** 1412(1985).

33. Petrasso, R.D., Phys. Rev. Lett.,**57** 707 (1986).

34. Lipschultz, B., *et al.*, *Nucl. Fusion* **24**, 977 (1984).

35. Terry, J.L., *et al. Bull. Am. Phys. Soc.* **26** 886(1981).

36. Baker, D.R., *et al.*, *Nucl. Fusion* **22** 807 (1982).

39. Foord, M.E., Marmar, E.S. *Nucl. Fusion* **25** 197 (1985).

40. Von Goeler, S., Stodiek, W. *et al.*, *Nucl. Fusion* **15**, 306 (1975).

41. Kadomtsev, B., Sov. J. Plasma Phys. **1** 389 (1975).

42. Dnestrovskii, Y., Lysenko, S.E., Smith, R., Sov. J. Plasma Phys. **3** 9 (1977)

43. Jahns,G.L., Soler,M., Waddell,B.V.,*Nucl. Fusion* **18** 609 (1978).

44. Vasin, N., Gorbunov, E.P., Neudachin, S.V., Pereverzev, G.V., Sov. J. Plasma Phys. **8** 2 (1982).

45. Parail, V., Pereverzev, G.V., Sov J.,Plasma Phys, **6** 1 (1980).

46. Spitzer,L.,"Physics of Fully Ionized Gases", Interscience Publishers, New York, 1962.

47. Wolfe,S.M.,*et al.*, *Nucl. Fusion* **26** 329 (1986)

49. Terry J.L., Plasma Fusion Center, Cambridge, MA, Private comm. (1986)

50 Greenwald, M., Plasma Fusion Center, Cambridge, MA Private comm. (1986).

51. Terry J.L., Plasma Fusion Center, Cambridge, MA, Private comm. (1986)

53. Seguin,F.H., *Bull. Am. Phys. Soc.* **28** 1249(1983).

54. Cambell,D.J.,*et al.*, *Nucl. Fusion* **26** 1085 (1986)

55. Hinton,F.L., Hazeltine, R.D., Rev Mod Phys, Vol. 48, No. 2., (1976)

56. Antonsen,T.,*et al.*, *Nucl. Fusion*, **19** 641 (1979)

57. Freeman,R.L., Jones,E.M., " Atomic Collision Processes in Plasma Physics Experiments", UKAEA Research Group, Culham Laboratory - CLM-R 137, Abingdon, Berkshire (1974)

58. Fiore, C., Plasma Fusion Center, Cambridge, MA, Private comm. (1986).

59. Chang,C.S., General Atomic Co., San Diego, CA., Private Comm. (1985).

60. Coppi,B.,Spright,C., Phys. Rev. Lett. **41**, 551 (1978)

61. Lee,G.S., Diamond.P.H., "Theory of Ion-Temperature-Gradient-Driven Turbulence in Tokamaks", Inst. for Fusion Studies - IFSR 209, Austin, TX (1986).

62. Diamond,P.H., Inst. for Fusion Studies, Austin, TX, Private comm. (1986).

63. Seguin,F.H., *et al.*," On Impurity Transport in Tokamaks", Plasma Fusion Center - PFC/JA-82-25, MIT, Cambridge, MA. (1982)

64. Abramowitz, A., Stegun,I., " Handbook of Mathematical Tables", Dover Pub-

lications, New York (1972).

65. Foord, M.E., *Bull. Am. Phys. Soc.* **28** 1248(1983).

66. Gondhalekar, A.,*et al.*, "Density Buildup in JET" from Reprints of JET Poster Presentations at the 27th Annual APS Plasma Physics Meeting, San Diego, CA, 1985 -JET-P(85)31.

67. Schmidt, G.L.,"Pellet Injection Results During TFTR Ohmic and Neutral Beam Heating Experiments", Eleventh IAEA Meeting, Kyoto,Japan, Nov., 1986.

68. Kim, S.B., *Nucl. Fusion* **26** 1251 (1986).

69. Wolfe, S.M., *Bull. Am. Phys. Soc.* **26** (1981) 976.

70. Lee, G.S., Oakridge National Labs, Oakridge, Tenn., Private comm. (1986).